Science
AAAS

Supplementary Materials for

A rockslide-generated tsunami in a Greenland fjord rang Earth for 9 days

Kristian Svennevig *et al*.

Corresponding author: Kristian Svennevig, ksv@geus.dk

Science **385**, 1196 (2024)
DOI: 10.1126/science.adm9247

The PDF file includes:

Other Supplementary Material for this manuscript includes the following:

Materials & methods

(a) Volume calculations from Digital Surface Models (DSMs), using satellite stereo-photogrammetry (Pléiades satellite images) and structure from motion (SfM)

The 2023-09-16 landslide volume was determined using the ArcticDEM Digital Elevation Model; (*63*) considered as the topography before the rockslide event, and two post-event topographies constructed from satellite stereo-photogrammetry applied to cloudless very-high resolution Pléiades satellite imagery acquired on 2023-09-29 and from Structure from Motion (SfM) model constructed from airborne photographs acquired on 2023-09-19.

(i) Satellite Pléiades stereophotogrammetric topographic model of the area

The satellite stereo-photogrammetric model was constructed from a triplet of Pléiades panchromatic images (native spatial resolution: 0.70 m; spectral band: 0.47–0.83 µm) specifically tasked through the CIEST2 program of the French Solid Earth datahub ForM@Ter, and the French Space Agency (CNES). Cloudless images were acquired over the area on 2023-09-29 with incidence angles of 11°, 91°, and 169° along the same orbital track in a single mode path between 14:25 and 14:26 UTC. The images were coded in primary mode (e.g., 12 bits per pixel) and in a GeoTIFF file format, which is the geometric processing level closest to the natural image acquired by the sensor. It ensures a high dynamic range at acquisition, anti-aliasing, high sharpness, and exhaustive preservation of the acquired information. Therefore, each pixel can take one value out of 4096 allowing the detection of subtle nuances at the beginning or the end of the energy spectrum, thus giving an increased capability to distinguish objects within the shadows of a mountain and pale-colored elements in very light/bright environments such as ice and bedrock such as in Greenland. This mode further ensures that the sensor is placed in rectilinear geometry and that the images are clear of all radiometric distortion. The Pléiades images are transferred in basic radiometric mode corresponding to raw data without radiometric processing. In this mode, each pixel is given in digital numbers, i.e., native pixel values from the sensor acquisition (after equalization). Those digital numbers quantify the energy recorded by the detector, corrected relative to the other detectors to avoid non-uniformity noise. Rational Polynomial Coefficients (RPCs) and the sensor model are provided with the product to apply tailored post-processing techniques such as stereo-photogrammetry. The image coordinate system is WGS84. The photogrammetric generation of the Pléiades DSM is based on the DSM-OPT automated processing chain (en.poleterresolide.fr/dsm-opt-service/) built upon the open-source MicMac photogrammetric library and specific developments made for dense matching of multi-view satellite acquisitions. The DSM-OPT processing comprises tie-point detection and bundle adjustment of the three input Pléiades images to initially compensate for the relative biases in the RPC sensor models. Subsequently, dense matching is applied for the stereo triplets using a multi-directional dynamic programming approach (a variant of semi-global matching implemented in MicMac; github.com/micmacIGN/micmac). The target spatial resolution for the Pléiades DSM has been set to 1 m. The relative alignment of the Pléiades surface model is performed with ArcticDEM (tile of 2022-05-22) used as a reference; the iterative closest-point (ICP) algorithm implemented in the AMES stereo-pipeline (github.com/NeoGeographyToolkit/StereoPipeline) and the demcoreg library (demcoreg.readthedocs.io/) is used and applied on areas considered as stable in the images, e.g., not affected by the rockslide and by glacier motion. The residual biases and statistical dispersion of the elevation differences of the aligned Pléiades DSM, computed on these stable areas, are summarized by a mean and a standard deviation of, respectively, 0.10 m and 1.21 m. The aligned Pleiades DSM

was then geocoded in the UTM25N coordinate system.

(ii) Structure from Motion airborne topographic model of the area

The Structure from Motion (SfM) model used 68 photographs, including 16 acquired by a DJI Mini 3 Pro Uncrewed Aerial Vehicle (UAV) flight over the lower section of the glacier and 52 photographs taken manually with a Canon EOS 5D Mark IV camera during an overflight of the landslide area by the Royal Danish Air Force. The photographs were processed in Agisoft Metashape v. 2.0.1. Six control points for SfM processing were generated from the Arctic DEM by identifying common points on the post-event photographs and the Arctic DEM hillshade. These control points and the Global Positioning System (GPS) tags of the UAV photographs provided georeferencing for the SfM model. The photographs were aligned using the following settings: high accuracy, generic and reference pre-selection, and adaptive camera model fitting. Alignment was optimized after points with reconstruction uncertainty >50 and reprojection error >0.5 were removed, and the dense cloud was constructed using medium quality and mild depth filtering.

(iii) Elevation changes and volume calculation

Two different surfaces were calculated, e.g., (1) Pléiades DSM model versus ArcticDEM, and (2) SfM DSM model versus ArticDEM.

For 1), the difference surface was first analyzed visually to delineate the approximate outlines of each unit of interest: a) the rockslide source area volume, b) the debris volume on the glacier, and c) the volume entrained from the top of the glacier below the impact area (e.g., eroded glacier). This preliminary inspection allows the detection and exclusion of areas with artifacts in both the Pleiades DSM (e.g. bright areas, shadows) and the ArticDEM. To avoid omission errors, the delineated outlines comprise fractions of unchanged terrains around these three units. The volume of each unit is computed from the sum of the elevation changes Δz_i of all pixels of the affected unit and the surface area of the individual pixels Δx^2. The estimated volumes and uncertainties are $23.4 \pm 1.4 \times 10^6$ m^3 [SEM] for 1), $0.8 \pm 0.3 \times 10^6$ m^3 [SEM] for 2) and $1.3 \pm 0.5 \times 10^6$ m^3 [SEM] for 3) (Fig S16).

For 2), change detection was performed in CloudCompare (www.danielgm.net/cc/) using the M3C2 algorithm (*64*) to estimate the error in the DEM-SfM comparison and to delineate the landslide area. To calculate landslide volume, we manually clipped out the landslide area and used the 2.5-dimensional (D) volume tool in CloudCompare. Different grid sizes yielded no change in volume, and using vertical or horizontal projection yielded very similar volumes of 25.53×10^6 m^3 and 25.43×10^6 m^3 respectively. In the stable bedrock areas adjacent to the landslide, the M3C2 change has an average value of 1.8 m and a standard deviation of 4.7 m. The average M3C2 change in the landslide area is 74 m, an uncertainty of 6-7 % for the volume calculation. This yields a volume of $25.5 \pm 1.7 \times 10^6$ m^3 (SEM) for the landslide. The value of 1.8 m represents the systematic offset between the two DEMs and is likely due to a combination of georeferencing errors and sensor inaccuracies within both DEMs.

For the estimation of the volume change of the lower glacier, a different procedure was used, due to the uncertainty of the Arctic DEM and the time lag between the Arctic DEM data collection and the 2023 event, which could conflate the longer-term evolution of the glacier with the landslide impacts. Instead, we used 34 field photographs collected from 4 different cameras in August 2022 and August 2023. These photographs were taken from boats in the fjord, limiting the coverage to the lower section of the glacier. These were combined with the 2023 photographs and processed in Agisoft Metashape using a co-alignment workflow (*65*). This method yields reliable change detection in the absence of

precise georeferencing by combining the photos from both epochs in the point matching and bundle adjustment stage of SfM processing. The parameters used for processing in Metashape were the same as described above.

Despite the large differences in photograph distribution and vantage point between the two epochs, the resulting models are highly consistent. In stable regions with good coverage in both models, the average M3C2 distance was 0.08 m with a standard deviation of 0.84 m. The average M3C2 distance over the glacier was 13.1 m, suggesting an uncertainty of 6.5%. Similar to the landslide volume calculation, the glacier area was manually clipped, and the volume was calculated using the 2.5D volume tool with a vertical projection, yielding a volume of $2.3 \pm 0.15 \times 10^6$ m^3 (SEM).

In the landslide impact zone, a reliable measurement of change could not be obtained, as the high uncertainty of the ArcticDEM-SfM comparison precludes the measurement of relatively small changes. In addition, as described below, an artifact in the ArcticDEM extends into the downstream end of the impact zone. This both introduces errors and makes it difficult to evaluate the uncertainty in the valley floor elevation comparison. Further, a surface elevation change in the impact zone will conflate three different sources of change – the long-term glacial lowering, the removal of glacial material by the landslide, and the deposit of a small amount of landslide material. The original ArcticDEM contains a large artifact in the central section of the glacier, where the elevations within the narrow valley are up to 200 meters higher than expected. In addition to the elevation anomaly, the boundaries of this artifact can be identified from patterns in the surface aspect, slope, and boundary of the ArcticDEM tiles. To estimate a more accurate valley topography, we constructed a corrected ArcticDEM by assuming that the width and gradient of the glacier were constant across the artifact area, consistent with the linear glacier profile both upstream and downstream. This provided estimates of valley bottom elevation through the affected area that were used to replace the anomalous values in the original DEM.

(b) Glacier elevation change

We analyze glacier elevation change from 1987 to 2018 by comparing elevation data made from 1987 aerial photos and an ArcticDEM strip from 2018 (*63*). We also assess elevation change from the Little Ice Age to 2018 using a glacier ablation area surface reconstruction (*66*) using the LIA (Little Ice Age) geometry of the glaciers recorded in the landscape, such as moraines and trimlines, for the reconstruction.

The topographical setting of the glacier outlet being funneled through a narrow gully makes it a challenge to get good elevation data free of artifacts from clouds, fog, and shadow. We examined same-day acquisition ArcticDEM strips from 2012 to 2021 and found that two 2012 strips were suitable as a reference DEM for co-registration and a 2018 strip had sufficient data on the glacier itself with little in terms of artifacts. ArcticDEM strips were filtered to only use the good data (bitmask = 0), resampled to 5 m, and reprojected to UTM 26 (EPSG:32626). A reference DEM was made from the two 2012 strips (co-registered using (*67*)) and unstable topography was masked away. All DEMs were subsequently co-registered to this reference DEM using (*67*).

The 1987 AeroDEM model (*68*) has little good data on the glacier, so from the same photos and ground control as used for the AeroDEM and orthophotos a new elevation dataset was made using Structure from Motion (Agisoft Metashape v. 2.0.1). This new 1987 point cloud was gridded to a 5 m grid and co-registered to the 2012 reference DEM. Both the standard deviation and root-mean-square error on the co-registration is 5.1 m.

The glacier height change raster was void-filled using a hypsometric method. We use a modified glacier outline polygon divided into elevation bins using 50 m contour lines from SDFI (*69*).

We find that during the 1987-2018 period the ice cap, from which the outlet glacier (GLIMS ID: G333056E72786N) at Hvide Støvhorn originates, reconfigured with increased mass loss at lower elevations due to a combination of increased ablation and discharge of solid ice into Dickson Fjord, and increased accumulation at higher elevations in the interior of the ice cap (Fig. S17). Land-terminating glaciers on the same ice cap also show this pattern of thinning (and retreat) of the snout and accumulation in the interior, so that the increased melting in the ablation area and precipitation in the accumulation area results in higher turnover. This glacier reconfiguration indicates a response to a warmer climate with increased precipitation (*70*). The local glaciers and ice caps in northeast Greenland have seen a negative mass balance since the Little Ice Age, which has accelerated since 2000 (*66*). However, the glaciers in the East Greenland subregion underwent a mass gain in 2015-2019 (*70*) so the ice surface elevation of the glacier will be decreasing in LIA-2014 and increasing in 2015-2019.

The polygons in Fig. 2C show the mean elevation change in each 50 m elevation bin, and the surface just below the rockslide has lowered 19 to 26 m for the 1987-2018 period if the glacier follows the regional trend.

According to (*66*) the ice surface has lowered by ~100 m between LIA-2018 or roughly 0.85 m/yr since the nominal date of glacier retreat from LIA maximum extent of 1900 CE. Because this rate is higher than the observed rate of elevation change during 1987-2018 which is ~0.65 m/yr, it is unlikely that the reconstruction of this specific glacier is reliable. This is probably due to a combination of shallow and steep angles in the gully precluding a good manual trace of trimlines in aerial and satellite images, and image correlation in satellite images. An ablation area mass balance of -0.17 and -0.41 m water equivalent (0.20 and 0.48 m/yr) for the periods LIA-2015 and 2000-2019, has been reconstructed in the northeast Greenland region (*66*). We use this as a rough estimate that from LIA-1987 the ice surface elevation has decreased at least 17 m and up to 100 m (*66*) and that most of the elevation decrease from 2000-2019 occurred before 2015.

(c) In situ measurements in the fjord

Observatory systems (or stations) are located in the inner part of Dickson Fjord, farther out at Ella Ø, and Sverresborg in the outer part of the fjord system near the East Greenland coast. Standard meteorological conditions are recorded (e.g., atmospheric temperature, wind speed and direction, atmospheric pressure, relative humidity, and precipitation) as well as ocean properties, e.g., pressure (tides), water temperature, and conductivity (salinity). Tidal and turbidity data are presented in Fig. S18. Additional measurements such as currents, sea ice keel, irradiance, turbidity, and colored dissolved organic matter are also made at the Ella Ø observatory. Data at Dickson Fjord and Sverresborg are recorded at 15-minute intervals but only transmitted near-real time every 30 minutes. At Ella Ø station, data are measured every 30 minutes and transferred daily. In addition, a 500 kHz acoustic doppler current profiler (ADCP) is installed on a subsurface buoy. The mooring is set to measure the current profile (hourly), ice keel and drift (12 hourly), and waves (15 min sampling rate). The subsea mooring data are transferred via inductive link to land where it is transferred daily via satellite data link to the server and dashboard. The raw high-frequency measurements from which averages are calculated are stored on the sensor and are available after the recovery of the mooring (planned for 2025). A more detailed setup of the observatory system at Ella Ø is provided by Rysgaard et al. (*71*). An increase in turbidity induced by tsunami waves eroding the coast at Ella Ø was visible

30 minutes after the pressure signal at Dickson Fjord. At Ella Ø, turbidity increased steeply over 3 hours and could be detected for about 6-7 hours. Dickson Fjord data are available from Boone et al. (*62*).

(d) Tsunami runup height mapping methodology

Tsunami runup height was mapped using Sentinel 2 L2A satellite images (*72*) from before, during, and after the tsunami event (Fig. S19) (recorded 2023-09-14 14:01 UTC, 2023-09-16 13:51 UTC, and 2023-09-17 14:11 UTC). At Ella Ø, a detailed runup height was mapped on a 2.59 cm/pixel DEM and orthophoto produced from drone images recorded on 10 September 2022. Using this dataset and photos recorded the day after the tsunami by the Danish Army, a detailed runup height could be reconstructed here.

In the Sentinel-2 scenes from after the event, dark colors relative to the images from before the event showed where the coast had been inundated. The boundary between these dark areas and the unaffected lighter areas was mapped as a polyline and a representative elevation for this line was read from the 2 m resolution Greenland DEM (https://dataforsyningen.dk/data/4780). The scenes from the 14 September and the 17 September cover the whole fjord system while the scene from the 16 September only covers the southeastern part and thus not the landslide area.

(e) Infrasound analysis

Following the tsunamigenic rockslide, infrasound has been detected on infrasound arrays I37NO (Bardufoss, Norway at 1667 km; Fig. S4) and I43RU (Dubna, Russian Federation at 3310 km). These arrays are part of the International Monitoring System (IMS) that is being installed for the verification of the Comprehensive Nuclear-Test-Ban Treaty (CTBT). Other nearby IMS infrasound arrays (I18DK in northwest Greenland at 1267 km and I26DE in Southern Germany at 3348 km) did not detect signals from the event.

Fig. S20 shows the array processing results from infrasound array I37NO. The results have been obtained using a time-domain delay-and-sum beamforming routine (*73*, *74*) in the 0.6-4 Hz passband. The algorithm searches the most coherent signal within the set of beams (defined by back-azimuth and phase speed) that are considered in the grid search. The coherency and probability of detection are quantified by the Fisher ratio. The Fisher ratio can also be related to a single-channel signal-to-noise ratio (SNR), assuming that the background noise on the array elements is uncorrelated Gaussian white noise.

The results show that between 5000 and 6000 s after the origin time (i.e., between 14:00 and 14:15 UTC), a coherent infrasound signal is detected that can be associated with the rockfall event based on the travel time and the observed back-azimuth, based on ray-theoretical simulations (Fig. S21). The group velocity of 0.3 km/s indicates that the signals have propagated through the stratospheric waveguide, i.e., between the ground and ~50 km altitude. The signals are transient and seem most coherent between 0.3 and 2.0 Hz, with a peak coherency around 0.5 Hz, and resemble signals from other landslides, e.g., the 2017 Nuugaatsiaq landslide. The detection at I43RU has a very low signal-to-noise ratio (SNR) of ~0.7 compared to the signal at I37NO (SNR ~3) and has a similar group velocity.

Infrasound propagation simulations from Greenland to I37NO (Fig. S21) using a 1-D model of the atmosphere (European Centre for Medium-Range Weather Forecasts [ECMWF] operational forecast for 2023-09-16 at 1300 UTC) confirms that the signals are guided in the stratospheric waveguide. A

parabolic equation (PE) model (*75*, *76*) is used to simulate the transmission loss (TL) from the source at 0.5 Hz, which amounts to 50 dB (re 1 km). In addition, a 3-D raytracer (*77*) is used to simulate the eigenray (shown in blue in Fig. S21) from which arrival time, back-azimuth, and phase speed at I37NO are estimated. A comparison shows a good agreement between simulations and observations. The non-detections at I18DK and I26DE can be explained by a low signal level that vanishes in the background noise at the station level, due to inefficient thermospheric propagation conditions (I18DK) and long-range (I26DE), respectively.

No infrasonic signal was detected in the frequency band around 10 mHz. This could mean that either (i) the source of the very long-period (VLP) signal did not radiate infrasound into the atmosphere, or (ii) the resulting VLP signal was not efficient in propagating in the atmosphere over longer ranges as the signal could not be trapped into atmospheric waveguides because of vertical radiation.

(f) Inversion of the landslide force history (LFH)

The occurrence of landslides involves the acceleration and deceleration of a mass, leading to the loading and unloading of the slope and the generation of long-period seismic waves. Forces contributing to this loading-unloading cycle include gravity, basal friction, and centripetal forces. Each force has a reactive counterpart acting in the opposite direction across the slide contact area (*18–20*, *33–35*, *37*, *78–80*).

The landslide applies a force F on the solid Earth, opposing the force Fs, equivalent to the bulk momentum change of the slide, given by: $F[x,t] = -Fs = \frac{d(mv)}{dt}[x,t]$

Here, m represents the mass of the landslide, v is the velocity of the center-of-mass at position x and time t. The time-varying forces acting during the loading-unloading cycle can be extracted through the inversion of long-period seismic waves, offering insights into the dynamics of the landslide.

To determine the landslide force history of the Dickson Fjord landslide, we use the inversion method developed by (*19*) as implemented in the *lsforce* Python library (*81*). This method approximates the landslide seismic source as a time-varying, 3-D force vector acting at a fixed point, justified when the spatial scale of the slide is small compared to the wavelength of the seismic waves and distances to recording seismic stations.

The LFH is derived from long-period waveforms recorded at three broadband stations. Component time histories (north, east, vertical) are parameterized using a sequence of overlapping isosceles triangles. Amplitudes of these triangles are solved by minimizing the misfit between observed and synthetic seismograms filtered between 10 and 60 seconds. Synthetic seismograms are calculated by summing Earth's elastic normal modes with corrections for laterally heterogeneous crust and mantle (*82*). We use the iasp91 2 s Earth model (*83*). Each force component's time history is constrained to integrate to zero, ensuring the sliding mass is at rest before and after the landslide. Various source models were tested, and the preferred model, based on 56 triangles with a half duration of 2 s, exhibited robust characteristics in the derived landslide force history, unaffected by data selection and source parameterization. Kinematic parameters are deduced from the integration of inverted forces. The trajectory is adjusted to conform to ground observations providing an estimate of the mass. Using a mass of 55×10^9 kg yielded an inverted trajectory that best aligns with the source area, the travel path geometry, and the run-out distance estimated from direct observations.

(g) Bathymetry data

The bathymetry of Dickson Fjord was surveyed in the summer of 2018 by the National Danish Hydrographic Office for the production of nautical charts (Fig. S2). These data have not been previously published. The data are given as a 15 m grid and are available from our supplementary repository (*61*). Due to the previously uncharted nature of the fjord system, the survey vessel could not go too close to the shore, leaving a 150 to 300 m wide and up to 200 m deep coastal gap where no data are available. Outside Dickson Fjord, the 2018 bathymetric data are supplemented with publicly available bathymetry from the General Bathymetric Chart of the Oceans GEBCO (*55*).

To conduct various numerical simulations, whether for the avalanche phase or the tsunami itself, we used a robust method to assemble the altimetric and bathymetric grids. It was crucial to preserve the main characteristics, such as slopes while eliminating the aliasing effects that often affect interpolated grids. To achieve this, we transformed the altimetric and bathymetric grids into point clouds. This allowed us to place the two data sources within the same reference frame, even if they initially had different spatial sampling. We then applied algorithms with adjustable tension splines and continuous curvature, which allowed us to properly interpolate the data in "gap" areas, primarily near shorelines, while minimizing the aliasing effects related to the oversampling necessary for numerical simulations. This approach led to a proper interpolation grid with absence of gaps at shorelines and a minimal aliasing suitable for the simulations.

(h) Tsunami modeling

Modeling of the tsunami generation, propagation, and runup height was performed using two different sets of models.

The first model was used for modeling the tsunami inundation and tide gauge recording at Ella Ø, complementing the HySEA simulations of modeling the long term seiche propagation (more details are given in text S6). This model couples the linear dispersive GloBouss (linearized first-order Boussinesq approximation) model for tsunami propagation (*84*, *85*) with the nonlinear shallow water MOST model (*86*) simulating tsunami inundation through three levels of nested high-resolution grids. Both GloBouss and MOST use finite difference discretisation to model the wave propagation. A rigid block source with prescribed velocity and trajectory was used for simulating the time-dependent volume displacement within the tsunami model following procedures previously used for hazard assessment and hindcasts (*6*, *87*, *88*). The height of the block was set to 130 m with an impact velocity of 90 m/s. The tsunami generation was then taken into account through the flux term in the volume conservation equation (eq. 2 in (*84*)). In addition, we run a time dependent Kajiura filter (*7*) that smooths the wave during tsunami generation to reduce noise in the trailing wave system. As the tsunami model used is linearised, modeling of the impact and near-field effects is simplified. To correct for this simplification, and also empirically take into account additional unmodeled effects such as the bulking factor (mixing of air with the landslide) and landslide entrainment, a correction factor for the effective landslide impact area was embedded into the setup of the block volume. The correction factor used here is 2.0 (i.e., the frontal area is increased by a factor of two), and also complies with the previous experience of past efforts in modeling rock slide tsunamis in the laboratory (*6*, *87*).

As the volume and dynamics of the landslide were highly uncertain right after the event had occurred, we performed a simple sensitivity study running simulations with block volumes 5, 10, and 25×10^6 m^3. The initial impact speed, the run-out distance, and the frontal area for the block model were established for each scenario using the landslide dynamics model VoellmyClaw (*89*). For the simulation of the tsunami propagation in the fjord, we resampled the GEBCO 30’ bathymetry to 100

m resolution. For simulating the inundation at Ella Ø we resampled local topographic data interpolated with GEBCO data for the bathymetry to provide a 5 m resolution inner computational grid. A Manning friction of 0.03 was used for the inundation modeling. For the offshore propagation modeling, friction was not included.

Simulated tsunami heights (relative to still water) at the tidal gauge station in Dickson Fjord have wave periods of ~80 s (trailing the higher and longer leading waves) and amplitudes up to 5 m (Fig. 1). Further east, near Ella Ø and in the two synthetic stations labeled gauge "1" and gauge "2" placed in Kempe Fjord, the leading amplitudes are reduced to 2 m, and the first wave arrival exhibits increased wave periods of about 5 minutes, followed by a higher frequency trailing wave system with wave periods less than 100 s. In Kong Oscar Fjord, the leading offshore wave amplitudes are reduced to less than 50 cm, and wave periods of the leading waves are about 10 minutes. At Ella Ø, simulated runup heights, conducted by adding a 0.7 m height of the tide at the time of the landslide impact, compare closely with the observed trim line. This shows that the initial amplitude and runup, which are controlled by the first phase of the tsunami propagation, are well captured by the model. We stress that GloBouss does not include damping terms such as bottom friction and therefore may underestimate long term wave damping somewhat, in particular for shorter frequency waves. Hence, the long term signal may be more contaminated with numerical noise, providing slightly lower damping values than HySEA.

In addition to the former models, we also performed simulations with the two-layer nonlinear HySEA model (*39*) that simulates the coupled motion of the landslide and of the generated tsunami waves with the hydrostatic approximation (*9*). Indeed, the objective here was to capture the long duration seiche oscillation near the landslide source, which has a wavelength much larger than the water depth, compatible with the hydrostatic approximation. HySEA has been extended from an initial model (*90*) and uses Cartesian coordinates and multilayer approach. HySEA uses a finite volume scheme for modeling the wave propagation. As in most landslide-generated tsunami models, the fluid and the granular mass are assumed to be shallow, incompressible, and homogeneous, and the equations governing landslide dynamics are depth-averaged to handle simulations on complex topography with a reasonable computational cost. As a result, the landslide is considered an effective granular media described by an empirical rheological law (*30*). We use the $\mu(I)$ rheology (*92*) that makes it possible to reproduce the main characteristics of some landslide dynamics and deposits (*37*, *56*, *92*, *93*). HySEA has been successfully used to simulate tsunamis generated by landslides at the laboratory and field scale (*9*, *39*, *56*, *94*, *95*).

We used friction coefficients for the granular mass similar to previous papers (μ_1=7°, μ_2=17°, and μ_3=9° with a characteristic grain size of 1 m). We tested several values of the friction between the landslide and the water layer (m_l=0 and 2×10^{-5}) as well as different Manning coefficients representing the friction between the water and the bottom (n = 0.00, 0.02, 0.03); (Fig. S5). All these simulations make it possible to recover a tsunami wave with a period of ~87 s, consistent with the VLP signal. Uncertainties in the shallow bathymetry may lead to errors in the simulated period of about ±10 s (SEM) based on analytical eigenfrequency solutions (*42*).

(i) Long-period seismic analysis

(1) Data and preprocessing

To gather a comprehensive dataset, we accessed global public seismic data from the International Federation of Digital Seismograph Networks (FDSN) web services, supplemented by the inclusion

of data from the Danish seismic network in Greenland (network code: DK). FDSN codes for seismic networks used (with citations where they exist): AB, AK (*96*), AW (*97*), AZ (*98*), BE (*99*), BK (*100*), C, C0 (*101*), C1 (*102*), CH (*103*), CI (*104*), CO (*105*), CU (*106*), CX (*107*), DK, EE, EP, FN, FR (*108*), G (*109*), GE (*110*), GO, GR (*111*), GS (*112*), GU (*113)*, HK, IC (*114*), II (*115*, *116*), IU (*117*), IV (*118*), IW (*119*), KC (*120*), LD (*121*), LX (*122*), MC, MM (*123*), MN (*124*), MS, MY, N4 (*125*), NA (*126*), NC (*127*), NE (*125*), NL (*126*), NM, NR (*128*), NU (*129*), NW, NZ (*130*), OO (*131*), PB, PL, PM (*132*), PS, PY(*133*), RM (*134*), RN (*135*), SB (*136*) SC, SG (*137*), SL (*138*), SV, SX (*139*), TH (*140*), TW (*141*), UP (*142*), US (*143*), WI (*144*), WM (*145*), WW (*146*), WY (*147*).

Where necessary, we applied a bandpass filter centered around the frequency of 10.88 millihertz (mHz). This allowed us to isolate the seismic energy specifically associated with the VLP. Where relevant, filter parameters are given in the legend or caption of the figures.

(2) VLP frequency analysis

We inspected Fourier amplitude spectra of 5-hour-long data windows and monitored how the VLP peak frequency changed as we slid the window along the time series in increments of 1 hour. The vertical component data of 45 GSN and GEOSCOPE stations were analyzed. The steel blue curve shows the prediction of the ocean tide at Dickson Fjord (Fig. S14). For the given time window, it has a peak-to-peak amplitude of 1.3 m and is dominated by semidiurnal variations. Both the VLP and the ocean tide show a clear, in-phase semidiurnal component such that high ocean tides coincide with a long VLP signal period (i.e., low frequency). This observation indicates a causal relationship between the ocean tides and the transverse seiche that generates the seismic VLP signal.

(3) Simulated seiche and VLP seismic signal amplitude decay

The observed slow decay of the seismic VLP signal over multiple days allows us to immediately reject the hypothesis of a seismic source consisting of a single 92 s pulse exciting the Earth's normal modes, as the resulting signal would then attenuate much more rapidly: fundamental mode Rayleigh waves at these periods have a quality factor of a harmonic oscillator, $Q = 117$ (*50*, *148*) so that the signal would decay to 1% of its initial amplitude in less than 5 hours. The slower energy decay is therefore linked to the source duration itself, which needs to be long enough to explain the 9 days of seismic records.

The frequencies and Q of selected VLP events are shown in Figs. S22-S24 and in Table S1. For the larger VLP events, there is a clear transition within the first 10 hours from low- to high-Q.

Having established that the VLP signal is not from a seismic free oscillation of the Earth, the question arises if we can observe signs of re-excitations. A tool to do this is the so-called phasor walk. The phasor walk is an analytical tool used in seismology to monitor the frequency and phase changes of narrow-band signals (*149*) over time. In particular, a phasor walk is a graphic representation of how the complex Fourier coefficient at a particular frequency grows with the length of the time series. Phase jumps manifest themselves as directional changes in the phasor walk. Such phase changes would be expected in the case of random re-excitations of the oscillator that drives the seismic VLP signal. Examples of such re-excitations could be multiple small rockslides or wind gusts. In Fig. S7 we show three phasor-walks for a vertical component VLP recording at BFO. The slow and smooth curvature of these walks can be attributed to the frequency variation (Fig. S14). The lack of any abrupt change in the direction of the phasor walks shows that the signal does not contain any phase jumps and thus allows us to argue against a source involving random re-excitation.

(4) Polarization of VLP ground motion

Fig. 5A was generated by considering the polarization attributes of the VLP signal for select, high-quality global and regional seismic stations. Three-component ground velocity data for each station were downloaded from the EarthScope Data Management Center (DMC) using the Python package ObsPy (*150*, *151*). Horizontal component data were then bandpass-filtered between 83.6 s and 100 s periods before being rotated into radial and transverse components assuming a source location of 72.5° N, 27.3° W (Table S2). The waveforms from each station were then plotted (e.g., Fig. 5C) and visually inspected for transients from earthquakes (rare) or pressure disturbances (*152–154*). The latter was a ubiquitous problem and excluded many regional and national network stations from further analysis due to tilt noise (*155*) generated on these predominantly near-surface stations with modest installation infrastructure, especially for horizontal components. Therefore, this analysis relies heavily on data from global seismic networks that benefit from extensive infrastructure (including borehole seismometer installations) and very broadband (i.e., 360 s corner period) seismometers (*44*).

For stations deemed to have recorded the VLP signal on both the transverse and radial components with high fidelity, a 5-hour window was selected beginning 3 hours after the landslide origin time. This time window was selected to avoid contamination of long-period (LP) signals associated with the landslide itself and to avoid surface waves generated by teleseismic earthquakes. The root-mean-square (RMS) ground velocity for both the radial (R) and transverse (T) components was taken for the 5-hour window and the Love factor (LF) is defined as:

$$LF = Log_{10}\left(\frac{T_{RMS}}{R_{RMS}}\right)$$

Values of LF > 0 indicate that the VLP signal at a given station is dominated by Love waves, while LF < 0 indicate predominantly Rayleigh wave excitation.

Figs. S25-S27 display polarization analyses for the VLP signal recorded at teleseismic distances on 2023-09-16. Stations are: II.ALE (11.85° epicentral distance, Fig. 5A), IU.KEV (16.97°, Fig. 5A), and IU.SFJD (9.89°, Fig. 5A). Distances and azimuths are computed relative to the center of Dickson Fjord near the gully of the landslide (72.83°N, 27.00°W). Horizontal components are rotated to radial and transverse. IU.KEV and IU.SFJD are near the great circle along the long axis of Dickson Fjord, where dominant Love waves and SH body waves are radiated at the fundamental frequency (Fig. 5A). II.ALE is near the perpendicular direction with dominant Rayleigh wave and P-SV body wave radiation. The signals are bandpass-filtered from 9 mHz to 25 mHz, which covers the fundamental frequency (10.88 mHz) and the first overtone (21.76 mHz). A time window beginning at 15:30 UT was selected, to avoid short-period transients at the time of the VLP onset and to avoid surface waves from the Mid-Indian Ridge earthquake (moment magnitude, M_w 5.4, 13:47:58.09 UTC). For each station, the diagrams show polarization (radial-tranverse [R-T], radial-vertical [R-Z], and vertical-transverse [Z-T]; notice the inverted Z-scale on R-Z), fast fourier transform (FFT) spectra (mid-right), where all curves are normalized to the largest peak of all on a linear amplitude scale, and the time series in units of acceleration (bottom).

(5) Source Location of the VLP signal from beamforming

We beamform global recordings of the 92 s VLP signal to estimate its source location. Beamforming (here synonymous with matched field processing) is a phase-matching algorithm to determine the origin and velocity of a wavefield propagating across an array of sensors by exploiting the coherency of the wavefield across the array (*156*, *157*). It does not require the abstraction of waveforms, such as

picking onsets of certain seismic phases, and is therefore suitable for near-monochromatic signals (*158*). We use cross-correlation beamforming (*159*) in a narrow frequency band from ca. 10-12 mHz to account for the 0.02 mHz variation in frequency over time (Figs. S7, S14).

We establish here that the recorded vertical component VLP signal is composed of Rayleigh waves by grid-searching in latitude, longitude, and homogeneous phase velocity using 997 vertical component seismograms recorded worldwide during the first 12 hours after the landslide (red star in Fig. S3). From 1488 publicly available seismograms, we select the 997 (67%) most coherent to ensure that we beamform quality recordings. We find a best-fit location at 68.3 km distance to the landslide for a phase velocity of 4.1 km/s (orange diamond in Fig. S3). The detected phase velocity is consistent with theoretical fundamental mode Rayleigh wave phase velocities for the Preliminary Reference Earth Model (PREM) at 92 s period (*50*).

To account for a heterogeneous Earth, including effects such as off-great-circle propagation, we compute a Rayleigh wave phase velocity model for a 92 s period. The model is the linear interpolation of the 10 mHz (100 s) and 15 mHz (66.6 s) LITHO1.0 velocity models (*160*). We estimate expected minor arc phase travel times from this model by the Fast Marching Method to use for beamforming (*161–163*). With the heterogeneous velocity model, maximum beam powers are consistently 25% higher than for the best-fitting homogeneous Earth model, whereas amplitudes of side maxima are reduced, indicating that this location is better constrained. The back-projected location is farther to the east (orange square in Fig. S3) at 92.3 km distance to the landslide and 68 km distance to the best-fitting location for a homogeneous Earth model. Both estimated locations are substantially less than one wavelength apart ≈380 km) from the landslide.

The estimated location is exceptionally stable through time, confirmed by beamforming in overlapping 2-hour windows over the first 10 days after the event (movie S3). The movie shows beampower distributions normalized for each time window. The 92 s VLP signal can be detected by beamforming for about 1 week, as seen in the movie and Fig. 5D. As the amplitude of the signal decreases with time, the source location can only be detected with the global network during quiet times when no other substantial sources, such as earthquakes, are present.

Although there is no comprehensive approach to quantify the uncertainty of beamforming locations and thus the quality of the absolute location (*164*), we find that the source is exceptionally stable in time (detected for ~7 days) and space (minor deviations over these 7 days). The background color in Fig. S3 depicts the beam power distribution for the tested latitude and longitude grid in the heterogeneous Earth model, averaged over the first 12 hours after the landslide. The shape of this distribution results from the near-monochromatic character of the signal, leading to substantial side maxima, as well as the geographic distribution of used seismic stations, which cluster towards the west and northwest (in North America) and southeast (in Central Europe) of the landslide. The beam power distribution resembles the “array response” in classical array seismology and gives only qualitative insight into the resolution capabilities of the network for the given frequency band (*157*, *165*). This means that while the location is stable and does not appear to move over time, the precision of the absolute location is unclear. Beamforming, however, does confirm that the source of the 92s VLP signal is in the vicinity of the landslide and Dickson Fjord, within a distance of one-quarter of the signal wavelength.

We provide all codes necessary for downloading and pre-processing the seismograms from public repositories, computing the beampowers (*166*), and reproducing these results (*61*).

(6) Numerical simulation of the VLP signal

We consider a simplified fjord geometry, as in Fig. S28. A seiche in the fjord, oscillating in the y-direction, will generate two sets of oscillating forces:

- Two vertical forces, F_{v+} and F_{v-}, acting on the fjord's floor, with equal magnitude and opposite direction. These two forces form a couple.
- Two horizontal forces, F_{h1} and F_{h2}, acting on the fjord's walls, with equal magnitude and equal direction. These two forces do not form a couple and can therefore be added: $F_h = F_{h1} + F_{h2}$,

Note that the magnitudes of the two sets of forces will generally differ.

We consider two stations: STA1 along the axis parallel to the fjord (*x*-axis) and STA2 along the axis perpendicular to the fjord (*y*-axis). We examine the surface wave amplitudes at these two stations generated by each of the two sets of forces.

We first consider the vertical couple (Fig. S29). The two forces will generate radially symmetric (cylindrical) Rayleigh waves with opposite amplitude, *A*:

$$A_{Rv}\left(t-\frac{r^{+}}{V_R}\right) \; and \; -A_{Rv}\left(t-\frac{r^{-}}{V_R}\right)$$

where the subscript *Rv* stands for Rayleigh wave due to the vertical couple, *t* is time, V_R is the Rayleigh phase velocity, and r^+ *and* r^- *are* the distances between the receiver and the positive and negative vertical forces, respectively.

At STA1, $r^+ = r^- = r / \cos\theta$ (Fig. S30), the vertical motion will cancel out, and the horizontal motion, *u*, will be in the *y* direction:

$$u_{y1}(t,r) = 2A_{Rv,r}\left(t-\frac{r/cos\theta}{V_R}\right) sin\,\theta = 2A_{Rv,r}\left(t-\frac{r/cos\theta}{V_R}\right)\frac{d/2}{r/cos\theta}$$
$$= \frac{dcos\theta}{r}A_{Rv,r}\left(t-\frac{r/cos\theta}{V_R}\right)$$

where $A_{Rv,r}$ is the Rayleigh wave radial amplitude.

This motion scales with the distance *d* between the two vertical forces and attenuates with distance as $r^{-1.5}$ (Rayleigh wave spreading, times a further r^{-1} term). The motion is linearly polarized in the *y* direction. It has the same polarization as a Love wave, but it has a phase velocity of a Rayleigh wave.

At STA2, the motion will have a horizontal component in the *y* direction and a vertical component in the *z* direction.

Let's consider the horizontal component first. It is the difference between two amplitudes with a phase shift of d/V_R:

$$u_{y2}(t,r) = A_{Rv,r}\left(t-\frac{r-d/2}{V_R}\right) - A_{Rv,r}\left(t-\frac{r+d/2}{V_R}\right)$$

where we use $r^+ = r\text{-}d/2$ and $r^- = r\text{+}d/2$. This is equivalent to computing the derivative of $A_{Rv,r}$ relative to distance *r* from the barycenter of the forces, multiplied by the distance between forces *d*:

$$u_{y2}(t,r) = d \cdot \frac{dA_{Rv,r}\left(t - \frac{r}{V_R}\right)}{dr}$$

which can be written in terms of time derivative:

$$u_{y2}(t,r) = d \cdot \frac{dt}{dr}\frac{dA_{Rv,r}\left(t - \frac{r}{V_R}\right)}{dt} = \frac{d}{V_R}\dot{A}_{Rv,r}\left(t - \frac{r}{V_R}\right)$$

where the dot above $A_{Rv,r}$ indicates time derivative, and we used $V_R = \mathrm{d}r/\mathrm{d}t$.

This motion scales with the distance d between the two vertical forces, divided by the Rayleigh phase velocity V_R, and attenuates with distance as $r^{-0.5}$ (Rayleigh wave spreading).

Similarly, the vertical component is:

$$u_{z2}(t,r) = \frac{d}{V_R}\dot{A}_{Rv,z}\left(t - \frac{r}{V_R}\right)$$

The motion at station STA2 is thus elliptically polarized in the y-z plane.

We now consider the ground motion produced at stations STA1 and STA2 by the effective horizontal force (Fig. S30). This force is located at the center of the axis system and will produce Love waves along the fjord axis (x-axis), Rayleigh waves along the axis perpendicular to the fjord (y-axis), and a mixture of the two along any other direction.

Station STA1 will receive a Love wave with amplitude:

$$A_{Lh}\left(t - \frac{r}{V_L}\right)$$

where the subscript Lh stands for Love wave due to the horizontal force, V_L is the Love phase velocity, and r is the distance between the source and the receiver. The motion attenuates with distance as $r^{-0.5}$, and is linearly polarized in the y direction (the vertical component is zero).

Station STA2 will receive a Rayleigh wave with amplitude:

$$A_{Rh}\left(t - \frac{r}{V_R}\right)$$

where the subscript Rh stands for Rayleigh wave due to the horizontal force, V_R is the Rayleigh phase velocity, and r is the distance between the source and the receiver. The motion attenuates with distance as $r^{-0.5}$, and is elliptically polarized in the yz plane.

To summarize:

- ground motion along the axis of the fjord (x-axis) is dominated by the Love waves produced by the horizontal force because the motion associated with the vertical couple attenuates rapidly as $r^{-1.5}$;
- ground motion along a direction orthogonal to the fjord axis (y-axis) is a mixture of Rayleigh waves generated by the vertical and horizontal forces.

To test the relative importance of the surface wave motion generated by the two sets of forces, we performed a synthetic test using the same arbitrary magnitude for all the forces. A Jupyter notebook

for reproducing this test ("*seiche_surface_waves.ipynb*") is available (*61*). The notebook makes use of ObsPy (*150*) to access the web services and process seismic traces.

The two vertical forces are separated by d = 2880 m in the y-direction and placed at 540 m of depth (approximate width and depth of the Dickson Fjord); the effective horizontal force is placed at the axis origin and at 540 m of depth. The stations are placed at 400 km of distance (i.e., one wavelength) along the x-axis (STA1) or the y-axis (STA2). Synthetic signals are generated using the EarthScope Synthetics Engine (Syngine) web service (*167*), which serves pre-computed Green's functions calculated using Instaseis (*168*) and AxiSEM (*169*). Here we use the anisotropic PREM model "prem_a_20s", pre-computed in the period interval of 20-100 s. We retrieved a Green's function for each station and each force. By summing Green's functions for each set of forces (vertical and horizontal), we obtain two simulated three-component seismograms at each station, one generated by the vertical forces and the other by the horizontal forces. Finally, we filter the traces between 9 and 13 mHz, i.e., around the observed frequency of the seiche (10.88 mHz). For each station, and vertical and horizontal components, we measure the ratio between the peak ground displacement generated by the horizontal forces (PGDh) and the peak ground displacement generated by vertical forces (PGDv). The results are summarized in Table S3. The effective horizontal force is substantially more capable of generating surface waves at both stations.

We therefore performed a direct simulation of the VLP signal recorded at selected stations worldwide (Fig. 5A) using, as the source, a horizontal force oriented along the transverse axis of the Dickson Fjord (N160°E, Fig. 5A), located at the center of the Dickson Fjord, in front of the observed landslide (Fig. 2), at coordinates 72.835°N, -26.985°E; the source is placed at 540 m depth (depth of the fjord at the chosen location). The only free parameter of our direct modeling exercise is the magnitude of the horizontal force.

Synthetic three-component Green's functions are retrieved using the Syngine web service, as described above. We use as a source-time function the normalised simulated time series of the seiche at the location of the landslide (Fig. 4E). This time series comes from our dx = 3 m, Manning = 0.03 HySEA simulation. Synthetic Green's functions and the source time function are convolved to obtain the three-component synthetic displacement signals at each selected station, which are finally compared to real data in the band 9-13 mHz.

After some trial and error, we found that using a horizontal force of 5×10^{11} N produces a satisfactory fit, both in amplitude and phase, at most stations.

Fig. S9 shows, as an example, the good fit between synthetic and observed signals, both filtered between 9 and 13 mHz, for station II.BFO, a station with predominant Rayleigh-wave motion. Fig. S10 shows, for the same station, the comparison of particle motion.

Another example is given in Figs. S11 and S12 for station IU.RSSD, which is a station with predominant Love-wave motion.

A Jupyter notebook for reproducing this forward modeling exercise ("*seiche_surface_waves_modelling.ipynb*") is available (*61*) and can be used to check the goodness of fit at any seismic station for which data are available from the EarthScope DMC Web Services. The notebook makes use of ObsPy (*150*) to access the web services and process seismic traces.

(7) The seiche as the source of the VLP signal

The radiation pattern, duration, and amplitude of the teleseismic VLP signal are consistent with a point source expressed as a horizontal force of 5×10^{11} N. The force is parallel to N160°N, which is perpendicular to the axis of Dickson Fjord, and its force-time-function oscillates at 92 s period with a slowly decaying amplitude. This has been demonstrated by the computation of synthetic seismograms and quantitative comparison with teleseismic recordings and is discussed in the preceding section.

In a seiche oscillating perpendicular to Dickson Fjord, an oscillating horizontal force directed N160°E is needed to provide the necessary transfer of momentum to the center of mass of the oscillating water body. Here, we investigate whether the force amplitude of 5×10^{11} N would be consistent with the seiche amplitude found in the numerical tsunami simulation (Fig. 4E). A Jupyter notebook for reproducing this computation ("*VLPsource_dynamics_triangular.ipynb*") is available (*61*) and can be used to test different sets of input parameters.

We consider a simplified geometry of the cross section of the fjord for an estimation of the order of magnitude of the seiche amplitude. This geometry is shown in Fig. S36 and is defined by the following quantities:

L = 2700 m: width of Dickson Fjord;
h = 540 m: maximum depth of Dickson Fjord;
h_s = 20 m: vertical extent of the wall at the shore to below the water surface;
D = 10 km: section along the fjord, which takes part in the seiche;
Δx: horizontal amplitude of the oscillating center of mass;
Δz: maximum vertical deflection of the water surface at the shore of the fjord.

The total volume of water taking part in the seiche hence is:

$$V = \frac{1}{2}\, L\, (h + h_s)\, D$$

which with the above-defined dimensions is 7.6×10^9 m³ corresponding to a mass m of 7.6×10^{12} kg.

The horizontal location of the center of mass of the sloshing water is $x(t) = \Delta x \sin(\omega t)$

such that its kinematic acceleration becomes $a(t)=x''(t)=-\Delta x\omega^2 \sin(\omega t)$, where x'' is the second derivative of x with respect to time t. The amplitude of the force needed to provide this acceleration then is $F = ma$ with $a = \Delta x\omega^2$ with $\omega = 2\pi/92$s. Hence

$$\Delta x = \frac{F}{m\,\omega^2}$$

which equals 14 m with the above given dimensions and a force amplitude of 5×10^{11} N. For the simplified seiche geometry this corresponds to a vertical deflection Δz of the water surface at the shore by:

$$\Delta x = \frac{L}{3}\frac{\Delta z}{h + h_s}$$

and hence Δz is 8.8 m, which is consistent with the seiche amplitude found in the numerical simulation (Fig. 4E).

The total energy in the sloshing water body equals the maximum kinetic energy:

$$E_{kin} = \frac{1}{2}\, m\, \Delta x\, \omega = 3.5\times10^{12} \text{ J.}$$

This is only a small fraction of the potential energy of the rock mass in the landslide:

$$E_{pot} = V\, \rho\, g\, H = 7\times10^{14} \text{ J}$$

where $V = 2.5\times10^7$ m³ is the volume of rock, $\rho = 2850$ kg m^{-3} is the approximate rock density, $g = 9.81$ m s^{-2} is gravity, and $H = 1000$ m is the approximate height above the fjord of the rock before the collapse. The landslide hence provides more than enough energy to get the seiche oscillation going.

A seiche oscillation of the amplitude computed by numerical simulation with energy input from the rockslide hence provides the transfer of momentum corresponding to a force amplitude of 5×10^{11} N, the source of the observed VLP signal.

(j) GPS data

We processed the Global Navigation Satellite Systems (GNSS) data from regional East Greenland GNSS stations (Fig. S31) using the GIPSY-OASIS software package with high-precision kinematic data processing methods (*170*) with ambiguity resolution using Jet Propulsion Laboratory (JPL)'s orbit and clock products. We use the GIPSY-OASIS version 6.4 developed at JPL (*171*). We use JPL final orbit products, which include satellite orbits, satellite clock parameters, and Earth orientation parameters. The orbit products take the satellite antenna phase center offsets into account. The atmospheric delay parameters are modeled using the Vienna Mapping Function 1 (VMF1) with VMF1grid nominals (*172*). Corrections are applied to remove the solid Earth tide and ocean tidal loading. The amplitudes and phases of the main ocean tidal loading terms are calculated using the Automatic Loading Provider (http://holt.oso.chalmers.se/loading/) applied to the FES2014b ocean tide model including correction for the center of mass motion of the Earth due to the ocean tides. The site coordinates are computed in the IGS14 frame (*173*). We convert the cartesian coordinates at 30 s intervals to local up, north, and east coordinates for each GNSS station monitored at bedrock in east Greenland (Fig. S32).

The GNSS data show no substantial vertical or horizontal displacement from by the landslide. The distance between the stations and the center of the landslide is too large to have recorded it.

Supplementary Text

Text S1: Landslide nomenclature

We follow the landslide nomenclature of Hungr et al. (*174*) in this paper. We thus use the term "landslide" to describe the broad overall mass movement event on the slope that occurred on 16 September 2023.

It is a delicate balance between using specific process-related names (-slide, - avalanche) and at the same time avoiding too complex descriptions. A problematic aspect is that the landslide changed name down the slope from an initial rockslide to a rock-ice avalanche. It can thus be confusing to refer to one or the other. We have chosen to refer to the landslide as a rockslide for the most part, but in some cases used the broader term landslide when referring to the whole sequence of mass movement.

When referring to the other mass movements that have occurred on the slope (Table S1), we call them landslides as we do not know enough about them to assign a specific process, and even material, to them.

Text S2: Physiography and climate of Dickson Fjord

Dickson Fjord is situated in the northernmost area of the Kong Oscar Fjord system and is connected to Kempe Fjord together with Røhss Fjord and Rhedin Fjord. From its mouth north of Kempe Fjord it stretches northwestward for about 15 km and then roughly east-west for 23 km. The fjord is 38 km long and 2.5-3.2 km wide, and fills a glacially carved U-shaped valley with depths from 150-200 m in the western part and down to 700 m in the eastern part. The surrounding up to 60° steep coastal slopes stretch up to c 2000 m above sea level. Several smaller land-terminating glaciers are found on both sides of the inner Dickson Fjord. The nameless glacier (informally termed "student glacier" by scientists working in the fjord) where the present landslides have occurred is a narrow 200 m wide marine-terminating glacier connected to Hvide Støvhorn (*175*). This glacier stands on a 220 m wide and 80 m long sediment peninsula on the south side of Dickson Fjord with a water depth of 20-40 m just in front of the glacier and down to 540 m in the center of Dickson Fjord 1500 m from the terminus of the glacier. At the head of Dickson Fjord, the larger Hissinger Glacier has its terminus.

The climate in Dickson Fjord is characterized by a long cold winter and short, cool summer. The fjord is situated 700 km north of the Arctic Circle, where the midnight sun characterizes the summer and darkness prevails during winter. The duration of the summer midnight sun and the winter polar night periods in the area is 93 days and 75 days, respectively, with a maximum incoming radiation of 750 W/m^2 during summer. Winters are generally very cold, with mean monthly temperatures as low as -30°C. Mean temperatures at sea level are below freezing 9 months of the year, and only the months June to August have positive mean air temperatures of up to +5°C. The whole of northeast Greenland is characterized by continuous permafrost, and the mean annual ground temperature in the Dickson Fjord area is modeled to be -8°C (*176*). The mean annual wind velocity in the area is 4.5 m/s, most frequently coming from the north. However, during June–August the dominant wind direction is easterly. Precipitation data are currently not available for the Dickson Fjord, but 200 km north at the Zackenberg Research station, it varies from 214 to 320 mm, approximately 75% of which is snow. Snow cover is usually formed in September and disappears through June–July. Fast ice in the fjord breaks in July, and new ice begins to form in late September and early October. The area is currently warming and subject to an increase in freshening from river discharge and melting of sea ice and glaciers (*38*, *177*).

Text S3: Brief geological setting

Northeast Greenland is structurally dominated by the Silurian - Devonian Caledonian orogeny that deformed the bedrock in north-south oriented folds and thrusts (*178*). In Dickson Fjord, the bedrock consists of Archean orthogneiss with intervals of pelitic sediments and marble and is intensely veined by pegmatites of muscovite-granite composition. Where the rockslide started, the foliation (i.e., the internal layering of the metamorphic rock) is dipping ~45° towards the west, although detailed structural information from the fjord is scarce (*179*).

Text S4: Other events in Dickson Fjord from satellite data

Three visually confirmed (by satellite images) precursor landslides occurred in 2013-2014, 2016, and 2017 from the same gully as the 2023-09-16 rock/ice avalanche (Table S1). These all occurred in the dark winter season without optical satellite coverage and ran out on the fjord sea ice without penetrating it. They could be recognized in Sentinel-1 Synthetic Aperture Radar (SAR) scenes and in early summer (June) Landsat 8-9 and Sentinel-2 satellite scenes when the snow on the sea ice is melted. Observations from satellite images of these landslides are briefly listed below to show that at least two of the events (2016 and 2017) correlate with VLP events. No VLP signal has been identified for the landslide that occurred in the winter of 2013/2014. Further research into their dynamics and tsunamigenic potential would be beneficial; this is, however, beyond the scope of the present paper. All open-access satellite images (Landsat: 1972-present, Sentinel-2: 2015-present) from Dickson Fjord were manually examined. No landslide events could be observed for the two seismologically observed VLP events in 2005 and 2006 (Table S1), but these both occurred in August when no show or sea ice was available to capture the traces of the possible associated landslide events.

a) The 2013-09-30 to 2014-03-02 landslide

A landslide deposit is seen on a Landsat 8-9 scene from 2014-06-11 after the snowmelt (Fig. S33a). Further analysis of Landsat 8-9 scenes shows that the event must have happened between 2013-09-30 (last scene of 2013) and 2014-03-02 (first scene of 2014). The deposit has a run out of 1050 m from the shoreline onto the ice and an area of 0.75 km^2. The glacier in the gully above the landslide is covered with debris in places, but no clear landslide scar can be identified. No seismic signal or VLP has been found for the event.

b) The 2016-02-12 landslide

A landslide deposit is seen on a Landsat 8-9 scene from 2016-06-07 after the snowmelt (Fig. S30b). Analysis of Sentinel-1 scenes and the identification of a VLP seismic signal show that the event happened at 2016-02-12 04:12 UTC (Figs. S7 & S31). The deposit has a run-out of 930 m from the shoreline onto the ice and an area of 0.56 km^2. The glacier in the gully above the landslide is covered with debris in places but no clear landslide scar can be identified.

c) The 2017-01-20 landslide

The landslide deposit is seen on a Sentinel-2 scene from 2017-06-15 after the snowmelt (Fig. S32c). Analysis of Sentinel-1 scenes and the identification of a VLP seismic signal show that the event happened at 2017-01-20 08:10 UTC (Figs. S12 & S32). The deposit has a run-out of 1050 m from the shoreline onto the ice and an area of 1.29 km^2. The deposit is asymmetrical, stretching towards the west. Three secondary features are observed that are not seen in the two previous events: (1) a distinct pattern in the snow cover on the ice indicates that the snow is thinner in a ~1200 m wide halo around

the deposit and potentially arranged in radial ridges. (2) Fractures in the sea ice concentric to the landslide deposits are seen both just next to the deposit but also at 500 to 1100 m from the deposit. (3) Seemingly randomly oriented fractured ice is observed in the fjord farther from the landslide than the concentric fractures. The glacier in the gully above the landslide is covered with debris in places, but no clear landslide scar can be identified. The randomly fractured sea ice is atypical for normal fjord ice, and we interpret this as an indication of tsunami activity in the fjord following the landslide.

d) October 2023-10-11 landslide and tsunami

Twenty-five days after the rock-ice avalanche of 2023-09-16, described in the main text, a new landslide occurred in the gully. The event was first recognized in the seismic record as it produced a VLP. A Sentinel-2 satellite image from 2013-10-13 showed that the glacier in the gully was now eroded even more than during the September 16th event, and the part of the glacier protruding into Dickson Fjord was also further reduced in size. No clear new landslide scar has been observed, but the glacier is dirtier after the event at a higher elevation than before.

Tsunami runup could be observed in the images in two places: 200 m west of the mouth of the gully 60 m runup was mapped. Here, 80 m runup was observed after the September 16th tsunami. 40 km (by waterway) from the source in Røhss Fjord, a vertical runup of 2 to 6 m was mapped versus 3 to 10 m in the September 16th event (Fig. S33).

Field validation was not possible for this event because the Danish military does not patrol by boat this late in the season and the Air Force surveillance plane was not available. Furthermore, open-access satellite acquisition stops in this region in late October due to arctic winter darkness.

We interpret the above event to be a minor (relative to the September 16th) landslide that entrained a large portion of the glacier. The initial landslide might have been composed of material deposited in the impact area of the gully after the September 16th rock-ice avalanche (Fig. 2F) or be a minor rockslide from the back-scarp of the September 16th rockslide.

Text S5: Destruction of cultural heritage and implications for event return rate

At Kap Hedlund, 35 km from the landslide by waterway, the 2023-09-16 tsunami had a vertical runup of up to 13 m (Fig. S35). Here a trapper hut from 1934 was replaced by a new hut in 1964 called Kap Hedlund Hytten. The exact elevation of this hut is unknown, but it was destroyed in the 2023-09-16 tsunami (Fig. S34b,c). 400 m to the north, a Thule Culture Inuit site with remnants of three winter houses have been reported located 1 to 1.3 m above the high water mark (*180*, *181*). The age of this site is unknown but the last sighting of Thule Culture Inuits from North East Greenland is from 1823. The conditions of these sites after the 2023-09-16 tsunami are unknown, but the low elevation and the destruction observed at the Kap Hedlund Hytten and in satellite images lead us to conclude that this site is destroyed. Several other cultural heritage sites of the Thule Culture Inuit and trapper era are present in the fjord system (Fig. 4B), and we expect that all the low-lying sites are affected by the 2023-09-16 tsunami, but a comprehensive documentation of this is beyond the scope of the present paper.

Apart from documenting the destructive force of the tsunami, these cultural heritage sites demonstrate that the 2023-09-16 tsunami is more than a ~one in 200-year event because the Thule Culture Inuit site older than 1823 would have been destroyed if such an event had occurred in this period.

Text S6: Supplementary tsunami simulations for wave damping

A set of simulation tests have been carried out to investigate the wave damping within Dickson Fjord to provide an independent test to compare with the long duration HySEA simulations. For this we have used the dispersive GloBouss model (*43*, *43*, *84*, *85*).

Simulations are extended in duration and run at a much finer spatial resolution. GloBouss is run in *linear shallow water* (LSW) mode in which there is no dispersion or non-linearity. We extract two wave signals, one in the middle of the fjord (gauge A) and one in the eastern fjord bend (gauge B); see the extent of the computational domain and analysis results in Figs. S37 and S38, respectively. A noteworthy finding is that the first eigenmode found in the signal at gauge A (wave period of ~85 s) is almost not present farther out-fjord at gauge B, an indication that the first eigenmode is mostly trapped to the inner part of the fjord. The computed Q-values in Fig. S40 also confirms this weaker dissipation of the seiche in the inner fjord. Because of the simple numerical finite difference representation of the wave modeling in GloBouss, the long-term propagation gives rise to excessively noisy wave components of relatively high frequency that become more prominent when the wave simulations are run for a very long time. Hence, to monitor the damping of the most relevant low frequency part of the wave spectrum, we evaluate the time series from a time series subject to lowpass-filter with a cutoff at 0.03 Hz. To this end, we first take the FFT of a time series output from GloBouss at the gauge location, apply a simple cosine-squared with a width of the transition zone of 0.01 Hz, and then run an inverse-FFT to retrieve the filtered time series solution. This leaves wave components up to about one-third of the dominant wave period. We further compare the result with the unfiltered solution taken directly from GloBouss. The original and lowpass-filtered signal have similar Q-values of ~2000. Due to the noisy behavior of GloBouss, the frequency pattern does not reveal the same clear almost monochromatic signal as HySEA, but still, the first eigenmode (~0.012 Hz, wave period ~85 s) and the first subharmonic (~0.024 Hz, wave period ~43 s) frequency is found in the spectrum.

Grid refinement convergence tests show that the longer leading waves are reproduced similarly for different grid resolutions and that the Q-value (here roughly representing the envelope of the amplitudes over time) is retained for different resolutions (Fig. S39). With respect to the frequency spectrum, we see a similar pattern for the longer waves for different grid sizes, but with larger deviations for short waves (frequency less than 0.03 Hz). On the other hand, with the long duration signal in mind, it is not possible to avoid phase deviations appearing in the trailing waves for different grid spacings. The simulations give converging amplitude envelopes for the two grid resolutions of 12.5 m and 25.0 m, for gauge A a Q-value ~3000, for gauge B a value of ~2000. This shows that the Q-values are unchanged with increasing spatial resolution for the GloBouss simulations, which supports the finding of a relatively low damping value (high Q-value) for the seiche wave in the inner fjord domain found using HySEA. The convergence of the amplitude envelope for lowpass-filtered signal shows the same results, shown in Fig. S40.

Supplementary Figures

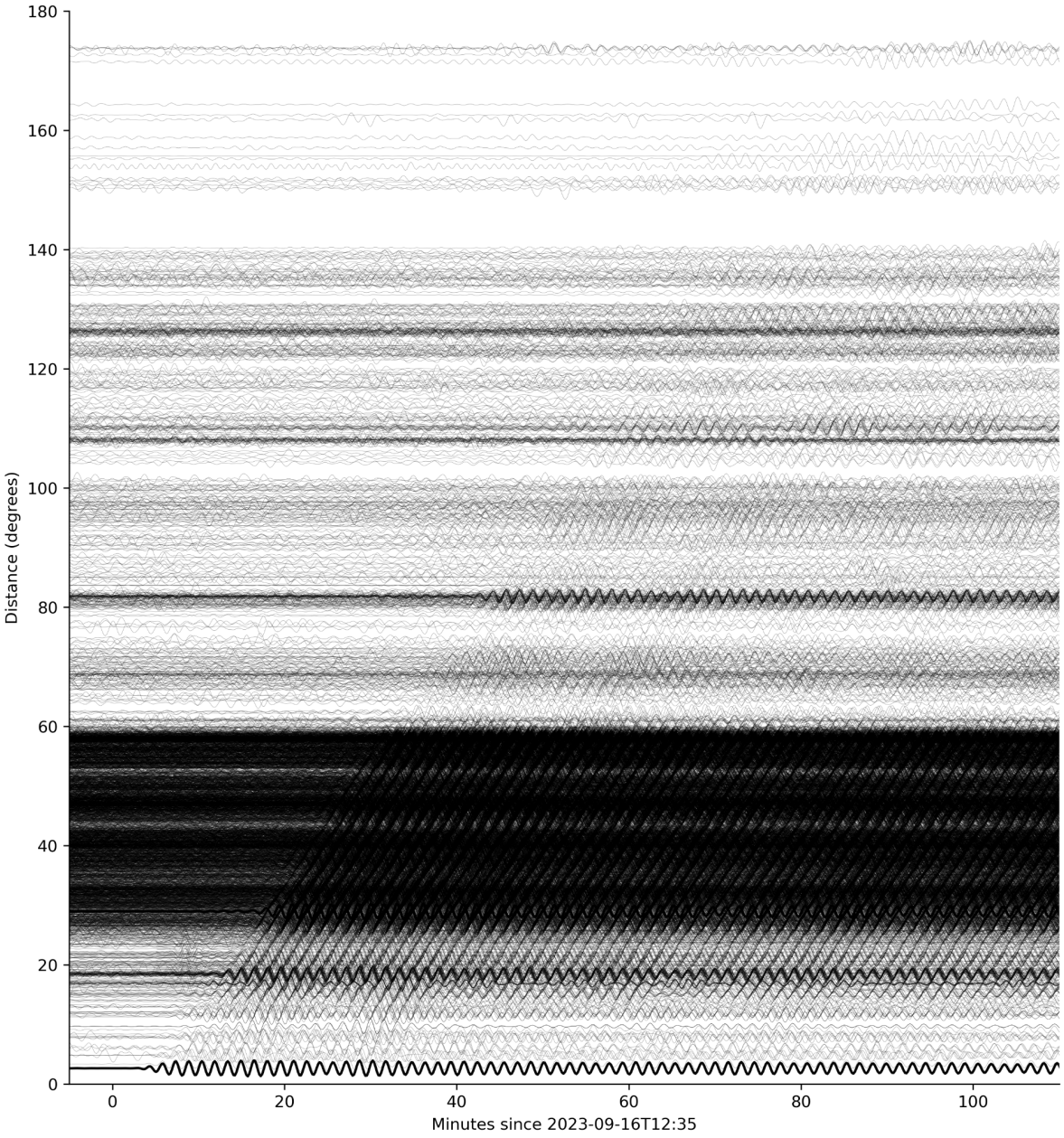

Fig. S1: *Seismic record section, plotted in the same way as Fig. 1A, but waveforms are filtered between 80 s and 100 s period and are shown to a larger distance range, showing the very long-period (VLP) seismic signal propagating around the world.*

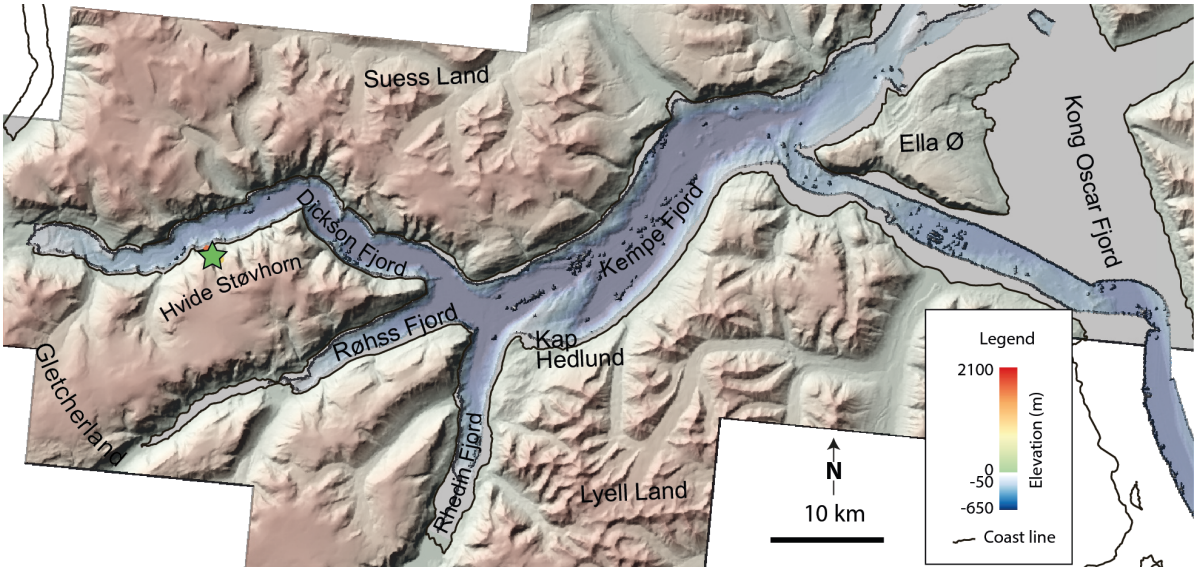

Fig. S2: *Render of the new bathymetry used in the tsunami modeling. Onshore, a 10 m DEM from SDFI is shown (69). The landslide area is depicted with a green star.*

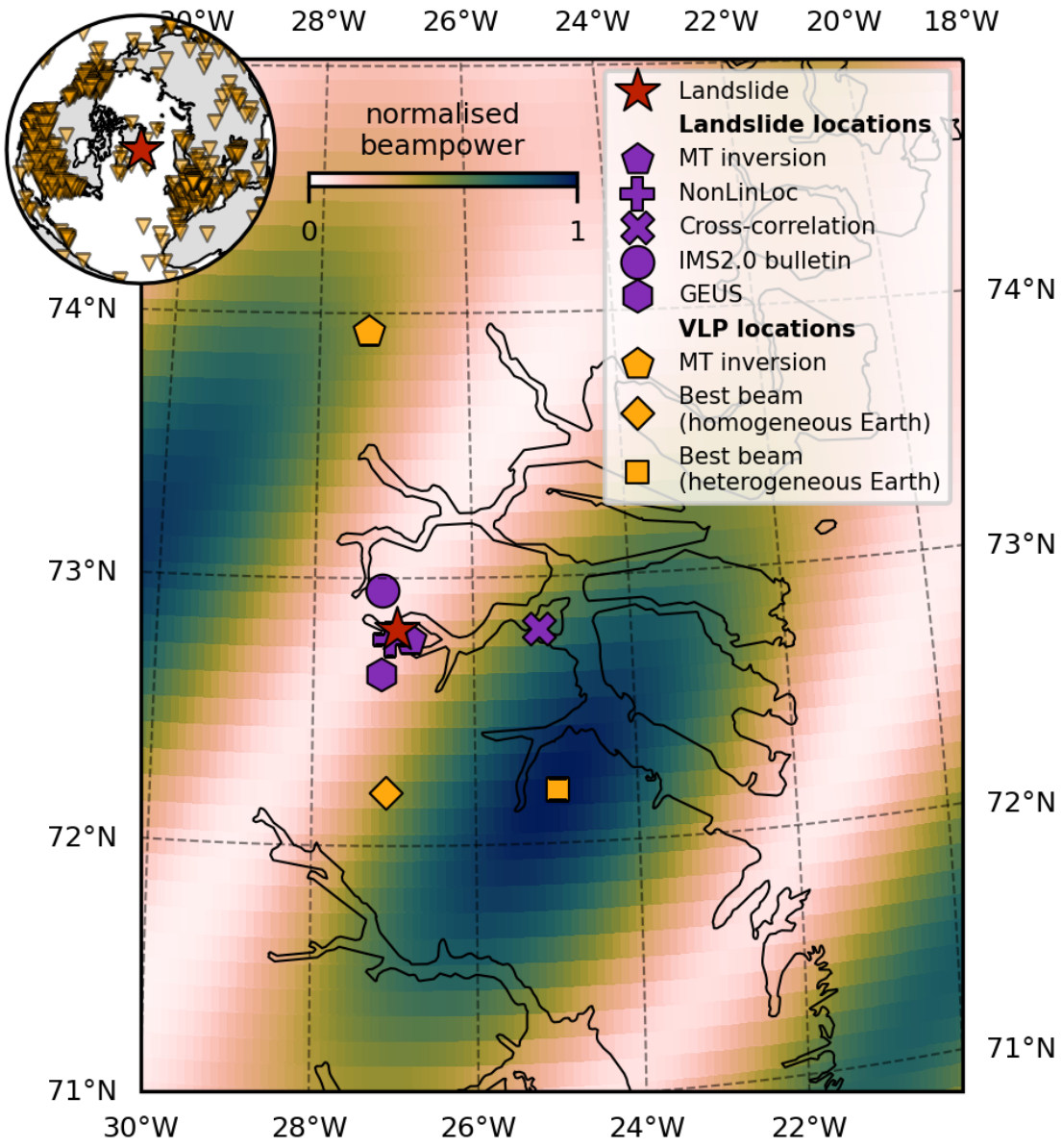

Fig. S3*: Locations estimated from seismic data for the landslide (purple markers) and the very long-period (VLP) signal (orange markers) using different methods and data (Table S2). Background colors indicate the beampower distribution for the location of the VLP signal for the heterogeneous Earth model. Inset top left: map of the 997 stations used for beamforming, dominantly located in North America and Central Europe.*

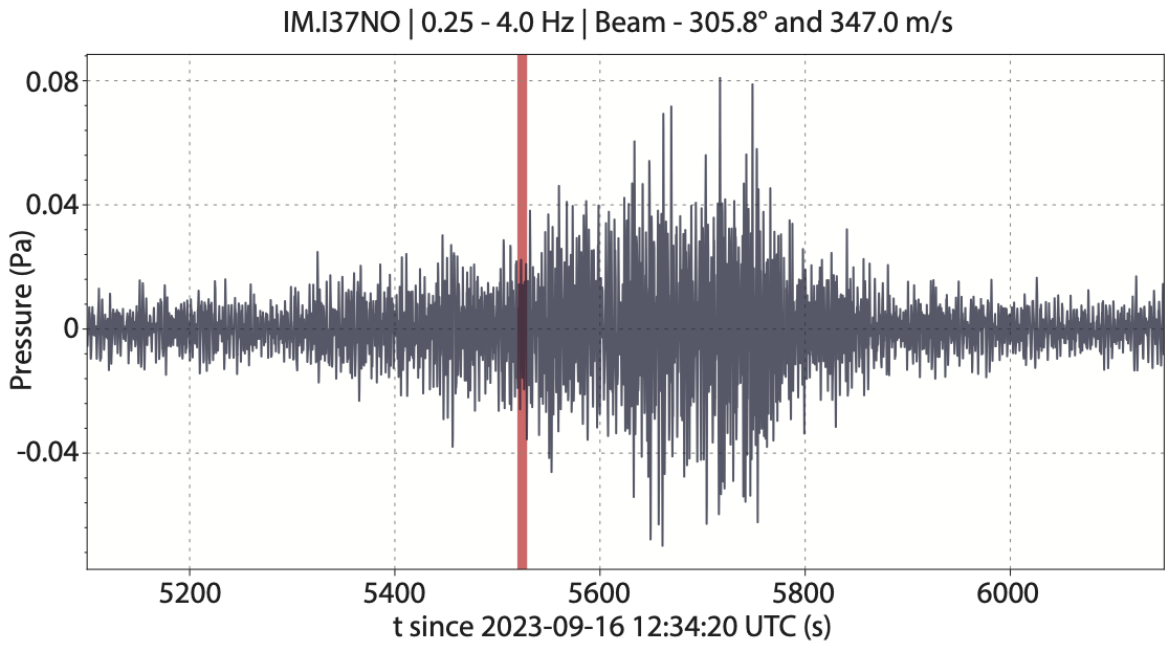

Fig. S4: *Acoustic signal recorded at infrasound array I37NO in northern Norway (1667 km distance). The ray theoretical arrival time is indicated by the vertical red line. "t" in the x-axis label = "time".*

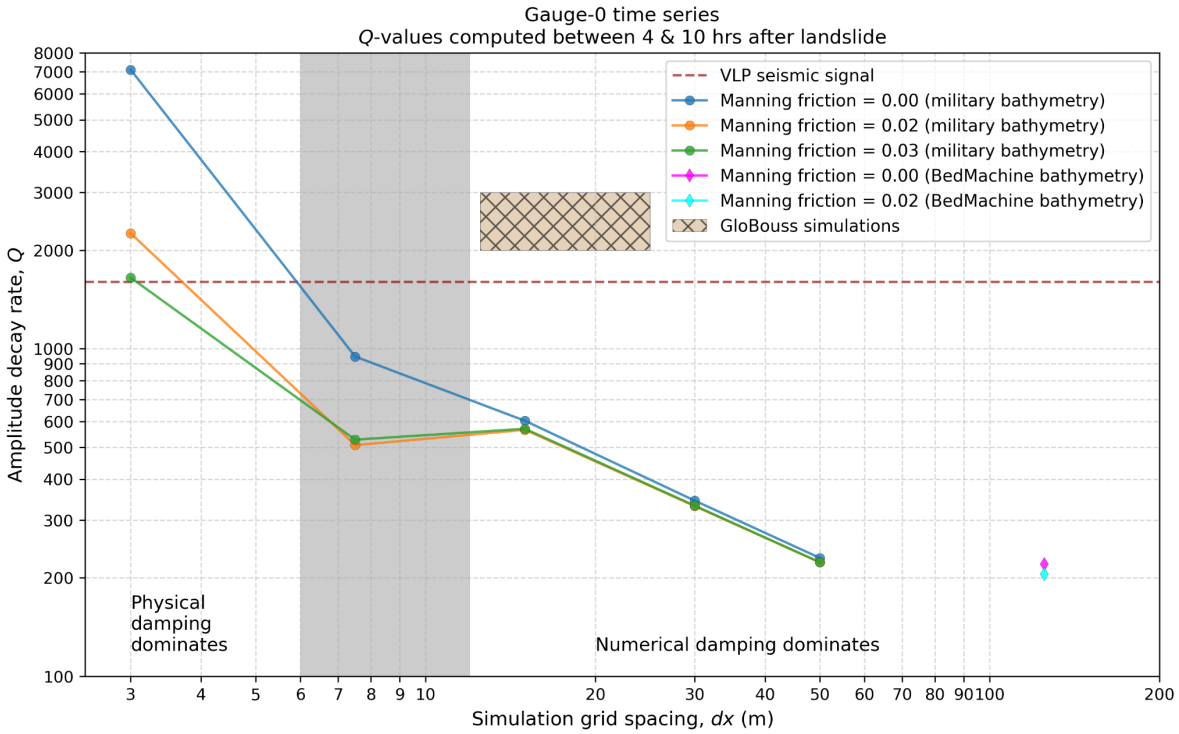

Fig. S5: *Seiche decay rates (Q-values) at the landslide location for HySEA tsunami simulations using different model grid spacing, bathymetry resolution, and Manning bottom-friction parameters. Q-values are computed by computing power spectral-densities in 3-hour sliding windows with 67% overlap between 4 and 10 hours after the landslide and observing how power decays in an integrated frequency band of 11.40-11.55 mHz (182). In the caption, "VLP" = "very long-period".*

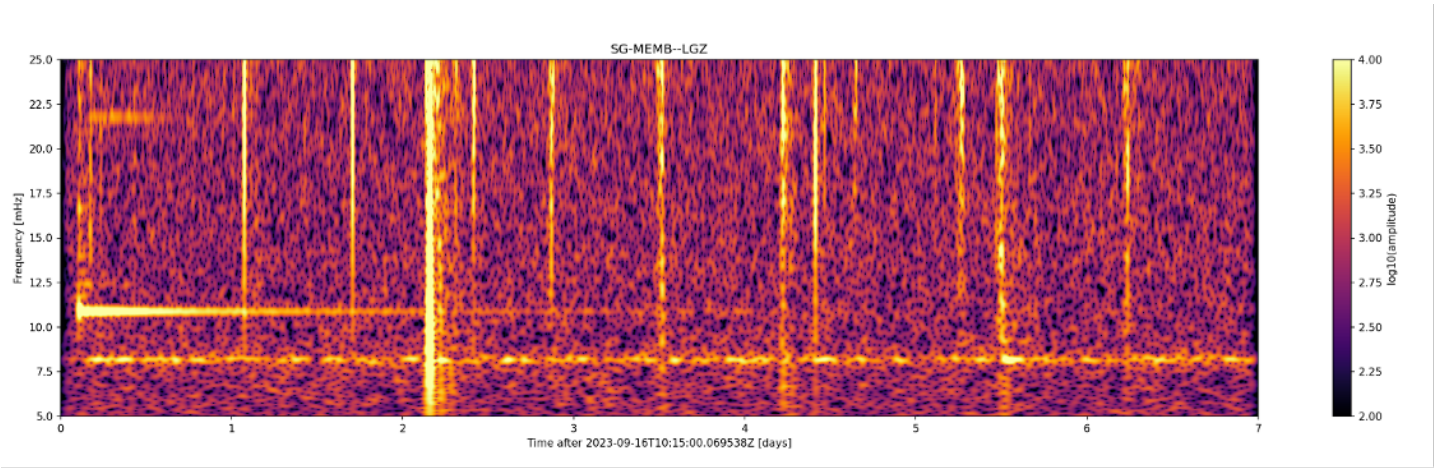

Fig. S6: *Spectrogram showing that the 10.88 mHz very long-period (VLP) event was also recorded by the SG.MEMB superconducting gravimeter installed in Belgium. The prominent signal at 8 mHz is the parasitic resonance of the sphere in the superconducting gravimeter.*

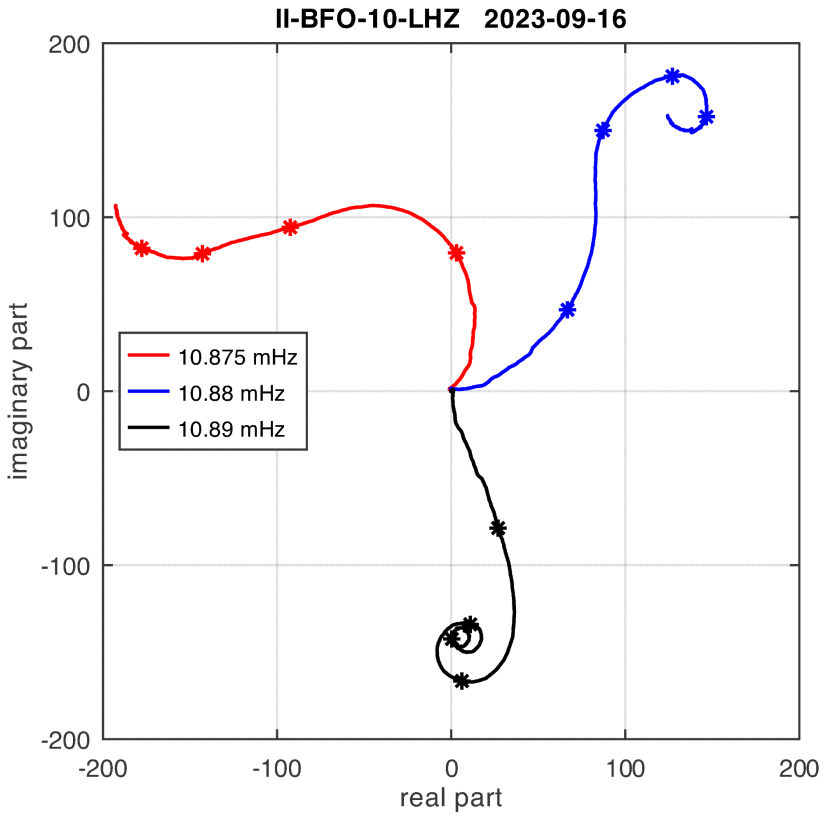

Fig. S7: *Phasor walks for the very long-period (VLP) signal recorded at II.BFO.10.LHZ for the initial 50 hours. A phasor walk is a graphic representation of how the complex Fourier coefficient at a particular frequency grows with the length of the time series. The three phasor walks start at the origin of the complex plane and are marked with an asterisk in 10-hour intervals. The frequencies for the three walks were chosen to cover the band covered by the VLP signal. All three walks are initially curved counterclockwise before they curl in the clockwise direction. This slow change in curvature is indicative of a slow change in the VLP frequency. The angle under which a phasor-walk departs from the origin is arbitrary: changing the start time by only a fraction of the signal period (92 s) any take-off angle can be obtained. The shape of the phasor-walk, however, remains unchanged. The position of the BFO seismic station is shown in Fig. 5A.*

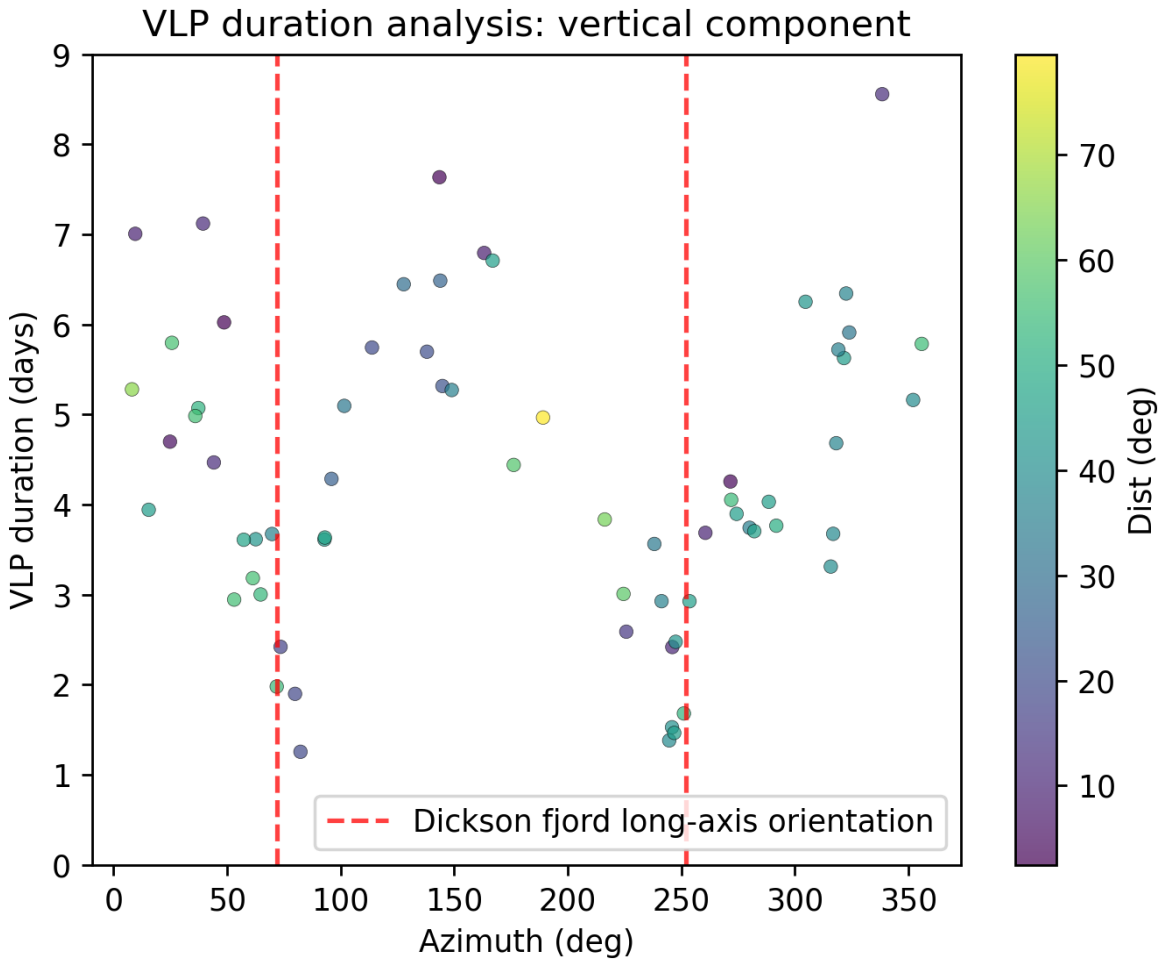

Fig S8: *Vertical-component very long-period (VLP) signal durations estimated from global seismic stations up to 90 degrees distance. The duration pattern relative to the orientation of Dickson Fjord mimics the Love and Rayleigh wave relative amplitudes as shown in Fig. 5A. Durations were conservatively estimated by taking a semi-automated approach in which we first applied a narrowband filter around the fundamental frequency of the VLP, took the envelope of these filtered waveforms, smoothed them, and computed the duration when the envelope amplitude returned to the pre-event root-mean-square noise level. We cross-checked these automated duration calculations with a visual assessment of spectrograms. In the colorbar label, "Dist" = "Distance".*

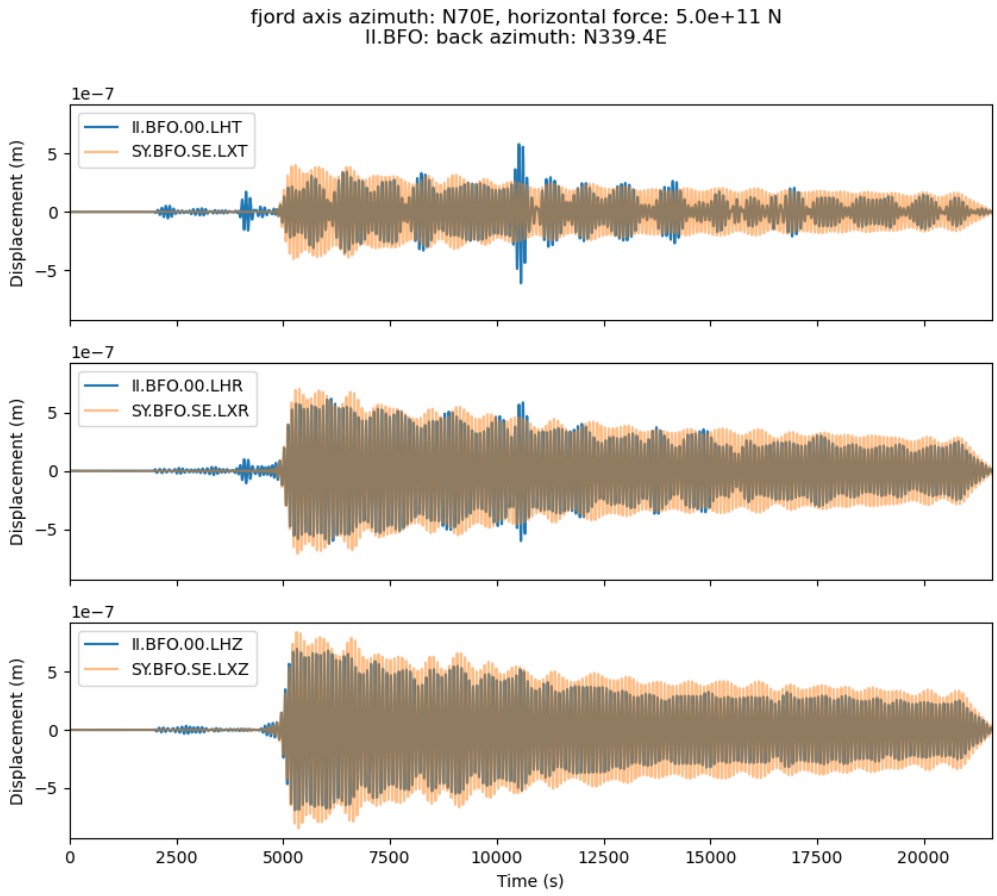

Fig. S9: *Observed (blue) and simulated (orange) ground displacement at station II.BFO, using a horizontal force of 5×10^{11} N and the vertical displacement at DK.SCO as a source time function. Both signals are filtered between 9 and 13 mHz. The position of the BFO seismic station is shown in Fig. 5A.*

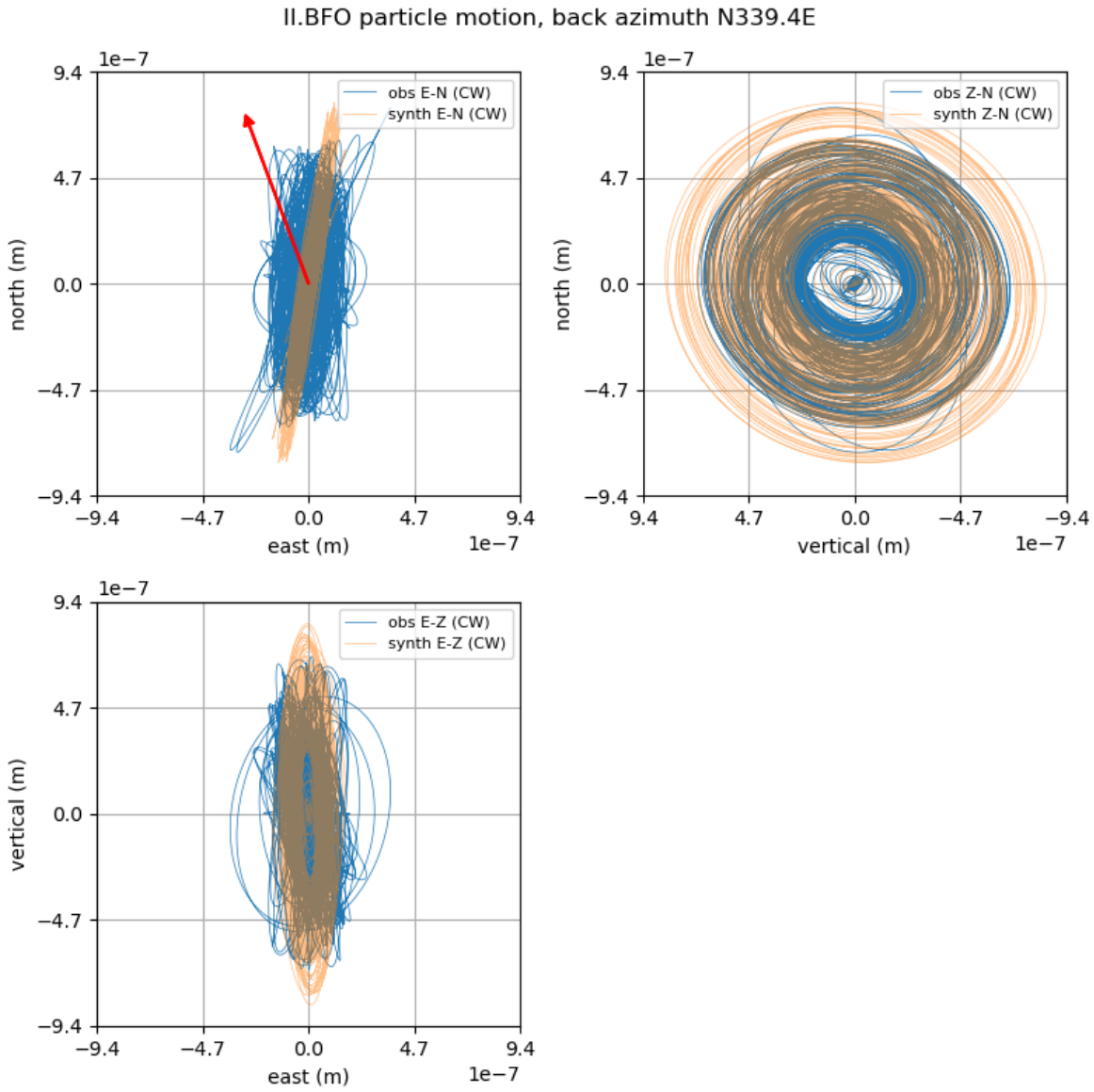

Fig. S10: *Observed (blue) and simulated (orange) particle motion at station II.BFO, using a horizontal force of* 5×10^{11} *N and the vertical displacement at DK.SCO as a source time function. Both signals are filtered between 9 and 13 mHz. The back azimuth to the source is indicated by the red arrow. The position of the BFO seismic station is shown in Fig. 5A.*

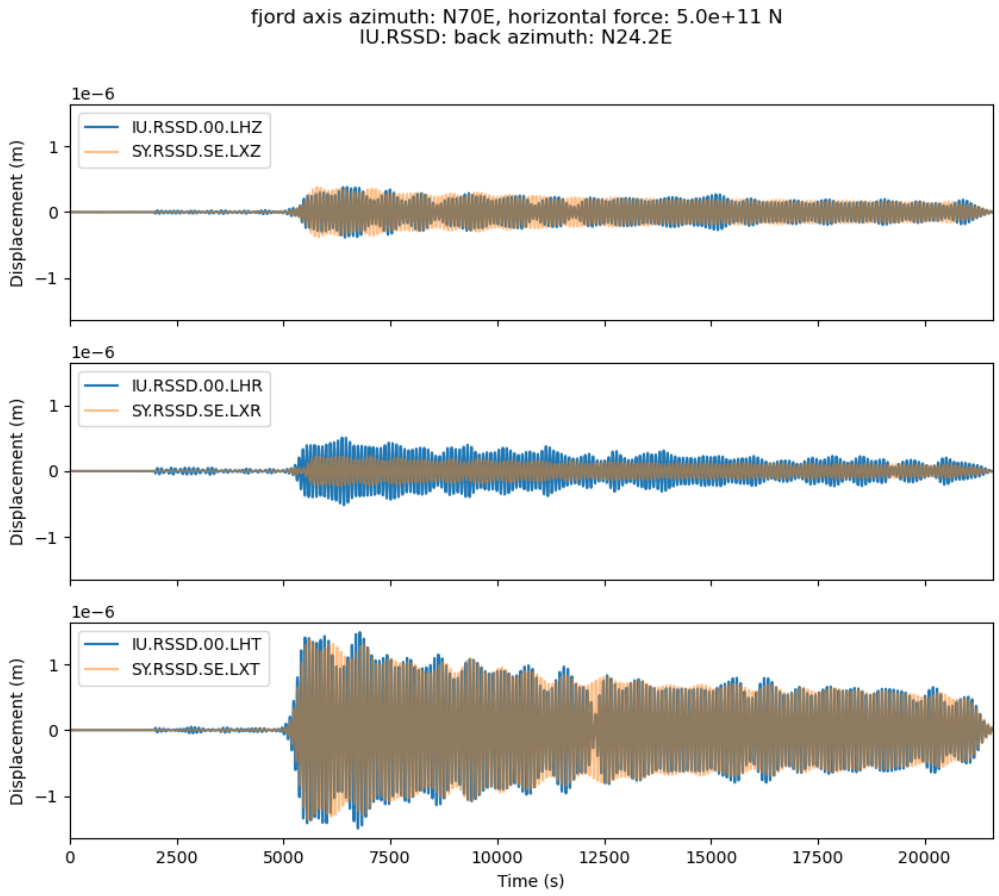

Fig. S11: *Observed (blue) and simulated (orange) ground displacement at station IU.RSSD, using a horizontal force of 5×10^{11} N and the vertical displacement at DK.SCO as a source time function. Both signals are filtered between 9 and 13 mHz. The position of the RSSD seismic station is shown in Fig. 5A.*

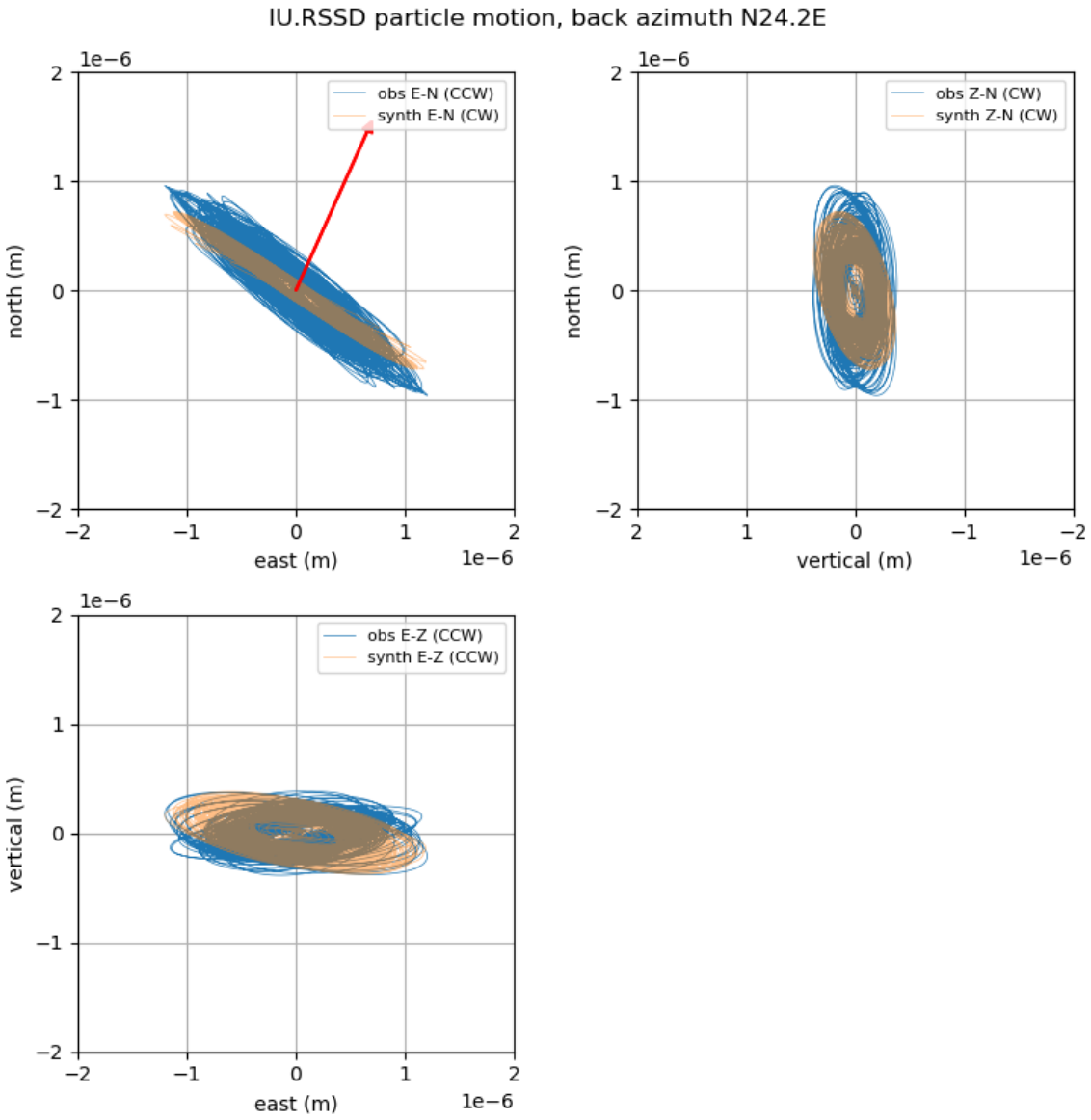

Fig. S12. *Observed (blue) and simulated (orange) particle motion at station IU.RSSD, using a horizontal force of* 5×10^{11} *N and the vertical displacement at DK.SCO as a source time function. Both signals are filtered between 9 and 13 mHz. The back azimuth to the source is indicated by the red arrow. The position of the RSSD seismic station is shown in Fig. 5A.*

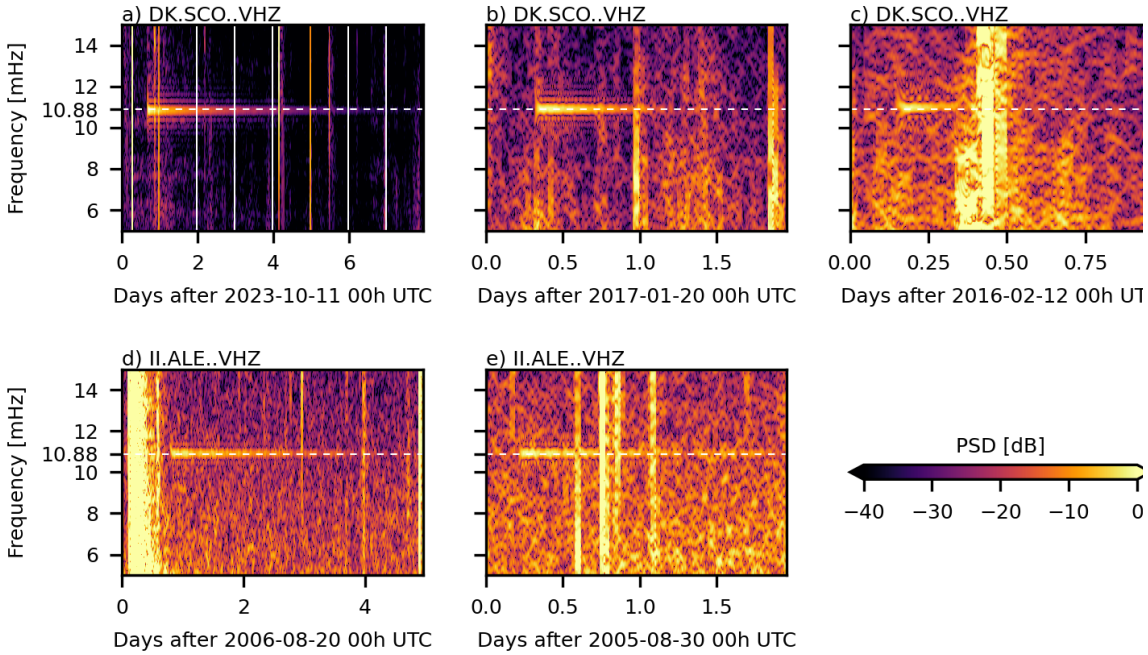

Fig. S13*: Spectrograms of vertical component seismograms of the other detected events with a monochromatic signal near 10.88 mHz (Table S1). (a-c) Events recorded on DK.SCO. (d-e) Events recorded on II.ALE before data were available from DK.SCO. In the caption, "PSD" = "power spectral density".*

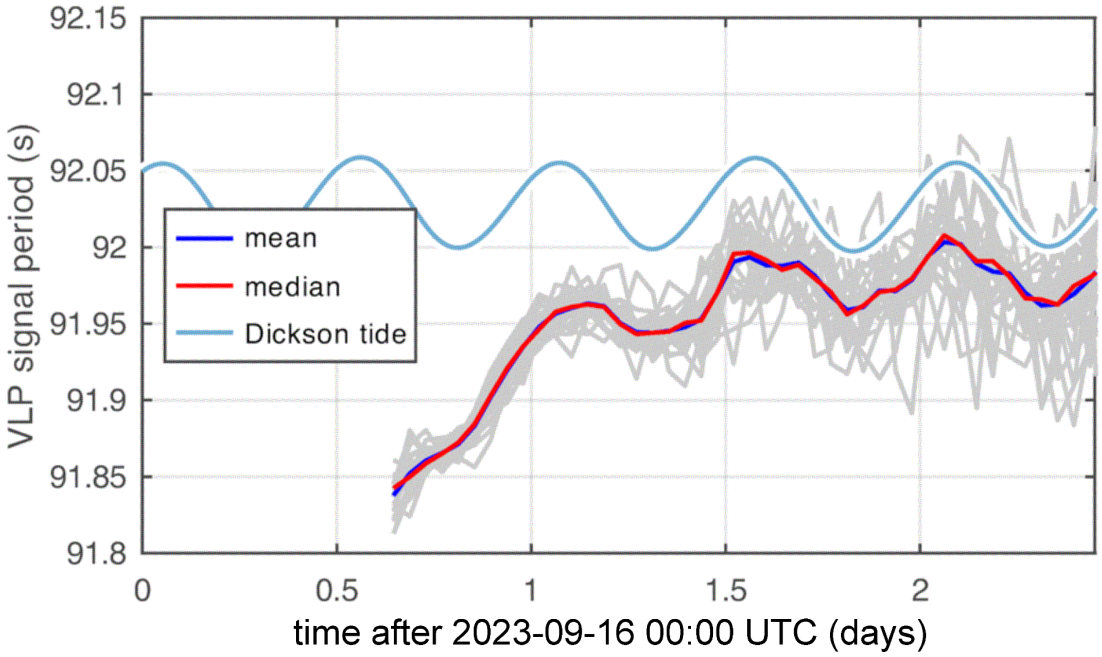

Fig. S14: *Variation of the dominant period of the VLP signal with time. In a sliding window analysis with 5-hour long windows and 4-hour overlap the VLP peak frequency was estimated from Hanning-tapered Fourier spectra. The vertical component data of 45 Global Seismographic Network (GSN) and GEOSCOPE stations were analyzed (gray curves). The blue and red curves show the mean and median variation. The steel blue curve shows the prediction of the ocean tide at Dickson Fjord. For the given time window it has a peak-to-peak amplitude of 1.3 m and is dominated by semidiurnal variations. Both signals, the VLP period and the ocean tide, show a clear semidiurnal component that is in phase such that high ocean tides coincide with the long VLP signal period (i.e., low frequency). The use of a 5-hour long sliding Hanning window to estimate the semidiurnal frequency variation of the VLP signal leads to a bias of 10%. Thus the true semidiurnal VLP frequency variation is 10% larger than shown in this figure.*

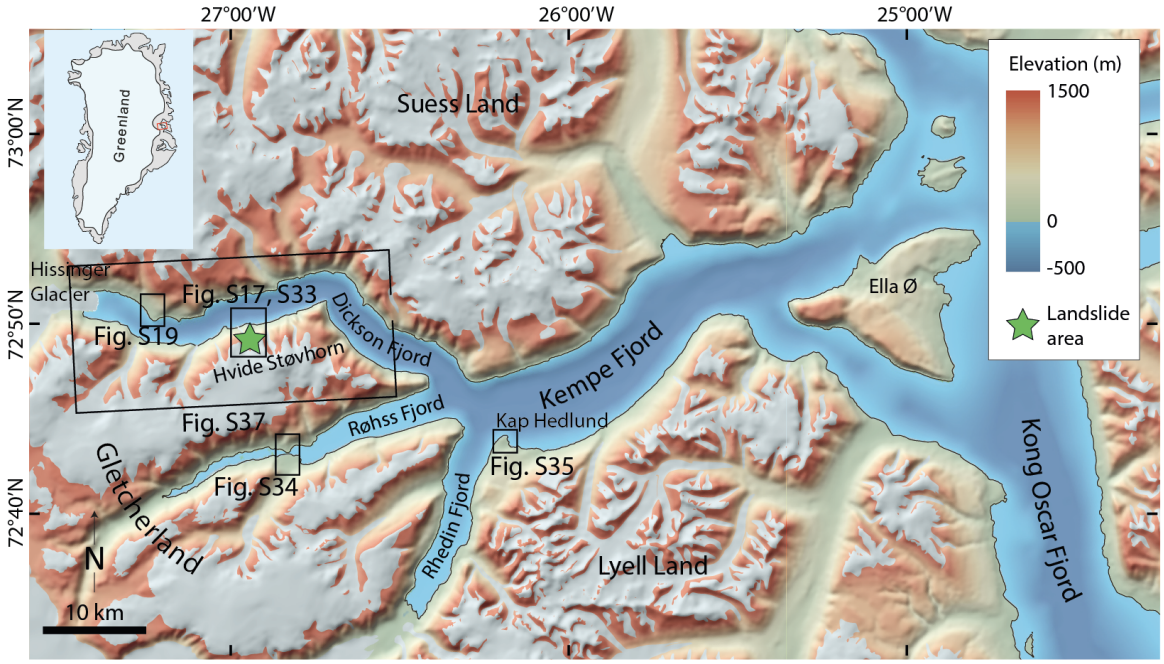

Fig. S15: *Overview map of the field area showing place names used in the text and positions of subsequent figures in the supplementary material. The background DEM is from GEUS and the bathymetry is from BedMachine V5.*

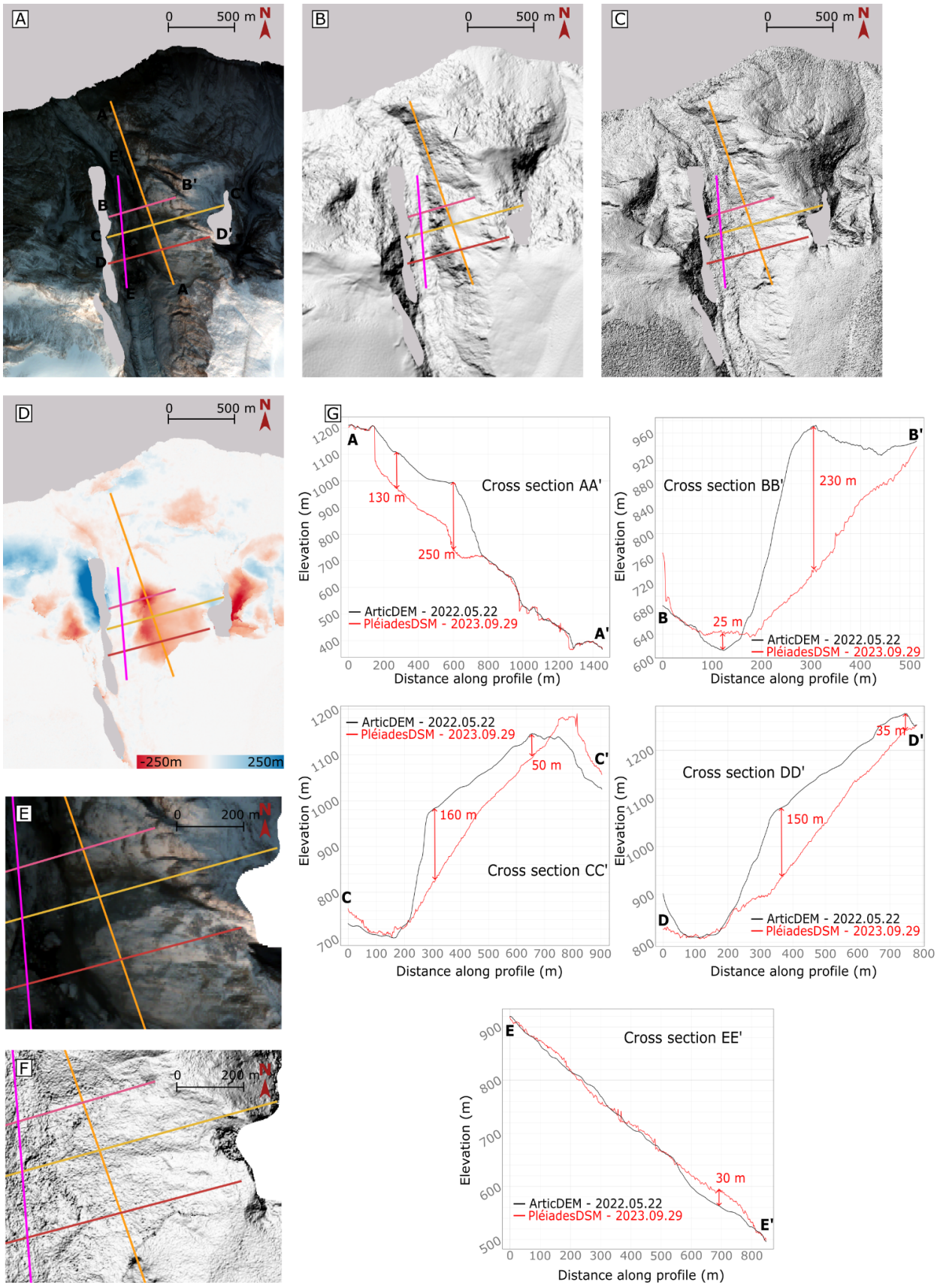
A
0 500 m N
A'
E'
B'
C'
B
C
D'
D
E
A
B
0 500 m N
C
0 500 m N
D
0 500 m N
-250m
250m
E
0 200 m N
F
0 200 m N
G
A
130 m
250 m
Cross section AA'
A'
— ArticDEM - 2022.05.22
— PléiadesDSM - 2023.09.29
Elevation (m)
Distance along profile (m)
B'
230 m
Cross section BB'
B
25 m
— ArticDEM - 2022.05.22
— PléiadesDSM - 2023.09.29
Elevation (m)
Distance along profile (m)
— ArticDEM - 2022.05.22
— PléiadesDSM - 2023.09.29
C'
50 m
160 m
Cross section CC'
C
Elevation (m)
Distance along profile (m)
35 m
D'
Cross section DD'
150 m
D
— ArticDEM - 2022.05.22
— PléiadesDSM - 2023.09.29
Elevation (m)
Distance along profile (m)
E
Cross section EE'
30 m
E'
— ArticDEM - 2022.05.22
— PléiadesDSM - 2023.09.29
Elevation (m)
Distance along profile (m)

Fig. S16: *Rockslide volume estimation from a post-event DSM constructed from Pleiades satellite stereo-imagery tasked by the CIEST2 programme (ForM@Ter and CNES) and acquired on 2023-09-29. (a) Pléiades multispectral image, centered on the rockslide of 2023-09-29. The water surfaces in the fjord and the shadows are masked in light gray (© CNES 2023, Distribution Airbus Defence & Space); (b) Hillshade of the 2m spatial resolution pre-event topography (ArcticDEM, 2022-05-22); (c) Hillshade of the 1m spatial resolution post-event topography (Pléiades DSM, 2023-09-29); (d) DSM of difference (DoD) calculated from the subtraction of the post-event and pre-event topographies; (e) Zoomed view of the rockslide source area as identified in the 2023-09-29 Pléiades multispectral imagery; (f) Zoomed view of rockslide source area in the hillshade post-event topography; (g) Longitudinal and transverse cross-sections presenting the pre- and the post-event topographies.*

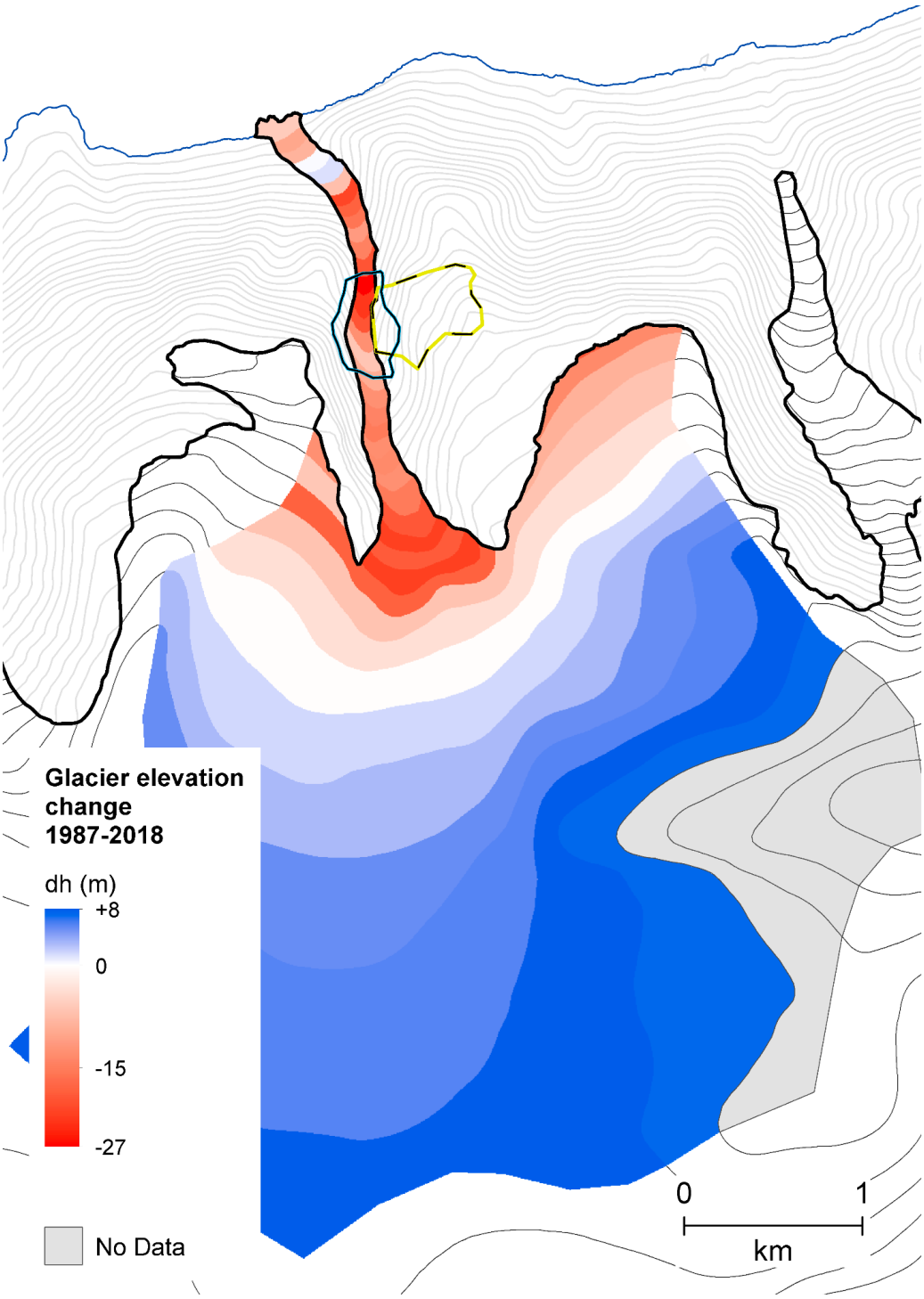

***Fig. S17**: Hypsometrically binned surface elevation change during 1987-2018 of the drainage basin of glacier GLIMS ID: G333056E72786N. The yellow/black line is the outline of the area that failed in the landslide, and the blue outline is the impact area where the rockslide impacted the glacier.*

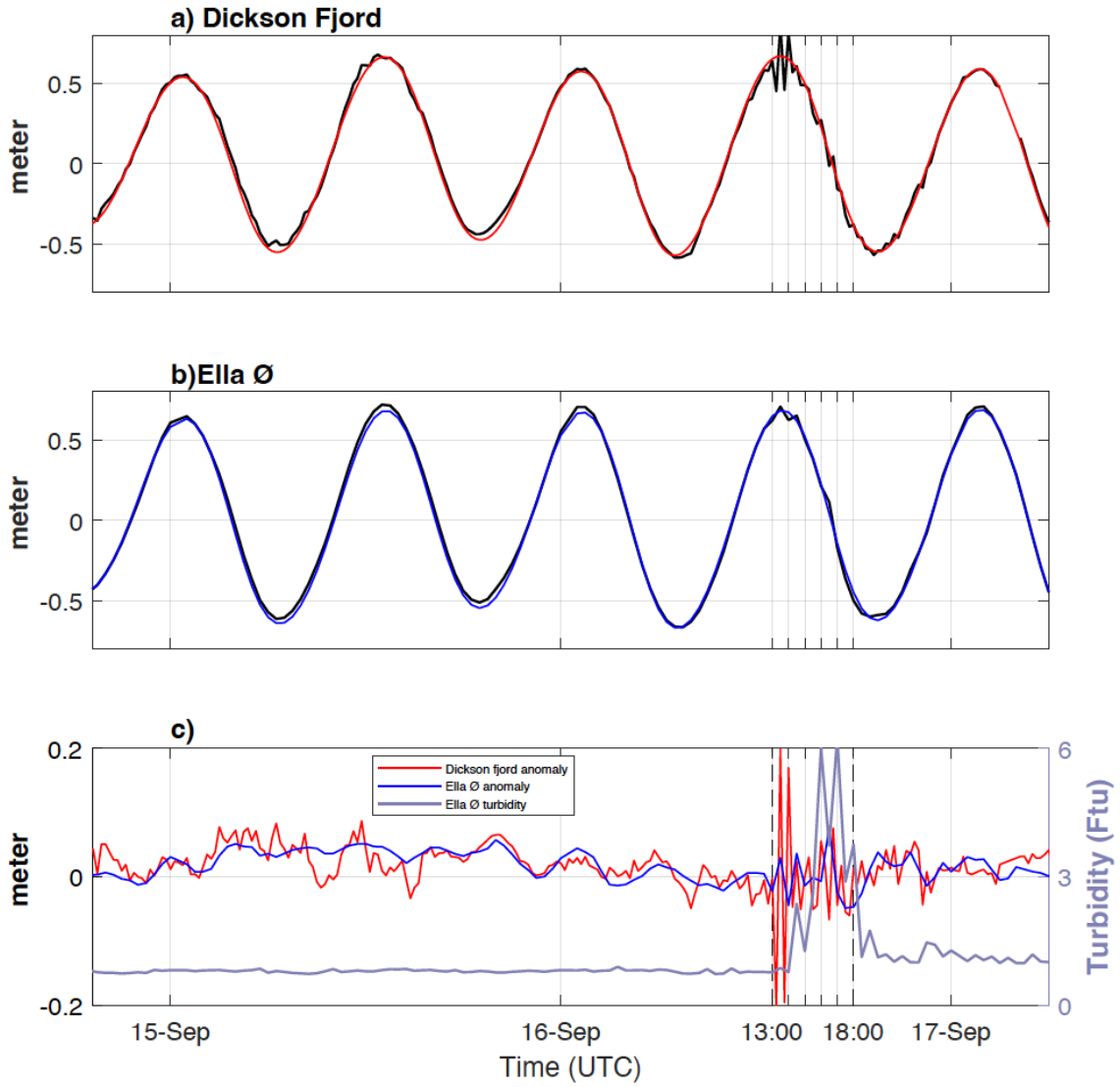

Fig. S18: *Tidal signal from (a) Dickson and (b) Ella Ø moorings. Data are sampled every 15 minutes at Dickson Fjord, and every 30 minutes at Ella Ø. The black line is observations, and blue and red are the predicted tide. (c) Tidal anomaly as well as the turbidity signal following the arrival of the tsunami.*

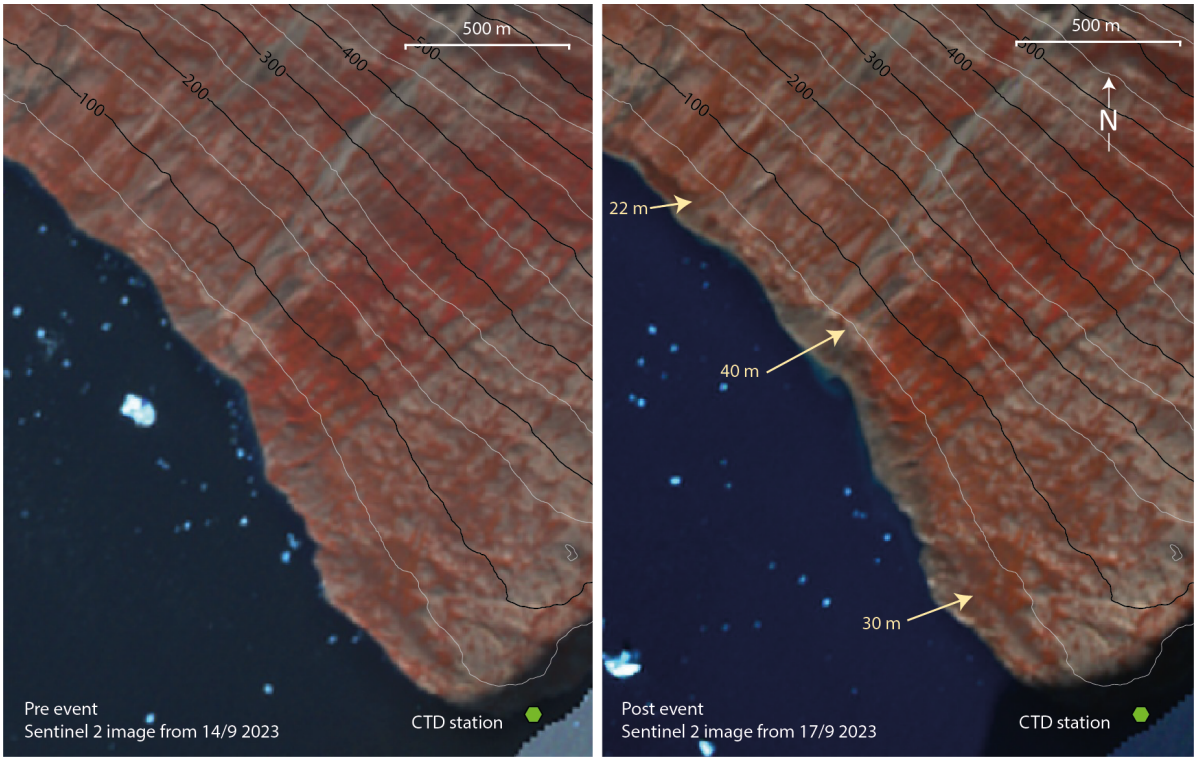

Fig. S19: *Examples of observed runup in Dickson Fjord shown on false color Sentinel 2 satellite images. 9 km west of the landslide. The runup is seen as darker areas in the post-event image relative to the pre-event image. Some measured heights in m above sea level are shown with yellow arrows. Contour intervals are 50 m. Refer to Fig. 1C for the position of the conductivity, temperature, depth (CTD) station in the fjord.*

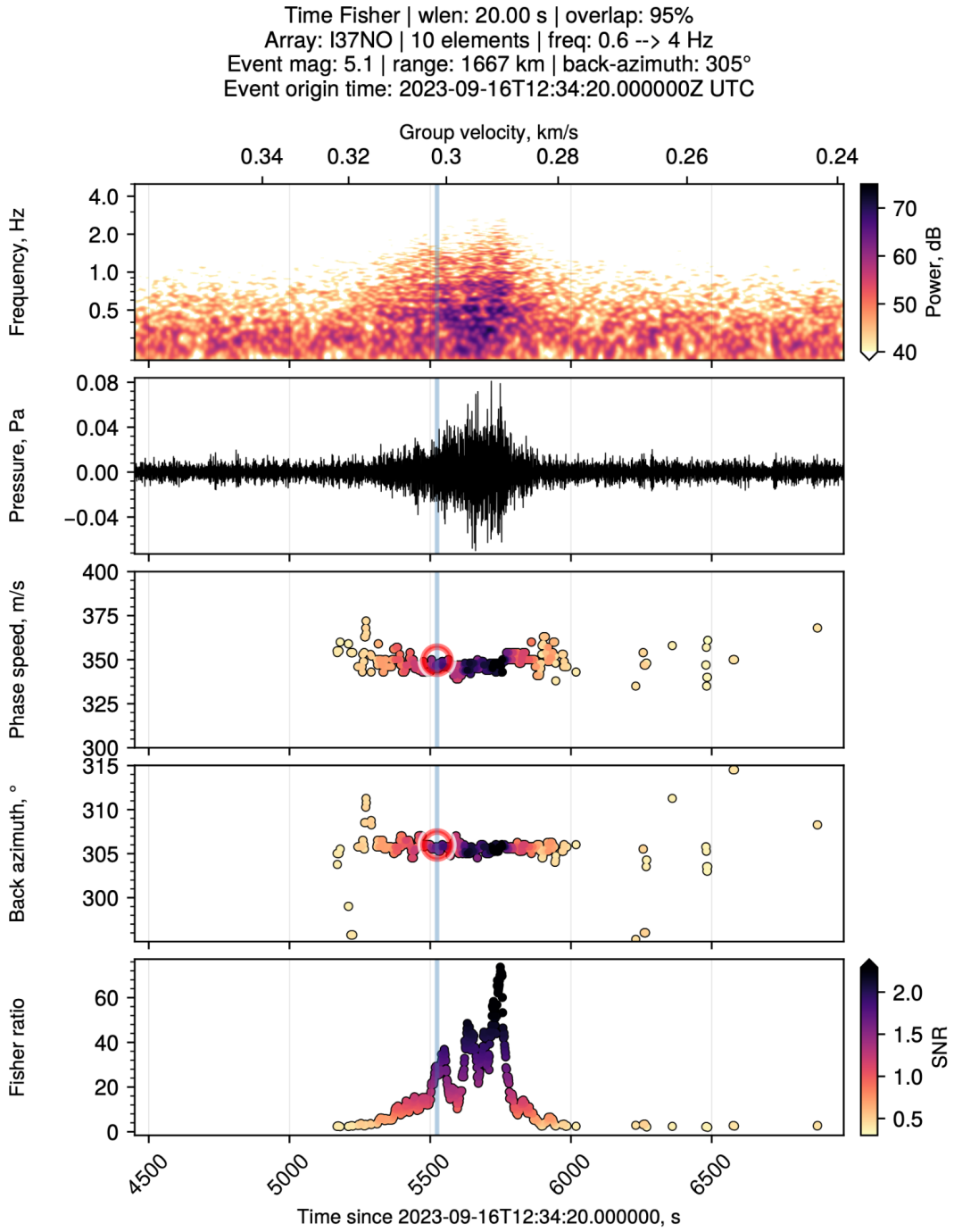

Fig. S20*: Infrasound array processing results at I37NO (Bardufoss, Norway). Ray-theoretical simulations of travel time (blue bar), phase speed, and back azimuth (both indicated by red circles) are indicated and show good agreement with the observed values. In the colorbar label, "SNR" = "signal-to-noise ratio".*

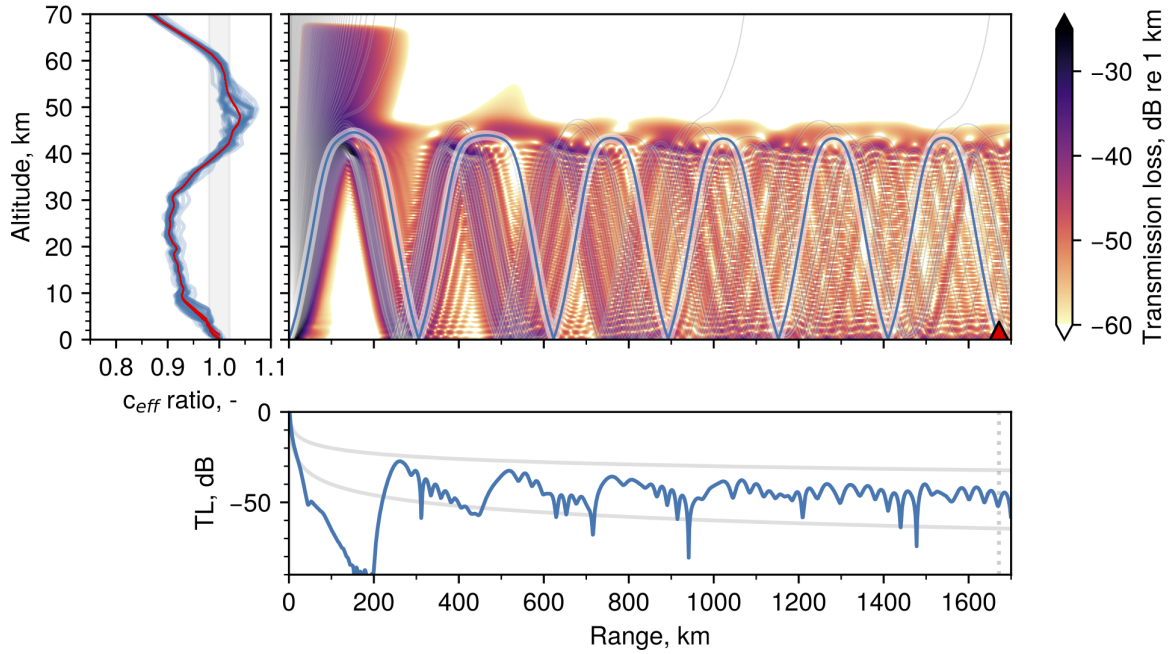

Fig. S21*: Infrasound propagation modeling results from the landslide location towards infrasound array I37NO (red triangle) using the parabolic equation (PE) and ray theoretical models. The PE is used to simulate the transmission loss (TL) from the source at 0.5 Hz. The eigenray, connecting the source to the receiver, is shown in blue and is used to simulate arrival time, back-azimuth, and phase speed at I37NO (as shown in Fig. S20). The simulations are calculated using a 1-D model atmosphere (red line) retrieved from the European Centre for Medium-Range Weather Forecasts (ECMWF) operational forecast for 2023-09-16T13:00:00 UTC. The effective sound speed ratio (c_{eff} ratio) corresponds to the effective refractive index for sound propagation in the atmosphere.*

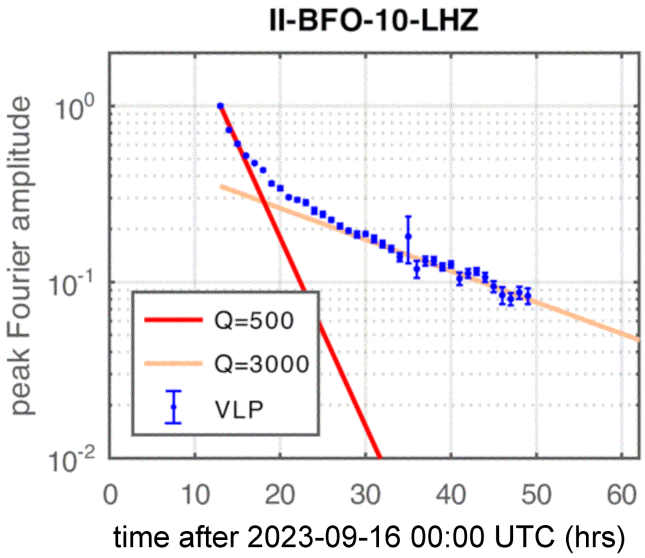

Fig. S22: *Amplitude decay of the very long-period (VLP) signal from 16 September 2023 based on a sliding window spectral analysis. The amplitude of the VLP signal was estimated as the peak amplitude in spectra of Hanning tapered 1-hour-long data segments. The signal-to-noise ratio (SNR) for the VLP signal was estimated from the spectra as the ratio of the VLP peak amplitude over the root-mean-square (RMS) noise in frequency bands adjacent to the VLP peak. The amplitude errors shown are then taken as the peak amplitude over the SNR. An initial rapid decay with the quality factor of a harmonic oscillator, Q ~ 500 is followed after about 10 hours by a 10-times slower decay with Q ~ 3000. Note that the SNR 35 hours after the VLP onset is still 6:1 so we can rule out that the apparent slow VLP decay at later times is caused by bias due to low SNR. The position of the BFO seismic station is shown in Fig. 5A.*

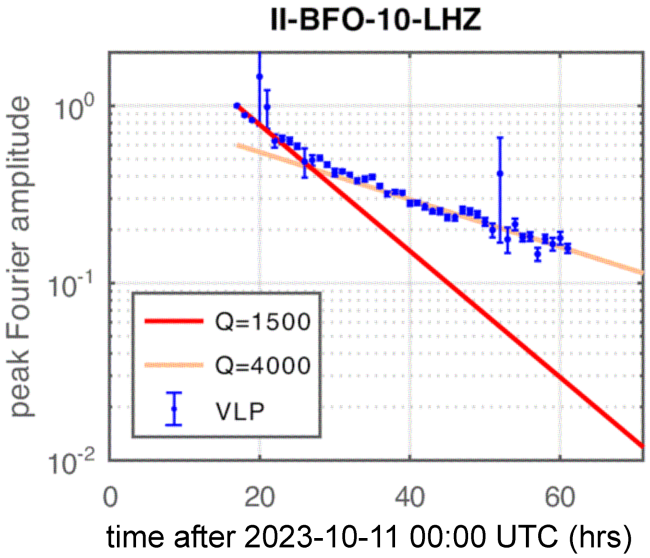

Fig. S23: *Same as Fig. S22 but for the very long-period (VLP) event of 11 October 2023. Interference from simultaneous earthquakes produced the amplitude estimates with large error bars. For this event too, a transition from fast to slow signal decay is evident. The position of the BFO seismic station is shown in Fig. 5A.*

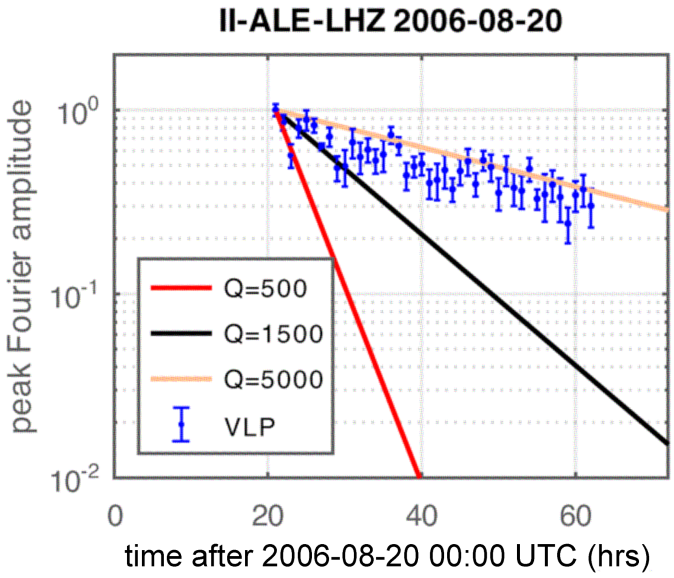

Fig. S24: *Same as Fig. S22 but for the very long-period (VLP) event of 20 August 2006 observed at II.ALE. This event is more than 10 times smaller than the two events from 2023 and signal decay is slow right from the start. The position of the ALE seismic station is shown in Fig. 5A.*

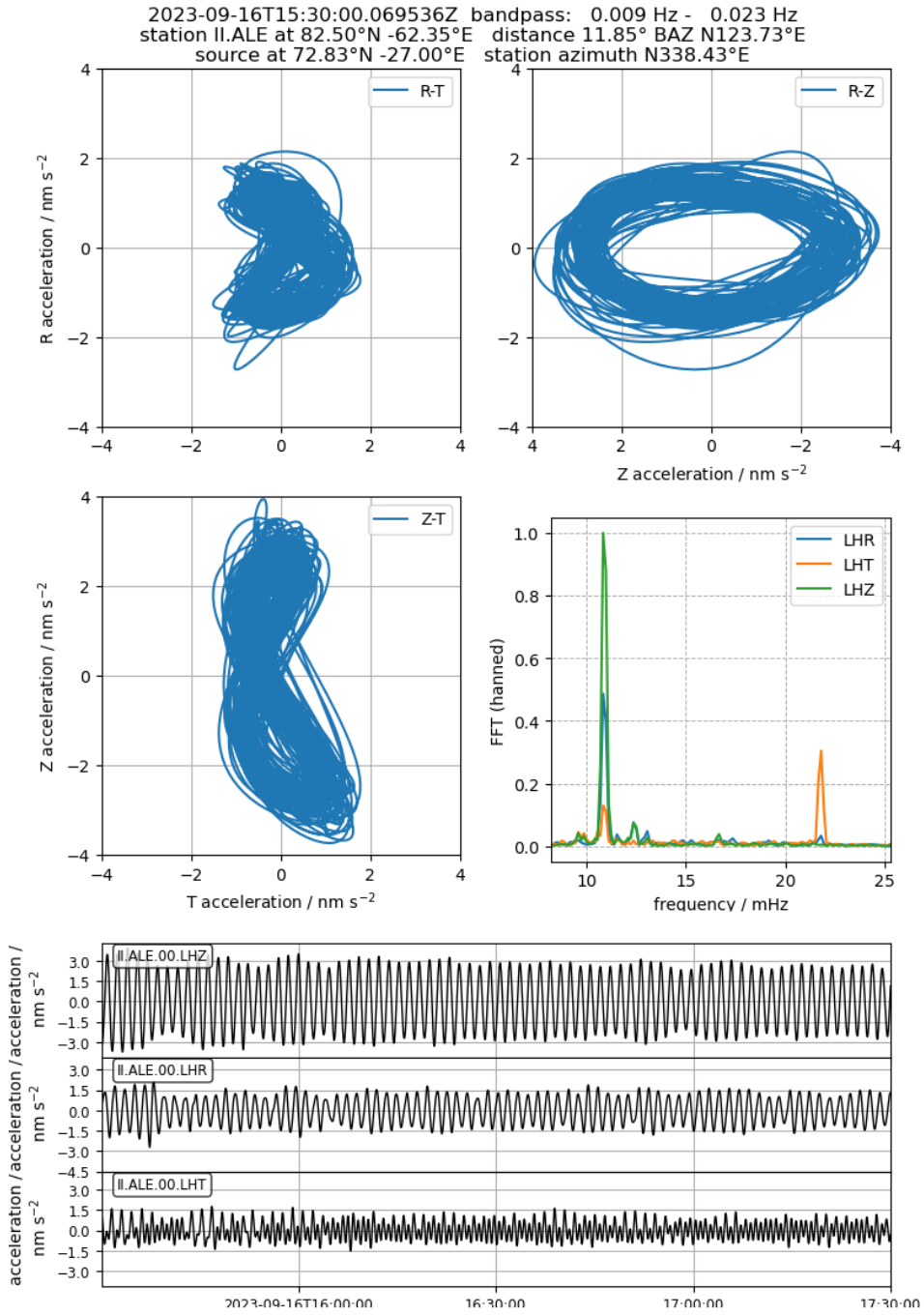

Fig. S25: Polarization analysis of signals recorded at station II.ALE, Canada (Fig. 5A). R-T = radial-transverse; R-Z = radial-vertical; Z-T = vertical-transverse; LHR = radial component; LHT = transverse component; LHZ = vertivcal component.

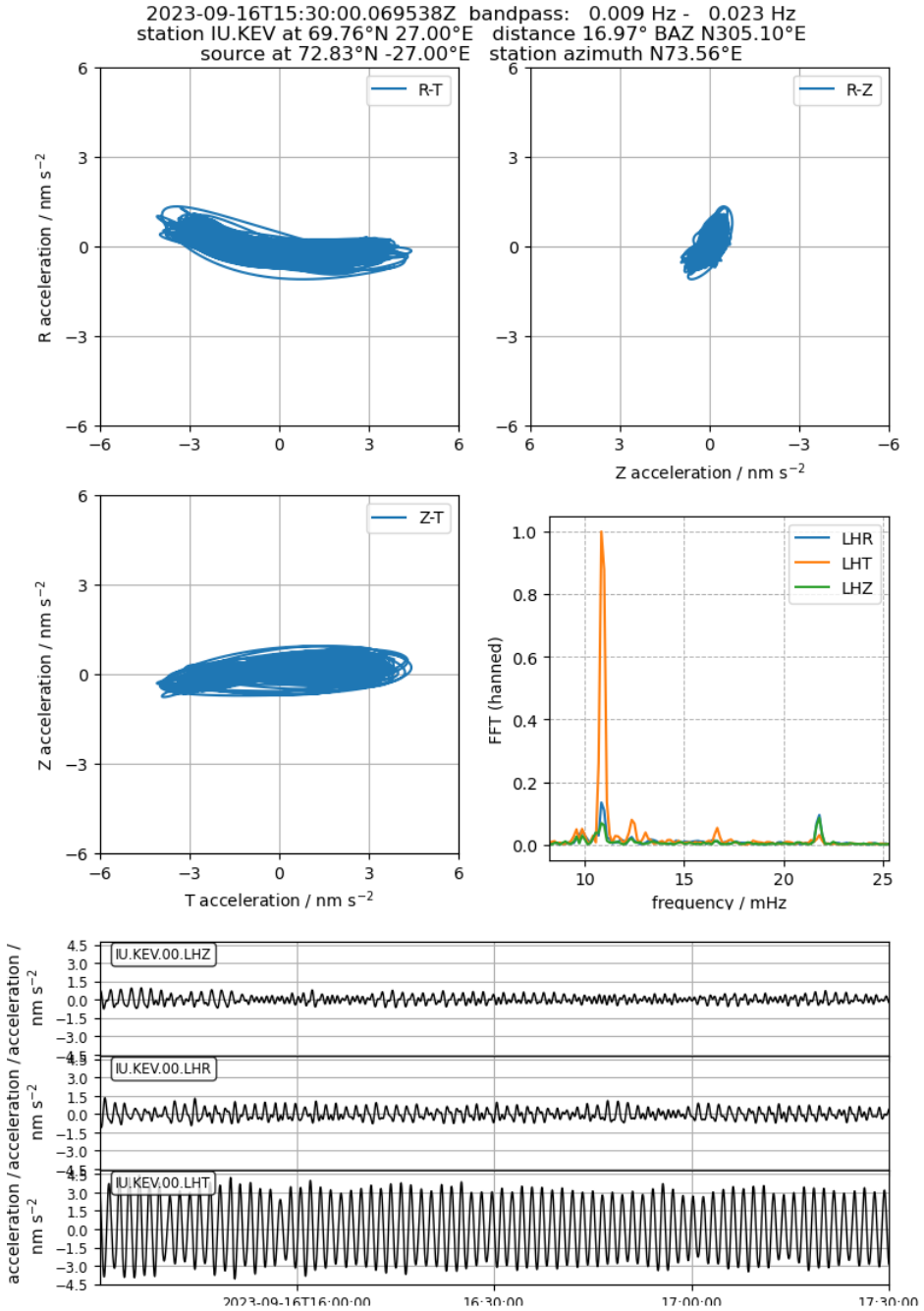

Fig. S26*: Polarization analysis of signals recorded at station IU.KEV, Finland (Fig. 5A).* R-T = radial-transverse; R-Z = radial-vertical; Z-T = vertical-transverse; LHR = radial component; LHT = transverse component; LHZ = vertivcal component.

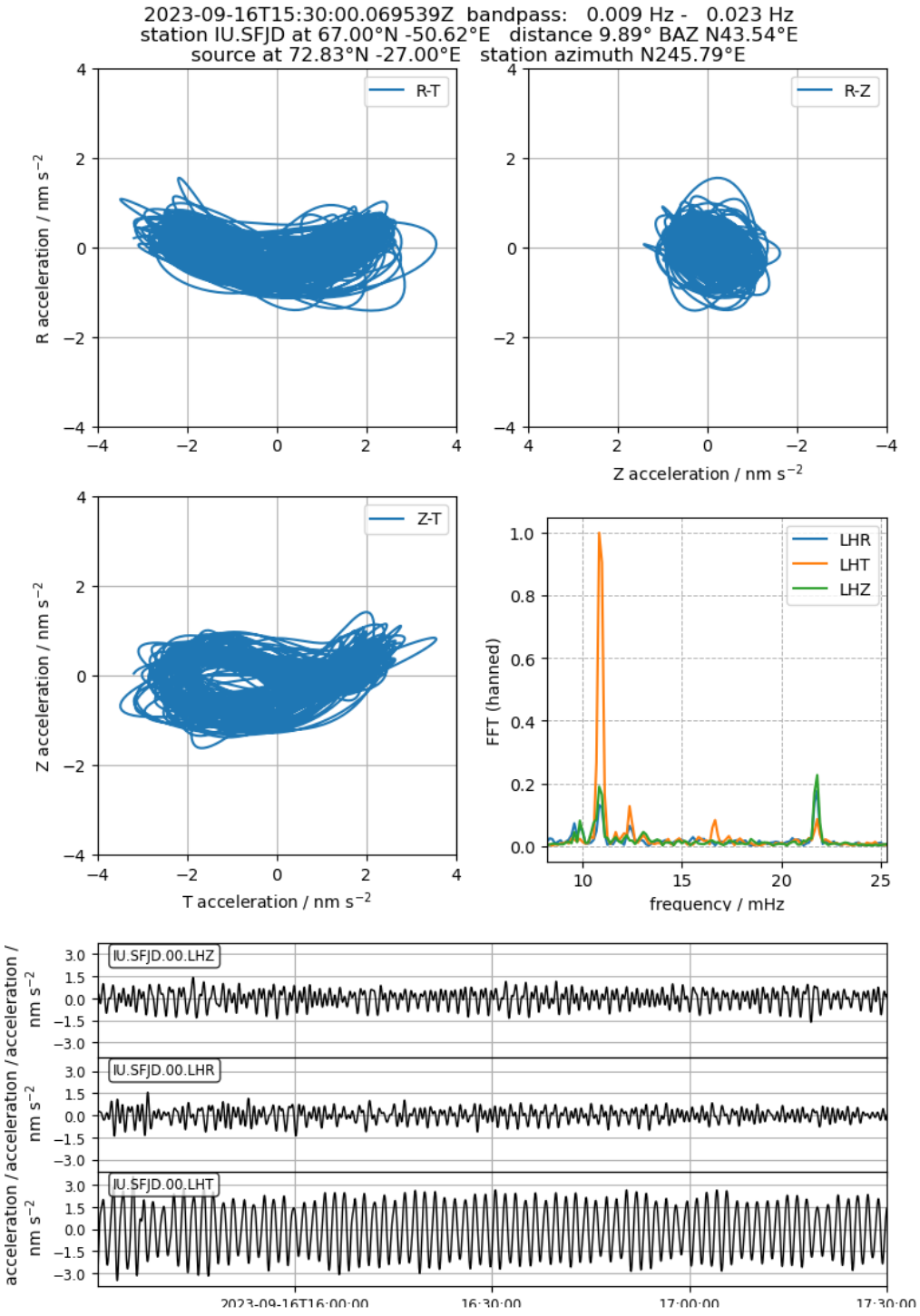

Fig. S27: Polarization analysis of signals recorded at station IU.SFJD, Greenland (Fig. 5A). R-T = radial-transverse; R-Z = radial-vertical; Z-T = vertical-transverse; LHR = radial component; LHT = transverse component; LHZ = vertical component.

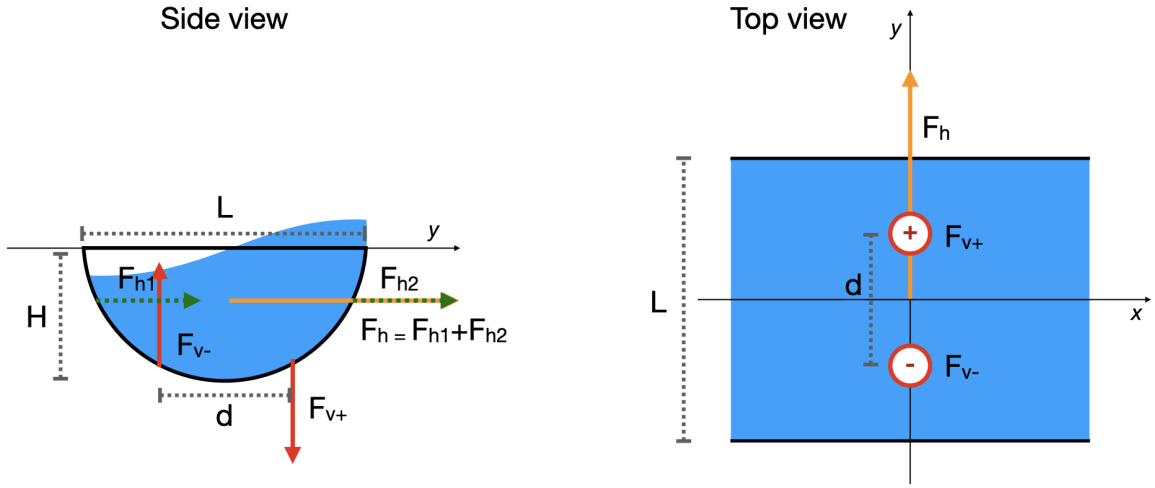

***Fig. S28**: Simplified fjord geometry with the system of forces that are generated by a seiche. Water oscillates in the y-axis direction, while the main fjord axis is in the x-axis direction.*

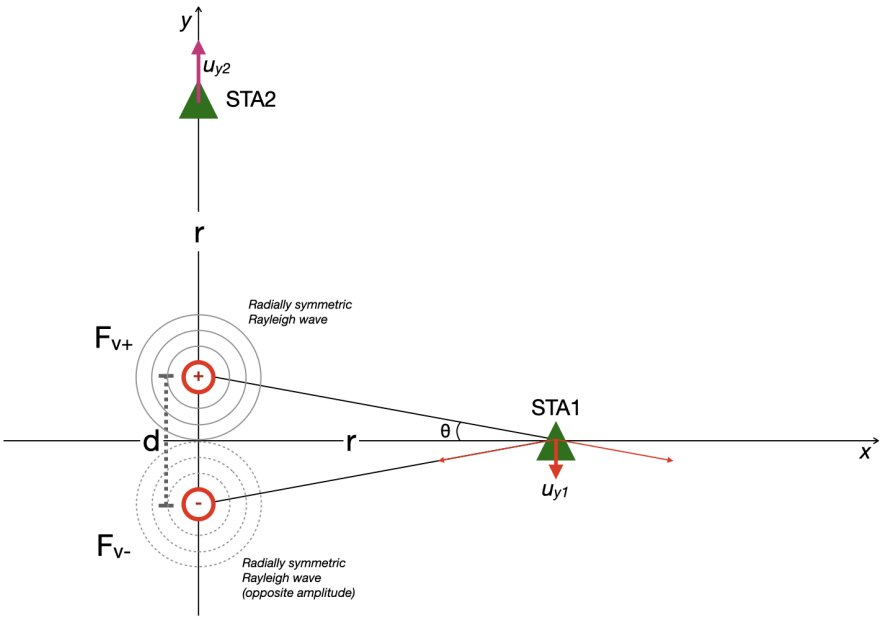

***Fig. S29**: Rayleigh wave radiation associated with the two vertical forces that is recorded at two stations. The distance r is defined, for both stations, from the center of the axis system.*

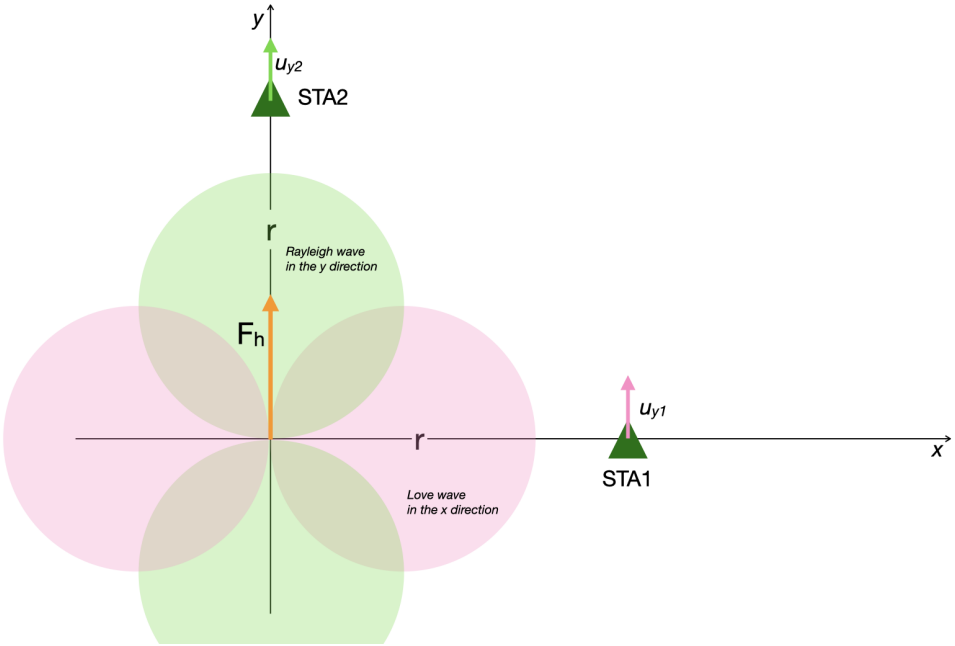

Fig. S30: *Surface wave radiation associated with the effective horizontal force and recorded at two stations. The colored circles are a schematic representation of radiation patterns for Love (pink) and Rayleigh (green) surface waves. The distance r is defined, for both stations, from the center of the axis system.*

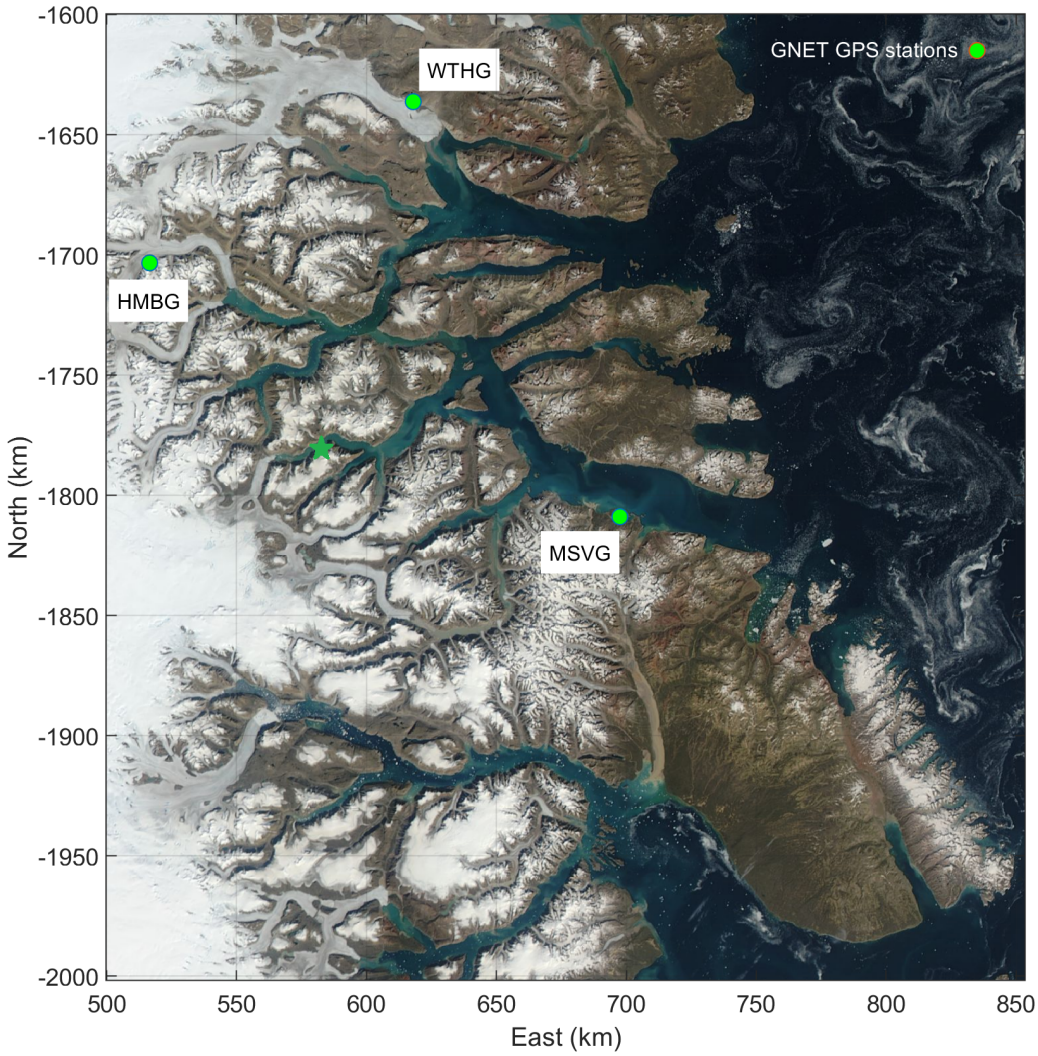

Fig. S31: *Location of GNET GPS (Global Positioning System) stations in East Greenland. The green star is the position of the landslide in Dickson Fjord.*

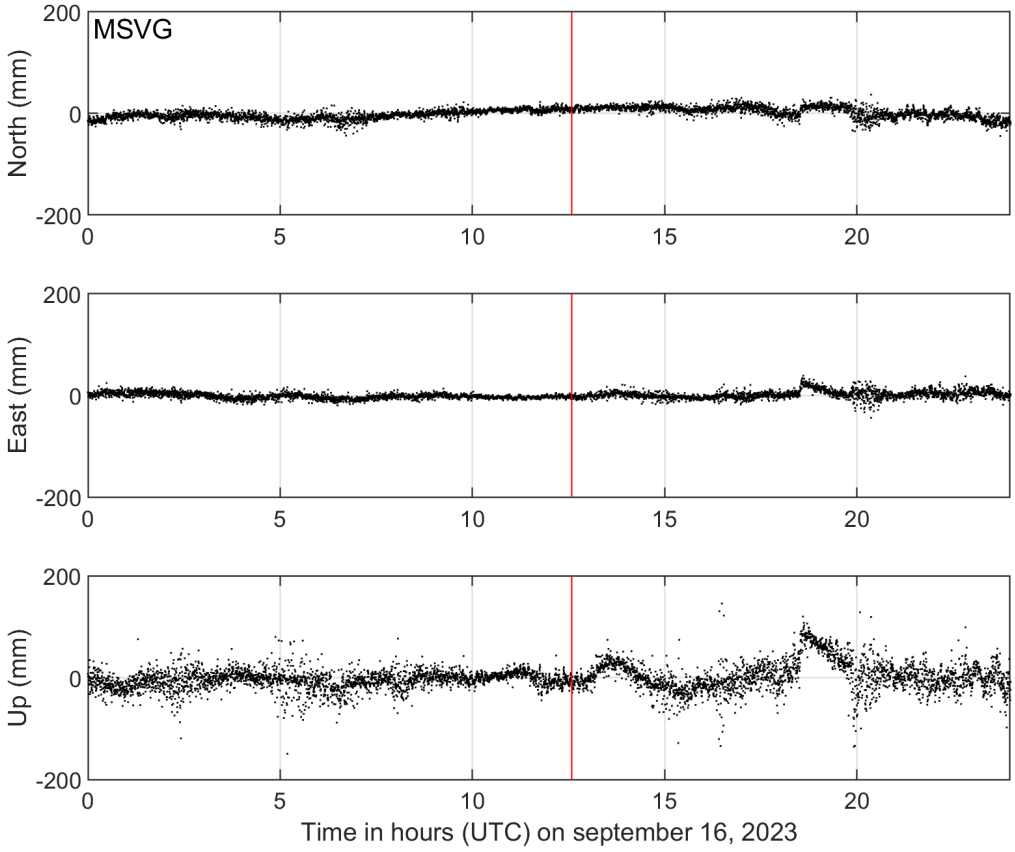

Fig. S32: *GPS (Global Positioning System) time series of north, east, and up displacements at MSVG. The timing of the landslide is indicated with a red line.*

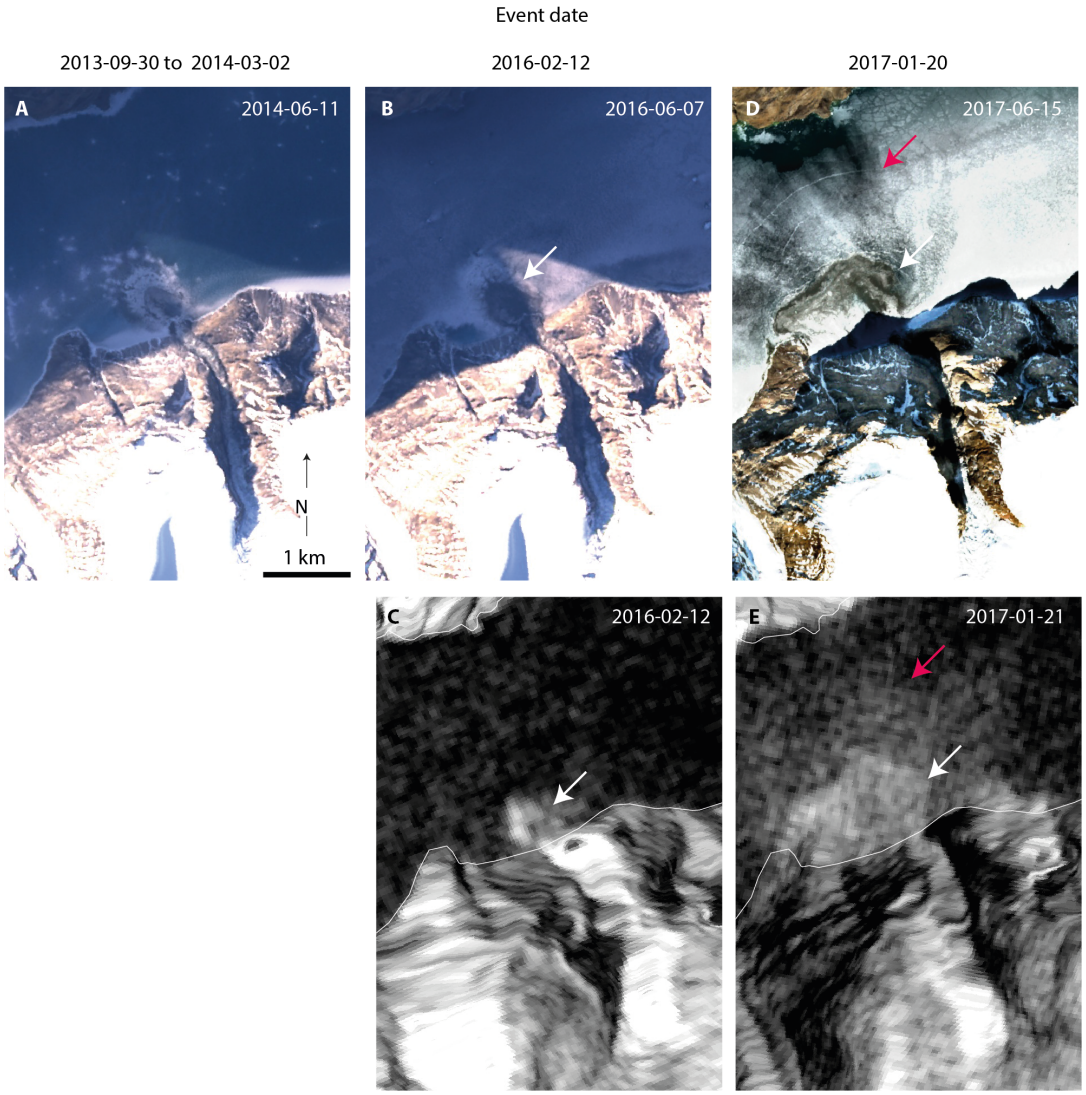

Fig. S33: *Satellite images of precursory landslide events at the glacial gully below Hvide Støvhorn.* ***(A)*** *Pan-sharpened Landsat 8-9 image (2014-06-11) of the landslide that must have failed between 2013-09-30 and 2014-03-02.* ***(B)*** *Pan sharpened Landsat 8-9 image (2016-06-07) of the 2016-02-12 04:10 UTC landslide.* ***(C)*** *Orthorectified gamma0 Sentinel-1 SAR image from the day of the landslide (2016-02-12). The high reflectance landslide deposit is given by a white arrow and has the same position as the white arrow in B).* ***(D)*** *Sentinel-2 image (2017-06-15) of the 2017-01-20 08:10 UTC landslide. Note the fractured ice and the dark halo with the absence of snow distal to the landslide deposit.* ***(E)*** *Same as (B) but from the day after the landslide (2017-01-20). The high reflectance landslide deposit is indicated with a white arrow and the slightly lower reflectance halo distal to the deposit with a red arrow. The position of the arrows is the same as in D).*

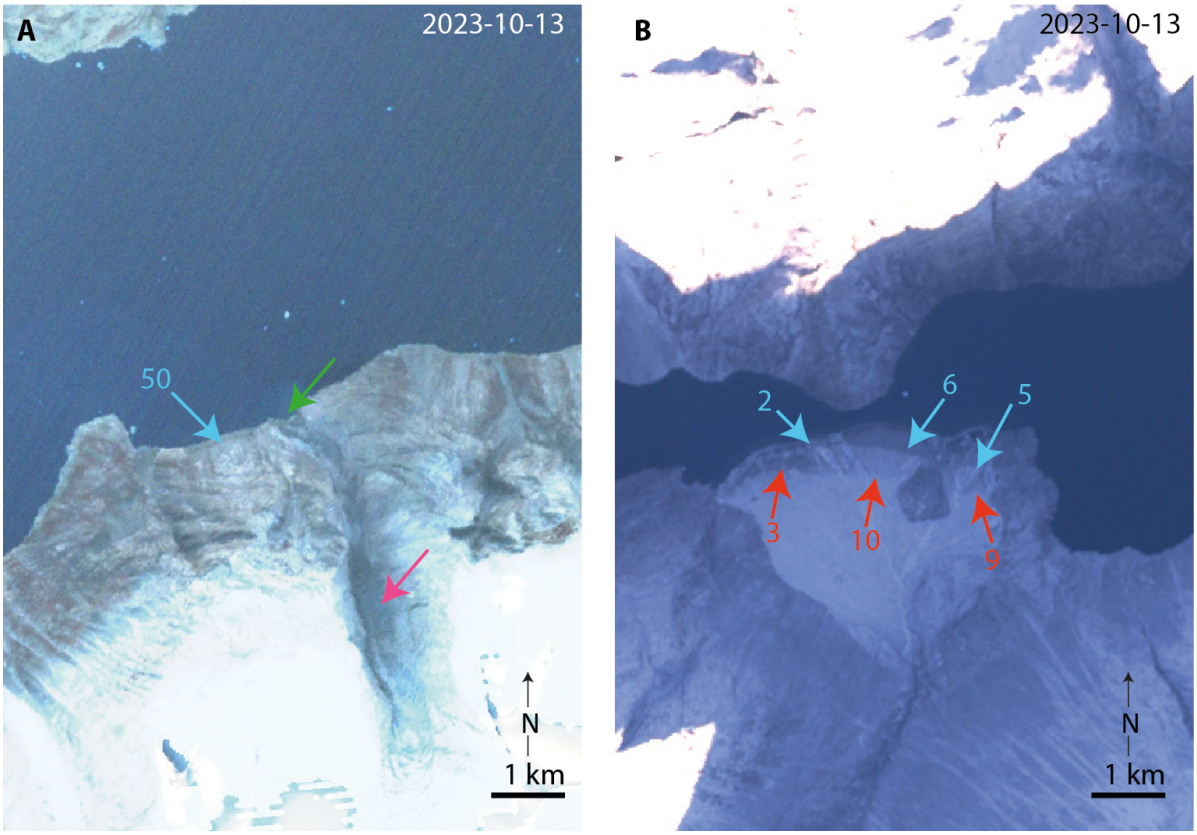

***Fig. S34**: Satellite observations of the 2023-10-11 landslide and tsunami. **(A)** Sentinel-2 image from 2023-10-13 of the glacier. A runup of 50 m is mappable (blue arrow). The 2023-09-16 event had a runup of ~80 m here. The green arrow indicates where the peninsula has been destroyed during the event, and further depletion of the glacier is visible above this area. The red arrow indicates the assumed source area of this event as the glacier is debris-covered here. **(B)** A delta in Røhss Fjord 40 km from the landslide showing inundation from the 2023-09-16 and the 2023-10-11 tsunamis. Vertical runups for the two tsunamis are indicated with red numbers for the 2023-09-16 event and blue for the 2023-10-11.*

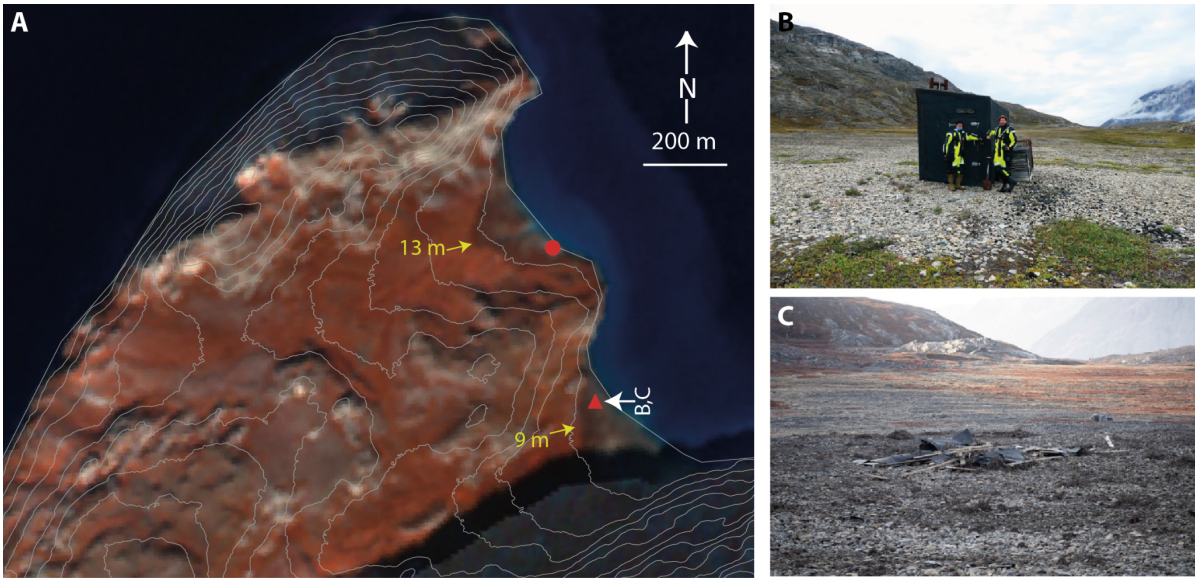

Fig. S35: *Examples of cultural heritage destroyed by the tsunami.* ***(A)*** *False-color Sentinel 2 satellite image from 2023-09-17 showing Kap Hedlund 33 km from the rock-ice avalanche. Tsunami runup is seen as dark colored areas and the maximum vertical runup is indicated with yellow arrows and annotated. 10 m contours are shown. The position of the Kap Hedelund hut from 1964 is shown (red triangle) along with the position of a Thule Culture Inuit site (red circle). Both are well within the inundated area.* ***(B)*** *and* ***(C)*** *photographs of the Kap Hedlund hut before (2022-08-09) and after (2023-09-19) the tsunami. Photo in (C) taken by the Sirius dog sled patrol of the Joint Arctic Command.*

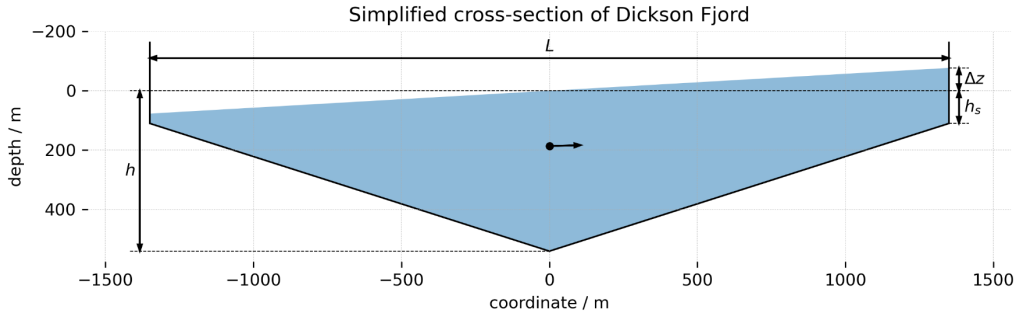

Fig. S36: *Simplified cross section through Dickson Fjord (note the vertical exaggeration on the seiche height (Δz) and the height of the vertical fjord walls). The dimensions are defined by the width L = 2700 m and the maximum depth h=540 m. At the shore, the simplified fjord is confined by vertical walls, which extend to h_s below the water surface. These walls simplify the computation of the location of the center of mass when the water surface gets deflected. In our computation, h_s = 20 m. The black dot marks the center of mass when the water surface is in equilibrium. The arrow shows the displaced center of gravity for the vertical displacement of Δz for the water surface at the shore.*

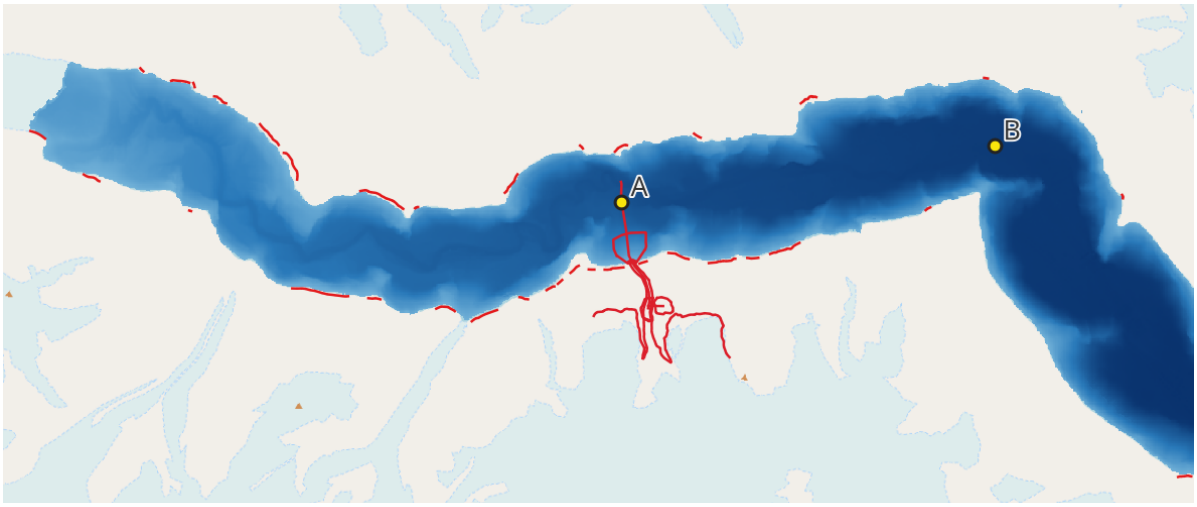

Fig. S37: *Computational domain and location of the gauges A and B in the GloBouss model.*

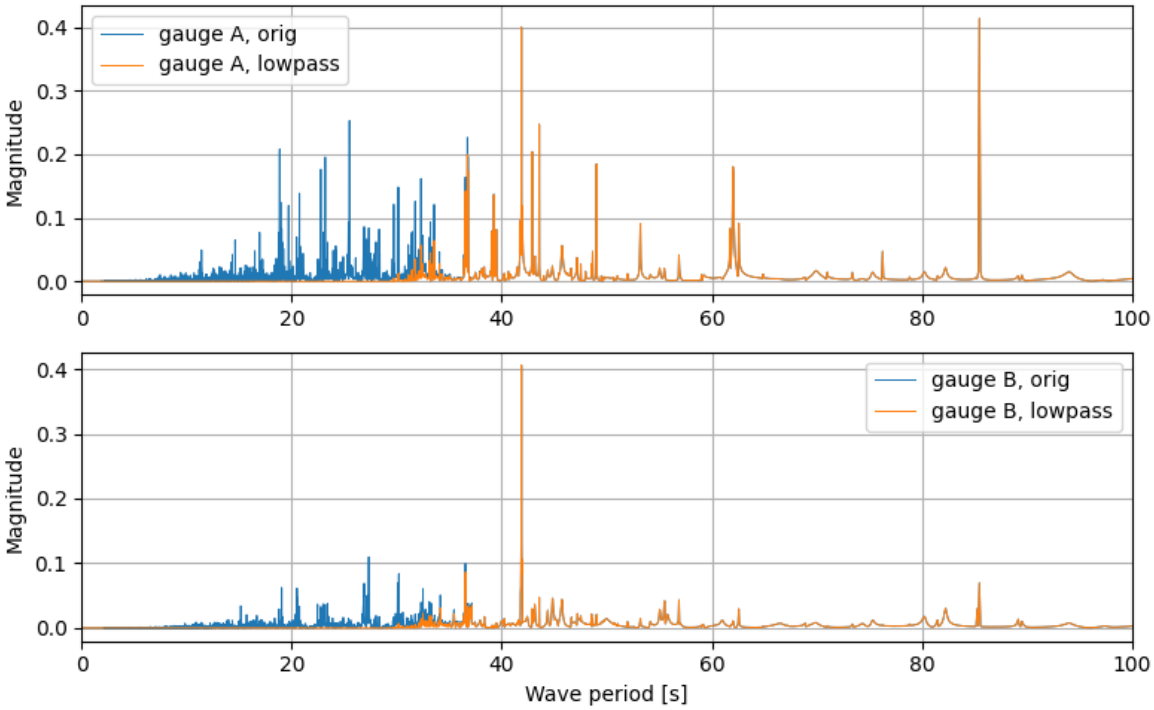

Fig. S38: *Wave period spectrum at gauges A (top) and B (bottom) for both original and lowpass filtered wave signal. The grid resolution is 12.5 m. In the legend, "orig" = unfiltered time series.*

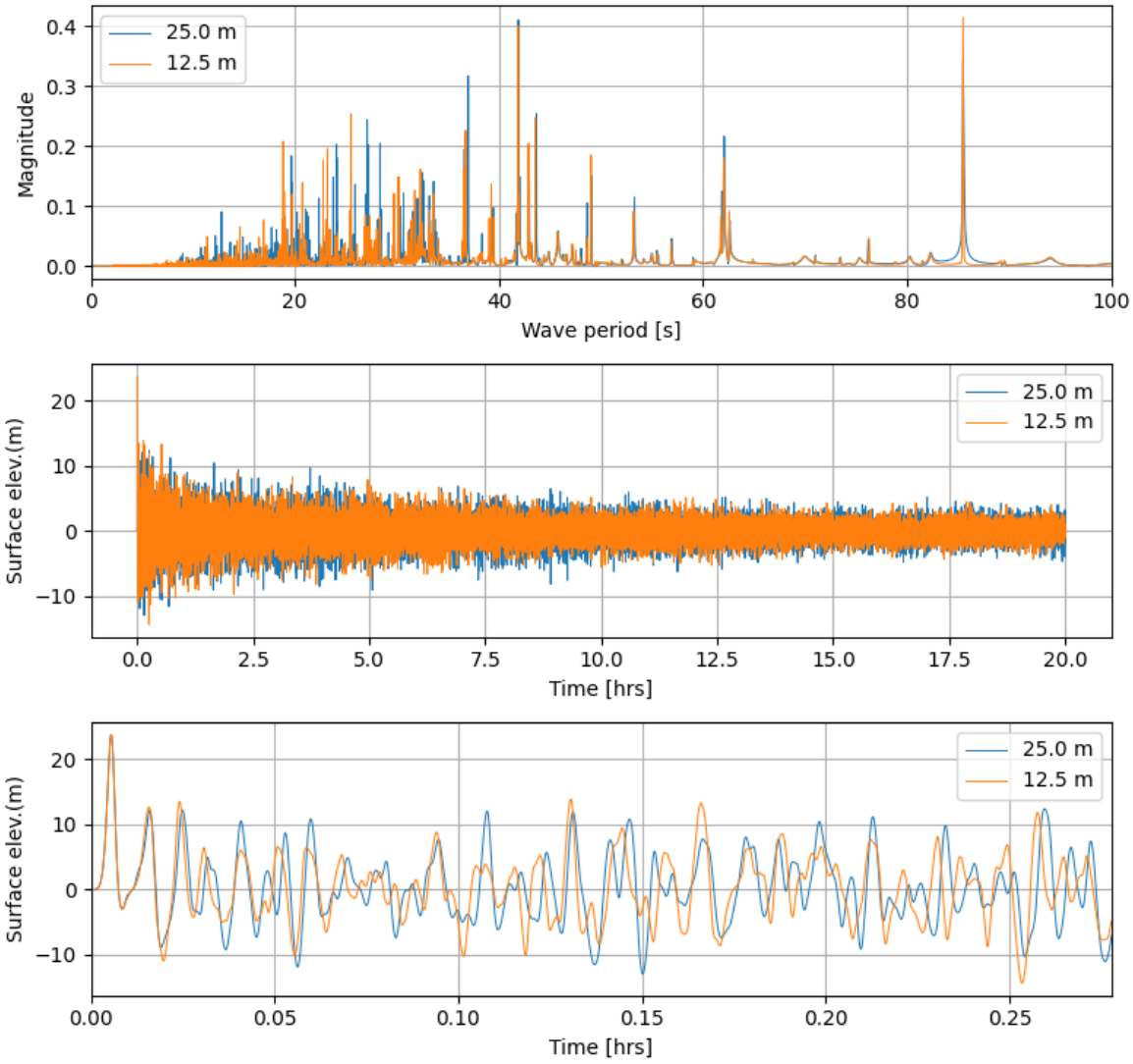

Fig. S39: *Grid refinement test at gauge A for the simulations with GloBouss with grid resolutions of 12.5 m and 25.0 m. From top to bottom panels, we respectively show the spectrum in wave period (computed for the first 10 hrs), entire wave signal, and first 1000 s of the wave signal.*

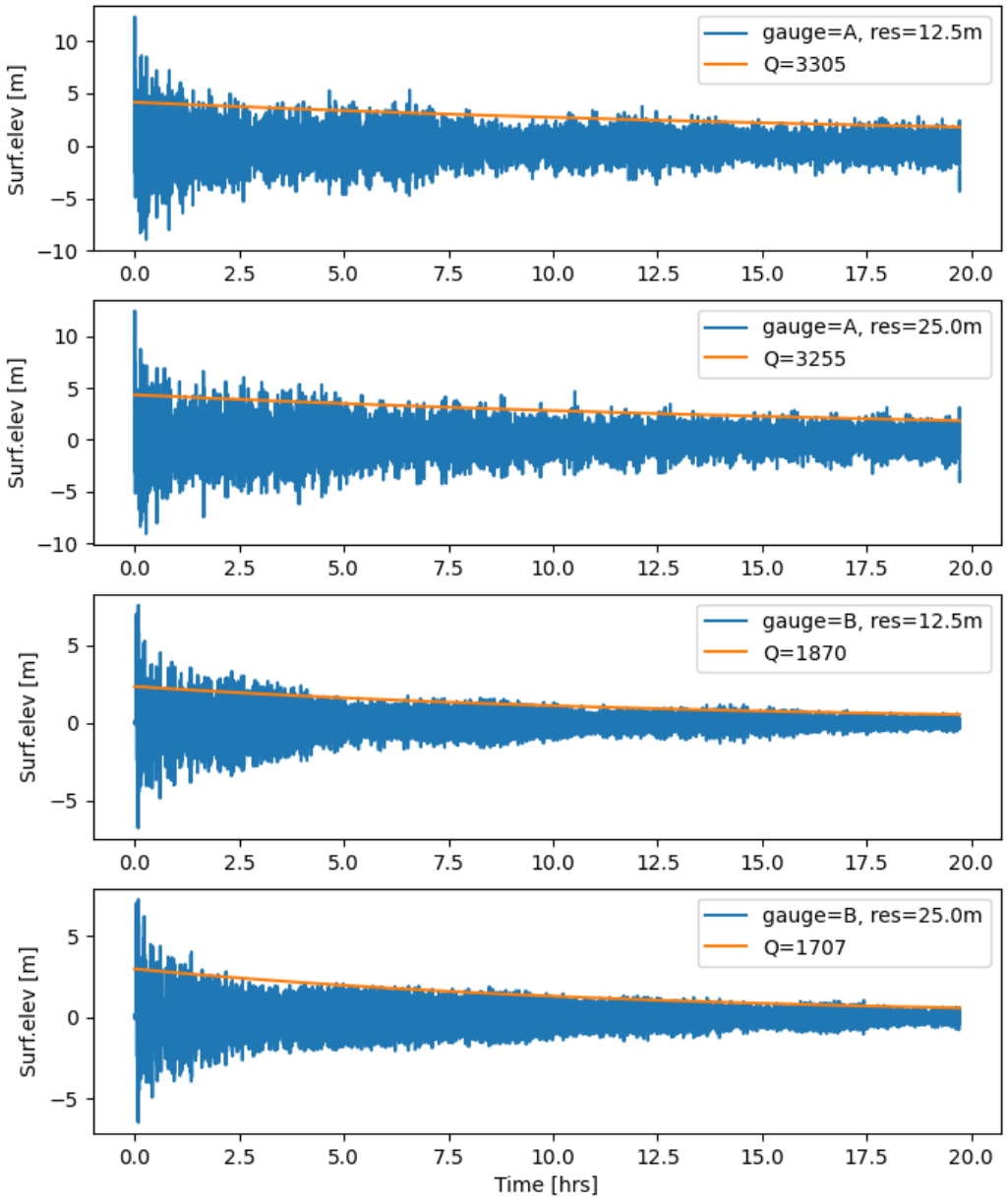

Fig. S40: *Computed damping factor (Q) based on curve fitting to a selection of wave peaks for a time window from 4 to 20 hours of tsunami propagation (lowpass-filtered signal). The Q values for different grid resolutions differ between 1.5% (gauge A) and 8% (gauge B).*

Supplementary Tables

Date	Time (UTC)	VLP	Trigger	Source of trigger information	Notes / special conditions	VLP observed duration	VLP frequency with 1σ errors (mHz)	VLP *Q*	Love node 1st harmonic	Love node 2nd harmonic	initial amplitude at DK.SCO.LHZ	initial amplitude at II.ALE.00.LHZ
2023-10-11	16:50	yes	Rock/ice avalanche?	Sentinel-2	Tsunami observed	~7 days	10.849 ±0.003	Initially 1500, after 10 hrs transition to *Q*=4000	N160°E	no observation	1.5 um; 100 nm/s; 7 nm/s²	0.75 um; 50 nm/s; 3.5 nm/s²
2023-09-16	12:35	yes	25.5 +/- 1.7 x10^6 m^3 Rock/ice avalanche	Field validation, Sentinel-2	Tsunami observed	~9 day	10.88 ±0.008	Initially 500 increasing with time to 3000	N160°E	N70°E	3.0 um; 200 nm/s; 14.0 nm/s²	1.5 um; 100 nm/s; 7 nm/s²
2017-01-20	08:10	yes	Snow/debris avalanche?	Sentinel-2 Sentinel-1	Run-out onto sea ice, sea ice disturbed by tsunami	20 hours	10.919 ±0.005	1200±300	insufficient horizontal signal	no observation	onset less clear; difficult to read	0.15 um; 10 nm/s; 0.7 nm/s²
2016-02-12	04:10	yes	Snow/debris avalanche?	Sentinel-2 Sentinel-1	Run-out onto sea ice	4 hours	11.017 ±0.020	650±250	insufficient signal		0.15 nm/s² +- 0.1 nm/s²	0.07 nm/s² +- 0.04 nm/s²
2013-09-30 to 2014-03-02	Unknown	not observed	Snow/debris avalanche?	Sentinel-2	Run-out onto sea ice	Not observed	n/a	n/a	n/a	n/a	n/a	n/a
2006-08-20	20:00	yes	Unknown		on II.ALE source region of VLP still under discussion	72 hours	10.906 ±0.010	5000±1000	insufficient signal		no data	0.06 nm/s² ±0.04 nm/s²
2005-08-30	06:00	yes	Unknown		on II.ALE source region of VLP still under discussion	36 hours	10.912 ±0.010	2000±1000	insufficient signal		no data	0.05 nm/s² ±0.04 nm/s²

Table S1*: Seismic source locations obtained in this study using different methods and data. List of very long-period (VLP) and landslide events referable to the glacial gully below Hvide Støvhorn in Dickson Fjord. During the course of our work on the 2023-09-16 landslide-tsunami-VLP event, we have identified six other such events. Three of these are observed both in the seismic record, while one is only seen in satellite data (Text S4) and two are only seen in the seismic record.*

Target	Approach	Frequency	Location	Method details
High-frequency (landslide)	NonLinLoc	~High	72.69N -27.34E	OT: 12:35:03.3. 7. P and S readings at SCO, DBG, SUMG (6 total).
	Regional waveform CMT Inversion	Landslide 0.04 Hz - 0.1 Hz	72.772N -26.796E	Grond (*183*). Max station distance = 1300 km
	IMS2.0 bulletin (CTBTO)	Landslide ~High?	72.9533N -27.1474E	OT: 12:35:34.95. Min dist: 8.5deg (II.BORG).
	Cross-correlation	Landslide	72.806N -25.1739E	
	First arrivals (GEUS)	Landslide	72.644N -27.151E	fixed to depth=0
Low-frequency (very long-period [VLP] event)	Beamforming VLP in heterogeneous Earth	VLP 10 mHz - 12 mHz	72.2N -25.1E	Model from LITHO1.0 (*161*)
	Beamforming VLP in homogeneous Earth	VLP 10 mHz - 12 mHz	72.2N -27.1E	4.1km/s best phase velocity
	Regional waveform CMT inversion	VLP 8 mHz - 15 mHz	73.93N -27.35E	Grond software (*183*). Used a resonating source-time function at 10.88 mHz (*47*). Max station distance = 1300 km
Hybrid	Automated Rayleigh wave stack-and-delay	25-100 s period	76.5N -31.5E (±1 deg)	Method / catalogue: (*184*)

Table S2: *Seismic source locations. OT = origin time*

	PGDh / PGDv (*y*-component)	**PGDh / PGDv (*z*-component)**
STA1 (400 km, *x*-direction)	500	*infinite (null z-component from vertical forces)*
STA2 (400 km, *y*-direction)	21.8	62.5

Table S3: *Simulation results for the relative importance of surface wave motion generated by the two sets of forces: ratio between the peak ground displacement generated by the horizontal forces (PGDh) and the vertical forces (PGDv) for both stations (STA1 and STA2) and both components. The two components are named "y-component" and "z-component" in the table.*

Multimedia Files

Movie S1

Time evolution over the first hour of the simulated seiche from the HySEA model (*dx* = 3 m; Manning = 0.03) along virtual gauges that corresponding to the X-X' line shown in Fig 5B. Gauge 0 corresponds to the landslide location; Gauge 20 is located on the shoreline directly opposite the landslide. In the movie, "t" denotes "time". "Military bathy" means the high-resolution, 3 m bathymetry model.

Movie S2

Time evolution over the two hours of the simulated seiche across the Dickson Fjord from the HySEA model (dx = 3 m; Manning = 0.03). The colorbar gives water elevation in meters. In the movie, "t" denotes "time", and the x-axis and y-axes correspond to easting and northing, respectively, with units of meters.

Movie S3

Teleseismic beamforming result showing the stack beampower and its peak location over ~10 days showing the stable location of the very long-period (VLP) seismic signal near Dickson Fjord. The inset map at the top-left shows stations used for the stack. The inset plot at the bottom shows the vertical waveform from DK.SCO, located ~300 km away from Dickson Fjord.

References and Notes

1. S. L. Gariano, F. Guzzetti, Landslides in a changing climate. *Earth Sci. Rev.* **162**, 227–252 (2016).

2. S. T. McColl, Paraglacial rock-slope stability. *Geomorphology* **153–154**, 1–16 (2012).

3. C. K. Ballantyne, P. Wilson, D. Gheorghiu, À. Rodés, Enhanced rock-slope failure following ice-sheet deglaciation: Timing and causes. *Earth Surf. Process. Landf.* **39**, 900–913 (2014).

4. A. I. Patton, S. L. Rathburn, D. M. Capps, Landslide response to climate change in permafrost regions. *Geomorphology* **340**, 116–128 (2019).

5. P. Saemundsson, C. Morino, S. J. Conway, "5.22 - Mass-Movements in Cold and Polar Climates" in *Treatise on Geomorphology*, J. F. Shroder, Ed. (Academic Press, ed. 2, 2022), pp. 350–370, 10.1016/B978-0-12-818234-5.00117-6.

6. C. B. Harbitz, S. Glimsdal, F. Løvholt, V. Kveldsvik, G. K. Pedersen, A. Jensen, Rockslide tsunamis in complex fjords: From an unstable rock slope at Åkerneset to tsunami risk in western Norway. *Coast. Eng.* **88**, 101–122 (2014).

7. F. Løvholt, G. Pedersen, C. B. Harbitz, S. Glimsdal, J. Kim, On the characteristics of landslide tsunamis. *Philos. Trans. A Math. Phys. Eng. Sci.* **373**, 20140376 (2015).

8. V. Heller, G. Ruffini, A critical review about generic subaerial landslide-tsunami experiments and options for a needed step change. *Earth Sci. Rev.* **242**, 104459 (2023).

9. P. Poulain, A. L. Friant, A. Mangeney, S. Viroulet, E. Fernandez-Nieto, M. Castro Diaz, M. Peruzzetto, G. Grandjean, F. Bouchut, R. Pedreros, J.-C. Komorowski, Performance and limits of a shallow-water model for landslide-generated tsunamis: From laboratory experiments to simulations of flank collapses at Montagne Pelée (Martinique). *Geophys. J. Int.* **233**, 796–825 (2023).

10. B. Higman, D. H. Shugar, C. P. Stark, G. Ekström, M. N. Koppes, P. Lynett, A. Dufresne, P. J. Haeussler, M. Geertsema, S. Gulick, A. Mattox, J. G. Venditti, M. A. L. Walton, N. McCall, E. Mckittrick, B. MacInnes, E. L. Bilderback, H. Tang, M. J. Willis, B. Richmond, R. S. Reece, C. Larsen, B. Olson, J. Capra, A. Ayca, C. Bloom, H. Williams, D. Bonno, R. Weiss, A. Keen, V. Skanavis, M. Loso, The 2015 landslide and tsunami in Taan Fiord, Alaska. *Sci. Rep.* **8**, 12993 (2018).

11. G. Lollino, A. Manconi, J. Locat, Y. Huang, M. Canals Artigas, Eds., *Engineering Geology for Society and Territory – Volume 4: Marine and Coastal Processes* (Springer International, 2014).

12. H. M. Fritz, F. Mohammed, J. Yoo, "Lituya Bay Landslide Impact Generated Mega-Tsunami 50th Anniversary" in *Tsunami Science Four Years after the 2004 Indian Ocean Tsunami: Part II: Observation and Data Analysis*, P. R. Cummins, K. Satake, L. S. L. Kong, Eds. (Birkhäuser, Basel, 2009), *Pageoph Topical Volumes*, pp. 153–175.

13. M. Geertsema, B. Menounos, G. Bullard, J. L. Carrivick, J. J. Clague, C. Dai, D. Donati, G. Ekstrom, J. M. Jackson, P. Lynett, M. Pichierri, A. Pon, D. H. Shugar, D. Stead, J. Del Bel Belluz, P. Friele, I. Giesbrecht, D. Heathfield, T. Millard, S. Nasonova, A. J. Schaeffer, B. C. Ward, D. Blaney, E. Blaney, C. Brillon, C. Bunn, W. Floyd, B. Higman, K. E. Hughes, W. McInnes, K. Mukherjee, M. A. Sharp, The 28 November 2020 Landslide, Tsunami, and Outburst Flood – A Hazard Cascade Associated With Rapid Deglaciation at Elliot Creek, British Columbia, Canada. *Geophys. Res. Lett.* **49**, e2021GL096716 (2022).

14. T. Dahl-Jensen, L. M. Larsen, S. A. S. Pedersen, J. Pedersen, H. F. Jepsen, G. Pedersen, T. Nielsen, A. K. Pedersen, F. Von Platen-Hallermund, W. Weng, Landslide and Tsunami 21 November 2000 in Paatuut, West Greenland. *Nat. Hazards* **31**, 277–287 (2004).

15. K. Svennevig, M. Keiding, N. J. Korsgaard, A. Lucas, M. Owen, M. D. Poulsen, J. Priebe, E. V. Sørensen, C. Morino, Uncovering a 70-year-old permafrost degradation induced disaster in the Arctic, the 1952 Niiortuut landslide-tsunami in central West Greenland. *Sci. Total Environ.* **859**, 160110 (2023).

16. K. Svennevig, R. L. Hermanns, M. Keiding, D. Binder, M. Citterio, T. Dahl-Jensen, S. Mertl, E. V. Sørensen, P. H. Voss, A large frozen debris avalanche entraining warming permafrost ground—The June 2021 Assapaat landslide, West Greenland. *Landslides* **19**, 2549–2567 (2022).

17. K. Svennevig, T. Dahl-Jensen, M. Keiding, J. P. Merryman Boncori, T. B. Larsen, S. Salehi, A. Munck Solgaard, P. H. Voss, Evolution of events before and after the 17 June 2017 rock avalanche at Karrat Fjord, West Greenland – a multidisciplinary approach to detecting and locating unstable rock slopes in a remote Arctic area. *Earth Surf. Dyn.* **8**, 1021–1038 (2020).

18. P. Favreau, A. Mangeney, A. Lucas, G. Crosta, F. Bouchut, Numerical modeling of landquakes. *Geophys. Res. Lett.* **37**, L15305 (2010).

19. G. Ekström, C. P. Stark, Simple scaling of catastrophic landslide dynamics. *Science* **339**, 1416–1419 (2013).

20. C. Hibert, G. Ekström, C. P. Stark, The relationship between bulk-mass momentum and short-period seismic radiation in catastrophic landslides. *J. Geophys. Res. Earth Surf.* **122**, 1201–1215 (2017).

21. W. Chao, T. Wu, K. Ma, Y. Kuo, Y. Wu, L. Zhao, M. Chung, H. Wu, Y. Tsai, The Large Greenland Landslide of 2017: Was a Tsunami Warning Possible? *Seismol. Res. Lett.* **89**, 1335–1344 (2018).

22. M. La Rocca, D. Galluzzo, G. Saccorotti, S. Tinti, G. B. Cimini, E. Del Pezzo, Seismic Signals Associated with Landslides and with a Tsunami at Stromboli Volcano, Italy. *Bull. Seismol. Soc. Am.* **94**, 1850–1867 (2004).

23. E. A. Kulikov, A. B. Rabinovich, R. E. Thomson, B. D. Bornhold, The landslide tsunami of November 3, 1994, Skagway Harbor, Alaska. *J. Geophys. Res.* **101** (C3), 6609–6615 (1996).

24. J. M. Amundson, J. F. Clinton, M. Fahnestock, M. Truffer, M. P. Lüthi, R. J. Motyka, Observing calving-generated ocean waves with coastal broadband seismometers, Jakobshavn Isbræ, Greenland. *Ann. Glaciol.* **53**, 79–84 (2012).

25. A. B. Rabinovich, "Seiches and Harbor Oscillations" in *Handbook of Coastal and Ocean Engineering*, Y. C. Kim, Ed. (World Scientific, 2009), pp. 193–236.

26. D. E. McNamara, A. T. Ringler, C. R. Hutt, L. S. Gee, Seismically observed seiching in the Panama Canal. *J. Geophys. Res.* **116** (B4), B04312 (2011).

27. L. Gualtieri, G. Ekström, Broad-band seismic analysis and modeling of the 2015 Taan Fjord, Alaska landslide using Instaseis. *Geophys. J. Int.* **213**, 1912–1923 (2018).

28. A. Paris, E. A. Okal, C. Guérin, P. Heinrich, F. Schindelé, H. Hébert, Numerical Modeling of the June 17, 2017 Landslide and Tsunami Events in Karrat Fjord, West Greenland. *Pure Appl. Geophys.* **176**, 3035–3057 (2019).

29. Materials and methods are available as supplementary materials.

30. R. Delannay, A. Valance, A. Mangeney, O. Roche, P. Richard, Granular and particle-laden flows: From laboratory experiments to field observations. *J. Phys. D Appl. Phys.* **50**, 053001 (2017).

31. A. Mangeney, Landslide boost from entrainment. *Nat. Geosci.* **4**, 77–78 (2011).

32. A. Dufresne, G. J. Wolken, C. Hibert, E. K. Bessette-Kirton, J. A. Coe, M. Geertsema, G. Ekström, The 2016 Lamplugh rock avalanche, Alaska: Deposit structures and emplacement dynamics. *Landslides* **16**, 2301–2319 (2019).

33. L. Moretti, A. Mangeney, F. Walter, Y. Capdeville, T. Bodin, E. Stutzmann, A. Le Friant, Constraining landslide characteristics with Bayesian inversion of field and seismic data. *Geophys. J. Int.* **221**, 1341–1348 (2020).

34. C. Hibert, G. Ekström, C. P. Stark, Dynamics of the Bingham Canyon Mine landslides from seismic signal analysis. *Geophys. Res. Lett.* **41**, 4535–4541 (2014).

35. L. Moretti, K. Allstadt, A. Mangeney, Y. Capdeville, E. Stutzmann, F. Bouchut, Numerical modeling of the Mount Meager landslide constrained by its force history derived from seismic data. *J. Geophys. Res. Solid Earth* **120**, 2579–2599 (2015).

36. M. I. Arran, A. Mangeney, J. De Rosny, M. Farin, R. Toussaint, O. Roche, Laboratory Landquakes: Insights From Experiments Into the High-Frequency Seismic Signal Generated by Geophysical Granular Flows. *J. Geophys. Res. Earth Surf.* **126**, e2021JF006172 (2021).

37. L. Moretti, A. Mangeney, Y. Capdeville, E. Stutzmann, C. Huggel, D. Schneider, F. Bouchut, Numerical modeling of the Mount Steller landslide flow history and of the generated long period seismic waves. *Geophys. Res. Lett.* **39**, L16402 (2012).

38. W. Boone, L. Ponsoni, G. Johnen, S. Rysgaard, "New technologies and insights from a real-time monitoring system of sea ice and oceanographic conditions in Northeast Greenland," EGU General Assembly 2023, Vienna, Austria, 24 to 28 April, Abstract EGU23-14430 (2023); https://doi.org/10.5194/egusphere-egu23-14430.

39. J. Macías, C. Escalante, M. J. Castro, Multilayer-HySEA model validation for landslide-generated tsunamis – Part 1: Rigid slides. *Nat. Hazards Earth Syst. Sci.* **21**, 775–789 (2021).

40. G. Davies, F. Romano, S. Lorito, Global Dissipation Models for Simulating Tsunamis at Far-Field Coasts up to 60 hours Post-Earthquake: Multi-Site Tests in Australia. *Front. Earth Sci. (Lausanne)* **8**, 598235 (2020).

41. D. Giles, E. Kashdan, D. M. Salmanidou, S. Guillas, F. Dias, Performance analysis of Volna-OP2 – massively parallel code for tsunami modelling. *Comput. Fluids* **209**, 104649 (2020).

42. H. Q. Rif'atin, I. Magdalena, Seiches in a Closed Basin of Various Geometric Shape. *J. Phys. Conf. Ser.* **1245**, 012061 (2019).

43. G. Pedersen, F. Løvholt, Documentation of a global Boussinesq solver, Preprint Series in Applied Mathematics 1, Dept. of Mathematics, University of Oslo, Norway (2008); https://www.ngi.no/globalassets/dokumenter/prosjekter/icg/globous-model-01-08.pdf.

44. A. T. Ringler, R. E. Anthony, R. C. Aster, C. J. Ammon, S. Arrowsmith, H. Benz, C. Ebeling, A. Frassetto, W.-Y. Kim, P. Koelemeijer, H. C. P. Lau, V. Lekić, J. P. Montagner, P. G. Richards, D. P. Schaff, M. Vallée, W. Yeck, Achievements and Prospects of Global Broadband Seismographic Networks After 30 Years of Continuous Geophysical Observations. *Rev. Geophys.* **60**, e2021RG000749 (2022).

45. N. Leroy, M. Vallée, D. Zigone, B. Romanowicz, E. Stutzmann, A. Maggi, C. Pardo, J. Montagner, M. Bes de Berc, C. Broucke, S. Bonaimé, G. Roult, J. Thoré, A. Bernard, M. Le Cocq, O. Sirol, L. Rivera, J. Lévêque, M. Cara, F. Pesqueira, GEOSCOPE Network: 40 Yr of Global Broadband Seismic Data. *Seismol. Res. Lett.* **95**, 1495–1517 (2023).

46. B. P. Lipovsky, E. M. Dunham, Vibrational modes of hydraulic fractures: Inference of fracture geometry from resonant frequencies and attenuation. *J. Geophys. Res. Solid Earth* **120**, 1080–1107 (2015).

47. S. Cesca, J. Letort, H. N. T. Razafindrakoto, S. Heimann, E. Rivalta, M. P. Isken, M. Nikkhoo, L. Passarelli, G. M. Petersen, F. Cotton, T. Dahm, Drainage of a deep magma reservoir near Mayotte inferred from seismicity and deformation. *Nat. Geosci.* **13**, 87–93 (2020).

48. H. Kanamori, J. Mori, Harmonic excitation of mantle Rayleigh waves by the 1991 eruption of Mount Pinatubo, Philippines. *Geophys. Res. Lett.* **19**, 721–724 (1992).

49. R. Widmer, W. Zürn, Bichromatic excitation of long-period Rayleigh and air waves by the Mount Pinatubo and El Chichon volcanic eruptions. *Geophys. Res. Lett.* **19**, 765–768 (1992).

50. A. M. Dziewonski, D. L. Anderson, Preliminary reference Earth model. *Phys. Earth Planet. Inter.* **25**, 297–356 (1981).

51. S. Allgeyer, H. Hébert, R. Madariaga, Modelling the tsunami free oscillations in the Marquesas (French Polynesia). *Geophys. J. Int.* **193**, 1447–1459 (2013).

52. L. Gualtieri, G. Ekström, Broad-band seismic analysis and modeling of the 2015 Taan Fjord, Alaska landslide using Instaseis. *Geophys. J. Int.* **213**, 1912–1923 (2018).

53. A. Farhadzadeh, A study of Lake Erie seiche and low frequency water level fluctuations in the presence of surface ice. *Ocean Eng.* **135**, 117–136 (2017).

54. L. Padman, M. R. Siegfried, H. A. Fricker, Ocean Tide Influences on the Antarctic and Greenland Ice Sheets. *Rev. Geophys.* **56**, 142–184 (2018).

55. P. Weatherall, K. M. Marks, M. Jakobsson, T. Schmitt, S. Tani, J. E. Arndt, M. Rovere, D. Chayes, V. Ferrini, R. Wigley, A new digital bathymetric model of the world's oceans. *Earth Space Sci.* **2**, 331–345 (2015).

56. P. Poulain, A. L. Friant, R. Pedreros, A. Mangeney, A. G. Filippini, G. Grandjean, A. Lemoine, E. D. Fernández-Nieto, M. J. C. Díaz, M. Peruzzetto, Numerical simulation of submarine landslides and generated tsunamis: Application to the on-going Mayotte seismo-volcanic crisis. *C. R. Geosci.* **354**, 361–390 (2022).

57. M. Bajo, I. Međugorac, G. Umgiesser, M. Orlić, Storm surge and seiche modelling in the Adriatic Sea and the impact of data assimilation. *Q. J. R. Meteorol. Soc.* **145**, 2070–2084 (2019).

58. M. Okihiro, R. T. Guza, Observations of Seiche Forcing and Amplification in Three Small Harbors. *J. Waterw. Port Coast. Ocean Eng.* **122**, 232–238 (1996).

59. J. Park, J. MacMahan, W. V. Sweet, K. Kotun, Continuous seiche in bays and harbors. *Ocean Sci.* **12**, 355–368 (2016).

60. M. Heidarzadeh, A. Muhari, A. B. Wijanarto, Insights on the Source of the 28 September 2018 Sulawesi Tsunami, Indonesia Based on Spectral Analyses and Numerical Simulations. *Pure Appl. Geophys.* **176**, 25–43 (2019).

61. S. Schippkus, S. Hicks, T. Forbriger, S. Glimsdal, W. Boone, C. Satriano, T. Lecocq, ROBelgium/VLPGreenland: Accepted version, Zenodo (2024); https://doi.org/10.5281/zenodo.13221192.

62. W. Boone, S. Rysgaard, E. R. Frandsen, R. Develter, Flanders Marine Institute (VLIZ), Belgium, University Of Aarhus (AU), Denmark, Greenland Integrated Observatory - CTD & Atmospheric Station Dickson Fjord - 2023, Marine Data Archive (2023). https://doi.org/10.14284/637.

63. C. Porter, I. Howat, M.-J. Noh, E. Husby, S. Khuvis, E. Danish, K. Tomko, J. Gardiner, A. Negrete, B. Yadav, J. Klassen, C. Kelleher, M. Cloutier, J. Bakker, J. Enos, G. Arnold, G. Bauer, P. Morin, ArcticDEM - Mosaics, Version 4.1, Harvard Dataverse (2023); 10.7910/DVN/3VDC4W.

64. D. Lague, N. Brodu, J. Leroux, Accurate 3D comparison of complex topography with terrestrial laser scanner: Application to the Rangitikei canyon (N-Z). *ISPRS J. Photogramm. Remote Sens.* **82**, 10–26 (2013).

65. K. L. Cook, M. Dietze, Short Communication: A simple workflow for robust low-cost UAV-derived change detection without ground control points. *Earth Surf. Dyn.* **7**, 1009–1017 (2019).

66. J. L. Carrivick, C. M. Boston, J. L. Sutherland, D. Pearce, H. Armstrong, A. Bjørk, K. K. Kjeldsen, J. Abermann, R. P. Oien, M. Grimes, W. H. M. James, M. W. Smith, Mass Loss of Glaciers and Ice Caps Across Greenland Since the Little Ice Age. *Geophys. Res. Lett.* **50**, e2023GL103950 (2023).

67. C. Nuth, A. Kääb, Co-registration and bias corrections of satellite elevation data sets for quantifying glacier thickness change. *Cryosphere* **5**, 271–290 (2011).

68. N. J. Korsgaard, C. Nuth, S. A. Khan, K. K. Kjeldsen, A. A. Bjørk, A. Schomacker, K. H. Kjær, Digital elevation model and orthophotographs of Greenland based on aerial photographs from 1978-1987. *Sci. Data* **3**, 160032 (2016).

69. SDFI (Agency for Data Supply and Infrastructure), Åbent Land Grønland - Disko bugt [Vektordata, 1:50.000](2024); https://dataforsyningen.dk/data/4771.

70. R. Hugonnet, R. McNabb, E. Berthier, B. Menounos, C. Nuth, L. Girod, D. Farinotti, M. Huss, I. Dussaillant, F. Brun, A. Kääb, Accelerated global glacier mass loss in the early twenty-first century. *Nature* **592**, 726–731 (2021).

71. S. Rysgaard, K. Bjerge, W. Boone, E. Frandsen, M. Graversen, T. Thomas Høye, B. Jensen, G. Johnen, M. Antoni Jackowicz-Korczynski, J. Taylor Kerby, S. Kortegaard, M. Mastepanov, C. Melvad, P. Schmidt Mikkelsen, K. Mortensen, C. Nørgaard, E. Poulsen, T. Riis, L. Sørensen, T. Røjle Christensen, A mobile observatory powered by sun and wind for near real time measurements of atmospheric, glacial, terrestrial, limnic and coastal oceanic conditions in remote off-grid areas. *HardwareX* **12**, e00331 (2022).

72. European Space Agency (ESA), Sentinel-2 L1C, Sentinel Hub EO Browser (2023); https://sentinelshare.page.link/Wsz2.

73. L. G. Evers, "The inaudible symphony: On the detection and source identification of atmospheric infrasound," thesis, Delft University of Technology (2008).

74. J. Assink, jdassink/beamforming: v1.0.0, Zenodo (2023); https://doi.org/10.5281/ZENODO.10260260.

75. R. Waxler, C. H. Hetzer, J. D. Assink, P. Blom, A two-dimensional effective sound speed parabolic equation model for infrasound propagation with ground topography. *J. Acoust. Soc. Am.* **152**, 3659–3669 (2022).

76. R. Waxler, C. Hetzer, J. Assink, D. Velea, chetzer-ncpa/ncpaprop-release: NCPAprop v2.1.0, version v2.1.0, Zenodo (2021). https://doi.org/10.5281/ZENODO.5562712.

77. P. Blom, Modeling infrasonic propagation through a spherical atmospheric layer-Analysis of the stratospheric pair. *J. Acoust. Soc. Am.* **145**, 2198–2208 (2019).

78. E. E. Brodsky, E. Gordeev, H. Kanamori, Landslide basal friction as measured by seismic waves. *Geophys. Res. Lett.* **30**, 2236 (2003).

79. K. Allstadt, Extracting source characteristics and dynamics of the August 2010 Mount Meager landslide from broadband seismograms. *J. Geophys. Res. Earth Surf.* **118**, 1472–1490 (2013).

80. C. Hibert, C. P. Stark, G. Ekström, Dynamics of the Oso-Steelhead landslide from broadband seismic analysis. *Nat. Hazards Earth Syst. Sci.* **15**, 1265–1273 (2015).

81. L. Toney, K. E. Allstadt, lsforce: A Python-Based Single-Force Seismic Inversion Framework for Massive Landslides. *Seismol. Res. Lett.* **92**, 2610–2626 (2021).

82. G. Ekström, A global model of Love and Rayleigh surface wave dispersion and anisotropy, 25-250 s. *Geophys. J. Int.* **187**, 1668–1686 (2011).

83. B. L. N. Kennett, E. R. Engdahl, iasp91 velocity model, EarthScope Earth Model Collaboration (1991); https://ds.iris.edu/spud/earthmodel/9991809.

84. F. Løvholt, G. K. Pedersen, S. Glimsdal, Coupling of dispersive tsunami propagation and shallow water coastal response. *Open Oceanogr. J.* **4**, 71–82 (2010).

85. F. Løvholt, G. Pedersen, G. Gisler, Oceanic propagation of a potential tsunami from the La Palma Island. *J. Geophys. Res.* **113**, C09026 (2008).

86. V. V. Titov, C. E. Synolakis, Numerical Modeling of Tidal Wave Runup. *J. Waterw. Port Coast. Ocean Eng.* **124**, 157–171 (1998).

87. F. Løvholt, S. Glimsdal, P. Lynett, G. Pedersen, Simulating tsunami propagation in fjords with long-wave models. *Nat. Hazards Earth Syst. Sci.* **15**, 657–669 (2015).

88. F. Løvholt, S. Glimsdal, C. B. Harbitz, On the landslide tsunami uncertainty and hazard. *Landslides* **17**, 2301–2315 (2020).

89. J. Kim, "Finite volume methods for tsunamis generated by submarine landslides," thesis, University of Washington, Washington (2014).

90. E. D. Fernández-Nieto, F. Bouchut, D. Bresch, M. J. Castro Díaz, A. Mangeney, A new Savage–Hutter type model for submarine avalanches and generated tsunami. *J. Comput. Phys.* **227**, 7720–7754 (2008).

91. O. Pouliquen, Y. Forterre, Friction law for dense granular flows: Application to the motion of a mass down a rough inclined plane. *J. Fluid Mech.* **453**, 133–151 (2002).

92. M. Brunet, L. Moretti, A. Le Friant, A. Mangeney, E. D. Fernández Nieto, F. Bouchut, Numerical simulation of the 30–45 ka debris avalanche flow of Montagne Pelée volcano, Martinique: From volcano flank collapse to submarine emplacement. *Nat. Hazards* **87**, 1189–1222 (2017).

93. A. Le Friant, G. Boudon, C. Deplus, B. Villemant, Large-scale flank collapse events during the activity of Montagne Pelée, Martinique, Lesser Antilles. *J. Geophys. Res.* **108** (B1), 2055 (2003).

94. J. T. Kirby, S. T. Grilli, J. Horrillo, P. L.-F. Liu, D. Nicolsky, S. Abadie, B. Ataie-Ashtiani, M. J. Castro, L. Clous, C. Escalante, I. Fine, J. M. González-Vida, F. Løvholt, P. Lynett, G. Ma, J. Macías, S. Ortega, F. Shi, S. Yavari-Ramshe, C. Zhang,

Validation and inter-comparison of models for landslide tsunami generation. *Ocean Model. (Oxf.)* **170**, 101943 (2022).

95. T. Esposti Ongaro, M. de' Michieli Vitturi, M. Cerminara, A. Fornaciai, L. Nannipieri, M. Favalli, B. Calusi, J. Macías, M. J. Castro, S. Ortega, J. M. González-Vida, C. Escalante, Modeling Tsunamis Generated by Submarine Landslides at Stromboli Volcano (Aeolian Islands, Italy): A Numerical Benchmark Study. *Front. Earth Sci. (Lausanne)* **9**, 628652 (2021).

96. Alaska Earthquake Center, Univ. of Alaska Fairbanks, Alaska Geophysical Network, International Federation of Digital Seismograph Networks (1987); https://doi.org/10.7914/SN/AK.

97. Alfred Wegener Institute For Polar And Marine Research (AWI), AWI Network Antarctica, GFZ Data Services (1993); https://doi.org/10.14470/NJ617293.

98. F. Vernon, ANZA Regional Network, International Federation of Digital Seismograph Networks (1982); https://doi.org/10.7914/SN/AZ.

99. Royal Observatory of Belgium, Belgian Seismic Network, International Federation of Digital Seismograph Networks (1985). https://doi.org/10.7914/SN/BE.

100. Northern California Earthquake Data Center, Berkeley Digital Seismic Network (BDSN), UC Berkeley Seismological Laboratory (2014); https://doi.org/10.7932/BDSN.

101. Colorado Geological Survey, Colorado Geological Survey Seismic Network, International Federation of Digital Seismograph Networks (2016); https://doi.org/10.7914/SN/C0.

102. Universidad de Chile, Red Sismologica Nacional, International Federation of Digital Seismograph Networks (2012); https://doi.org/10.7914/SN/C1.

103. Swiss Seismological Service (SED) at ETH Zurich, National Seismic Networks of Switzerland (1983); https://doi.org/10.12686/SED/NETWORKS/CH.

104. California Institute of Technology and United States Geological Survey Pasadena, Southern California Seismic Network, International Federation of Digital Seismograph Networks (1926); https://doi.org/10.7914/SN/CI.

105. University of South Carolina, South Carolina Seismic Network, International Federation of Digital Seismograph Networks (1987); https://doi.org/10.7914/SN/CO.

106. Albuquerque Seismological Laboratory (ASL)/USGS, Caribbean USGS Network, International Federation of Digital Seismograph Networks (2006); https://doi.org/10.7914/SN/CU.

107. GFZ German Research Centre For Geosciences, Institut Des Sciences De L'Univers-Centre National De La Recherche CNRS-INSU, IPOC Seismic Network, Integrated Plate boundary Observatory Chile - IPOC (2006); https://doi.org/10.14470/PK615318.

108. RESIF, RESIF-RLBP French Broad-band network, RESIF-RAP strong motion network and other seismic stations in metropolitan France, RESIF - Réseau Sismologique et géodésique Français (1995); https://doi.org/10.15778/RESIF.FR.

109. Institut De Physique Du Globe De Paris (IPGP), Ecole Et Observatoire Des Sciences De La Terre De Strasbourg (EOST), GEOSCOPE, French Global Network of Broad Band Seismic Stations (IPGP), Université de Paris (1982); https://doi.org/10.18715/GEOSCOPE.G.

110. GEOFON Data Centre, GEOFON Seismic Network, GFZ Data Services (1993); https://doi.org/10.14470/TR560404.

111. Federal Institute for Geosciences and Natural Resources, German Regional Seismic Network (GRSN) (1976); https://doi.org/10.25928/MBX6-HR74.

112. Albuquerque Seismological Laboratory (ASL)/USGS, US Geological Survey Networks, International Federation of Digital Seismograph Networks (1980); https://doi.org/10.7914/SN/GS.

113. University of Genoa, Regional Seismic Network of North Western Italy, International Federation of Digital Seismograph Networks (1967); https://doi.org/10.7914/SN/GU.

114. Albuquerque Seismological Laboratory (ASL)/USGS, New China Digital Seismograph Network, International Federation of Digital Seismograph Networks (1992); https://doi.org/10.7914/SN/IC.

115. Scripps Institution of Oceanography, Global Seismograph Network - IRIS/IDA, International Federation of Digital Seismograph Networks (1986); https://doi.org/10.7914/SN/II.

116. Black Forest Observatory (BFO), Black Forest Observatory Data, GFZ Data Services (1971); https://doi.org/10.5880/BFO.

117. Albuquerque Seismological Laboratory/USGS, Global Seismograph Network, (GSN - IRIS/USGS), International Federation of Digital Seismograph Networks (2014); https://doi.org/10.7914/SN/IU.

118. Istituto Nazionale di Geofisica e Vulcanologia (INGV), Rete Sismica Nazionale (RSN) (2005); https://doi.org/10.13127/SD/X0FXNH7QFY.

119. Albuquerque Seismological Laboratory (ASL)/USGS, Intermountain West Seismic Network, International Federation of Digital Seismograph Networks (2003); https://doi.org/10.7914/SN/IW.

120. Central Asian Institute for Applied Geosciences, Central Asian Seismic Network of CAIAG, International Federation of Digital Seismograph Networks (2008); https://doi.org/10.7914/SN/KC.

121. Lamont Doherty Earth Observatory (LDEO), Columbia University, Lamont-Doherty Cooperative Seismographic Network, International Federation of Digital Seismograph Networks (1970); https://doi.org/10.7914/SN/LD.

122. Instituto Dom Luiz (IDL) - Faculdade de Ciências da Universidade de Lisboa, International Federation of Digital Seismograph Networks (2003); https://doi.org/10.7914/SN/LX.

123. Department of Meteorology and Hydrology - National Earthquake Data Center, Myanmar National Seismic Network, International Federation of Digital Seismograph Networks (2016); https://doi.org/10.7914/SN/MM.

124. MedNet Project Partner Institutions, Mediterranean Very Broadband Seismographic Network, (MedNet) (1990); https://doi.org/10.13127/SD/FBBBTDTD6Q.

125. Albuquerque Seismological Laboratory/USGS, Central and Eastern US Network, International Federation of Digital Seismograph Networks (2013); https://doi.org/10.7914/SN/N4.

126. Royal Netherlands Meteorological Institute (KNMI), Caribbean Netherlands Seismic Network (2006); https://doi.org/10.21944/dffa7a3f-7e3a-3b33-a436-516a01b6af3f.

127. USGS Menlo Park, USGS Northern California Seismic Network, International Federation of Digital Seismograph Networks (1966); https://doi.org/10.7914/SN/NC.

128. Utrecht University (UU Netherlands), NARS, International Federation of Digital Seismograph Networks (1983); https://doi.org/10.7914/SN/NR.

129. Instituto Nicaraguense de Estudios Territoriales (INETER), Nicaraguan Seismic Network, International Federation of Digital Seismograph Networks (1975); https://doi.org/10.7914/SN/NU.

130. GNS Science, GeoNet Aotearoa New Zealand Seismic Digital Waveform Dataset, GNS Science (2021); https://doi.org/10.21420/G19Y-9D40.

131. Rutgers University, Ocean Observatories Initiative, International Federation of Digital Seismograph Networks (2013); https://doi.org/10.7914/SN/OO.

132. Instituto Português do Mar e da Atmosfera, I.P., Portuguese National Seismic Network, International Federation of Digital Seismograph Networks (2006); https://doi.org/10.7914/SN/PM.

133. F. Vernon, Piñon Flats Observatory Array, International Federation of Digital Seismograph Networks (2014); https://doi.org/10.7914/SN/PY.

134. Regional Integrated Multi-Hazard Early Warning System (RIMES Thailand), International Federation of Digital Seismograph Networks (2008); https://doi.org/10.7914/SN/RM.

135. Ruhr University Bochum, RuhrNet - Seismic Network of the Ruhr-University Bochum, Federal Institute for Geosciences and Natural Resources (BGR, Germany) (2007); https://doi.org/10.7914/SN/RN.

136. U. C. Santa Barbara, UC Santa Barbara Engineering Seismology Network, International Federation of Digital Seismograph Networks (1989); https://doi.org/10.7914/SN/SB.

137. Multiple Operators, International Geodynamics and Earth Tide Service, International Federation of Digital Seismograph Networks (1997); https://doi.org/10.7914/SN/SG.

138. Slovenian Environment Agency, Seismic Network of the Republic of Slovenia, International Federation of Digital Seismograph Networks (1990); https://doi.org/10.7914/SN/SL.

139. University of Leipzig, SXNET Saxon Seismic Network, International Federation of Digital Seismograph Networks (2001); https://doi.org/10.7914/SN/SX.

140. Institut fuer Geowissenschaften, Friedrich-Schiller-Universitaet Jena, Thüringer Seismologisches Netz, International Federation of Digital Seismograph Networks (2009); https://doi.org/10.7914/SN/TH.

141. Institute of Earth Sciences, Academia Sinica, Taiwan, Broadband Array in Taiwan for Seismology, International Federation of Digital Seismograph Networks (1996); https://doi.org/10.7914/SN/TW.

142. Swedish National Seismic Network, Swedish National Seismic Network, Uppsala University, Uppsala, Sweden (1904); https://doi.org/10.18159/SNSN.

143. Albuquerque Seismological Laboratory (ASL)/USGS, United States National Seismic Network, International Federation of Digital Seismograph Networks (1990); https://doi.org/10.7914/SN/US.

144. Institut De Physique Du Globe De Paris (IPGP), GNSS, Seismic Broadband and Strong Motion Permanent Networks in West Indies (IPGP), Université de Paris 2008; https://doi.org/10.18715/ANTILLES.WI.

145. San Fernando Royal Naval Observatory (ROA), Universidad Complutense De Madrid (UCM), Helmholtz-Zentrum Potsdam Deutsches GeoForschungsZentrum (GFZ), P. Universidade De Évora (UEVORA, Portugal), Institute Scientifique Of Rabat (ISRABAT, Morocco): The Western Mediterranean BB Seismic Network, GFZ Data Services (1996); https://doi.org/10.14470/JZ581150.

146. Idaho Geological Survey, Idaho Seismic Network, International Federation of Digital Seismograph Networks (2022); https://doi.org/10.7914/SN/WW.

147. University of Utah, Yellowstone National Park Seismograph Network, International Federation of Digital Seismograph Networks (1983); https://doi.org/10.7914/SN/WY.

148. C. A. Dalton, G. Ekström, Global models of surface wave attenuation. *J. Geophys. Res.* **111** (B5), 2005JB003997 (2006).

149. W. Zürn, P. A. Rydelek, Revisiting the Phasor-Walkout method for detailed investigation of harmonic signals in time series. *Surv. Geophys.* **15**, 409–431 (1994).

150. L. Krischer, T. Megies, R. Barsch, M. Beyreuther, T. Lecocq, C. Caudron, J. Wassermann, ObsPy: A bridge for seismology into the scientific Python ecosystem. *Comput. Sci. Discov.* **8**, 014003 (2015).

151. M. Beyreuther, R. Barsch, L. Krischer, T. Megies, Y. Behr, J. Wassermann, ObsPy: A Python Toolbox for Seismology. *Seismol. Res. Lett.* **81**, 530–533 (2010).

152. G. G. Sorrells, A Preliminary Investigation into the Relationship between Long-Period Seismic Noise and Local Fluctuations in the Atmospheric Pressure Field. *Geophys. J. R. Astron. Soc.* **26**, 71–82 (2010).

153. R. Beauduin, P. Lognonné, J. P. Montagner, S. Cacho, J. F. Karczewski, M. Morand, The effects of the atmospheric pressure changes on seismic signals or how to improve the quality of a station. *Bull. Seismol. Soc. Am.* **86**, 1760–1769 (1996).

154. A. C. B. Alejandro, A. T. Ringler, D. C. Wilson, R. E. Anthony, S. V. Moore, Towards understanding relationships between atmospheric pressure variations and long-period horizontal seismic data: A case study. *Geophys. J. Int.* **223**, 676–691 (2020).

155. P. W. Rodgers, The response of the horizontal pendulum seismometer to Rayleigh and Love waves, tilt, and free oscillations of the earth. *Bull. Seismol. Soc. Am.* **58**, 1385–1406 (1968).

156. A. B. Baggeroer, W. A. Kuperman, H. Schmidt, Matched field processing: Source localization in correlated noise as an optimum parameter estimation problem. *J. Acoust. Soc. Am.* **83**, 571–587 (1988).

157. S. Rost, C. Thomas, Array Seismology: Methods and Applications. *Rev. Geophys.* **40**, 1008 (2002).

158. L. Li, J. Tan, B. Schwarz, F. Staněk, N. Poiata, P. Shi, L. Diekmann, L. Eisner, D. Gajewski, Recent Advances and Challenges of Waveform-Based Seismic Location Methods at Multiple Scales. *Rev. Geophys.* **58**, e2019RG000667 (2020).

159. E. Ruigrok, S. Gibbons, K. Wapenaar, Cross-correlation beamforming. *J. Seismol.* **21**, 495–508 (2017).

160. M. E. Pasyanos, T. G. Masters, G. Laske, Z. Ma, LITHO1.0: An updated crust and lithospheric model of the Earth. *J. Geophys. Res. Solid Earth* **119**, 2153–2173 (2014).

161. J. A. Sethian, Fast Marching Methods. *SIAM Rev.* **41**, 199–235 (1999).

162. M. Gal, A. M. Reading, N. Rawlinson, V. Schulte-Pelkum, Matched Field Processing of Three-Component Seismic Array Data Applied to Rayleigh and Love Microseisms. *J. Geophys. Res. Solid Earth* **123**, 6871–6889 (2018).

163. M. C. A. White, H. Fang, N. Nakata, Y. Ben-Zion, PyKonal: A Python Package for Solving the Eikonal Equation in Spherical and Cartesian Coordinates Using the Fast Marching Method. *Seismol. Res. Lett.* **91**, 2378–2389 (2020).

164. Z. Xu, T. D. Mikesell, Estimation of Resolution and Covariance of Ambient Seismic Source Distributions: Full Waveform Inversion and Matched Field Processing. *J. Geophys. Res. Solid Earth* **127**, e2022JB024374 (2022).

165. S. Schippkus, C. Hadziioannou, Matched field processing accounting for complex Earth structure: Method and review. *Geophys. J. Int.* **231**, 1268–1282 (2022).

166. S. Schippkus, schipp/fast_beamforming: 2023-09-04 first release, Version v1, Zenodo (2023); https://doi.org/10.5281/ZENODO.8315028.

167. A. R. Hutko, M. Bahavar, C. Trabant, R. T. Weekly, M. V. Fossen, T. Ahern, Data Products at the IRIS-DMC: Growth and Usage. *Seismol. Res. Lett.* **88**, 892–903 (2017).

168. M. van Driel, L. Krischer, S. C. Stähler, K. Hosseini, T. Nissen-Meyer, Instaseis: Instant global seismograms based on a broadband waveform database. *Solid Earth* **6**, 701–717 (2015).

169. T. Nissen-Meyer, M. Van Driel, S. C. Stähler, K. Hosseini, S. Hempel, L. Auer, A. Colombi, A. Fournier, AxiSEM: Broadband 3-D seismic wavefields in axisymmetric media. *Solid Earth* **5**, 425–445 (2014).

170. J. Christmann, V. Helm, S. A. Khan, T. Kleiner, R. Müller, M. Morlighem, N. Neckel, M. Rückamp, D. Steinhage, O. Zeising, A. Humbert, Elastic deformation plays a non-negligible role in Greenland's outlet glacier flow. *Commun. Earth Environ.* **2**, 232 (2021).

171. W. Bertiger, Y. Bar-Sever, A. Dorsey, B. Haines, N. Harvey, D. Hemberger, M. Heflin, W. Lu, M. Miller, A. W. Moore, D. Murphy, P. Ries, L. Romans, A. Sibois, A. Sibthorpe, B. Szilagyi, M. Vallisneri, P. Willis, GipsyX/RTGx, a new tool set for space geodetic operations and research. *Adv. Space Res.* **66**, 469–489 (2020).

172. J. Boehm, B. Werl, H. Schuh, Troposphere mapping functions for GPS and very long baseline interferometry from European Centre for Medium-Range Weather Forecasts operational analysis data. *J. Geophys. Res.* **111**, B02406 (2006).

173. Z. Altamimi, P. Rebischung, L. Métivier, X. Collilieux, ITRF2014: A new release of the International Terrestrial Reference Frame modeling nonlinear station motions. *J. Geophys. Res. Solid Earth* **121**, 6109–6131 (2016).

174. O. Hungr, S. Leroueil, L. Picarelli, The Varnes classification of landslide types, an update. *Landslides* **11**, 167–194 (2014).

175. P. S. Mikkelsen, "Field report from the journey to Northeast Greenland 2023" (in Danish) (North-East Greenland Company Nanok, 2023); https://www.xsirius.dk/sites/default/files/2023-10/Feltrapport%202023%20DK_til%20hjemmeside.pdf .

176. J. Obu, S. Westermann, A. Bartsch, N. Berdnikov, H. H. Christiansen, A. Dashtseren, R. Delaloye, B. Elberling, B. Etzelmüller, A. Kholodov, A. Khomutov, A. Kääb, M. O. Leibman, A. G. Lewkowicz, S. K. Panda, V. Romanovsky, R. G. Way, A. Westergaard-Nielsen, T. Wu, J. Yamkhin, D. Zou, Northern Hemisphere permafrost map based on TTOP modelling for 2000–2016 at 1 km2 scale. *Earth Sci. Rev.* **193**, 299–316 (2019).

177. E. W. Willcox, J. Bendtsen, J. Mortensen, C. Mohn, M. Lemes, T. Juul-Pedersen, J. Holding, E. F. Møller, M. K. Sejr, M.-S. Seidenkrantz, S. Rysgaard, An Updated

View of the Water Masses on the Northeast Greenland Shelf and Their Link to the Laptev Sea and Lena River. *J. Geophys. Res. Oceans* **128**, e2022JC019052 (2023).

178. N. Henriksen, A. K. Higgins, F. Kalsbeek, T. C. R. Pulvertaft, Greenland from Archaean to Quaternary. Descriptive text to the Geological map of Greenland, 1: 2 500 000. *Geol. Greenl. Surv. Bull.* **185**, 2–93 (2000).

179. J. C. Escher, M. Smith, *Geological Map of Greenland, 1:500,000, Sheet 11, Kong Oscar Fjord* (Geological Survey of Denmark & Greenland, 2001).

180. P. V. Glob, M. Degerbøl, Eskimo settlements in Kempe fjord and King Oscar fjord. Treaarsexpeditionen til Christian X's Land 1931-34. *Medd. Gronl.* •••, 102 (1935).

181. J. F. Jensen, M. Hardenberg, "Arkæologisk berejsning af området mellem Kong Oscar Fjord og Kejser Franz Joseph Fjord Nordøstgrønland," SILA – Arctic Centre at the Ethnnographic Collections, the National Museum of Denmark (2012).

182. R. V. Sailor, A. M. Dziewonski, Measurements and interpretation of normal mode attenuation. *Geophys. J. Int.* **53**, 559–581 (1978).

183. S. Heimann, M. Isken, D. Kühn, H. Sudhaus, A. Steinberg, S. Daout, S. Cesca, H. Bathke, T. Dahm, Grond : a probabilistic earthquake source inversion framework, Version 1.10, GFZ Data Services (2018); https://doi.org/10.5880/GFZ.2.1.2018.003.

184. P. Poli, Continuation of Events Detection with Global Long-Period Seismic Data: An Analysis from 2010 to 2022. *Seismol. Res. Lett.* **95**, 1486–1494 (2023).